ADVANCED SYSTEM COMPONENTS FOR THE DEVELOPMENT OF A HANDHELD ION TRAP MASS SPECTROMETER

Kevin Philip Schultze

A dissertation submitted to the faculty at the University of North Carolina at Chapel Hill in partial fulfillment of the requirements for the degree of Doctor of Philosophy in the Department of Chemistry.

Chapel Hill
2014

Approved by:

J. Michael Ramsey

R. Mark Wightman

James W. Jorgenson

Michel R. Gagné

Bo Li

© 2014
Kevin Philip Schultze
ALL RIGHTS RESERVED

ABSTRACT

Kevin Philip Schultze: Advanced System Components for the Development of a Handheld Ion Trap Mass Spectrometer
(Under the direction of J. Michael Ramsey)

This work describes the development and implementation of system components utilized in a handheld ion trap mass spectrometer (MS). Current state-of-the-art portable mass spectrometers fall in the 30 to 40 lb. range due to their large and heavy vacuum systems. The strategy used in this work to create lighter, handheld instruments is to eliminate much of the vacuum pumping requirements by operating the entire instrument under 1 Torr of background pressure, i.e. 3 orders of magnitude higher than conventional instruments. Reducing the ion trap size by a factor of 20 and operating these miniature traps at increased RF drive frequencies compensates for the ions' reduced mean free path, making mass analysis possible at these elevated pressures.

The first component developed was a novel ion trap geometry. The design is a modification of the cylindrical ion trap (CIT), using three electrodes to produce an elongated two-dimensional trapping region capped by planar mesh electrode features on each end. The SLIT's increased dimensionality led to a tenfold increase in sensitivity versus a CIT with the same critical dimensions while maintaining identical resolution. This 5 mm long SLIT with critical dimensions x_o = 500 μm and z_o = 650 μm represents the smallest linear type ion trap reported to date and maintains higher resolution than their larger counterparts. SLIT

operation in pressures exceeding 1 Torr of helium, nitrogen, and air buffer gasses also represents the highest pressure operation reported for linear ion traps.

Ion detection at elevated pressures was achieved using a Faraday cup and charge sensitive amplifier. Mass spectra were collected using both a commercial amplifier and two custom made amplifiers. The smaller of the two custom Faraday cup amplifiers was incorporated into a miniature vacuum chamber along with the SLIT mass analyzer and glow discharge ion source. The operation of this MS system is the first reported miniature instrument operated without the use of turbomolecular vacuum pumps, and can in fact be operated with only a simple miniaturized roughing pump. Incorporating the miniature chamber, pump, and a custom miniature RF system, a prototype MS was developed weighing 2 lbs. and drawing 8.2 W.

Finally, gas chromatography - mass spectrometry (GC-MS) experiments were carried out utilizing the newly developed miniature MS instrumentation with a full size GC to demonstrate the feasibility of a future handheld GC-MS device. Detection of a variety of organic analytes during 2.5 minute separations was demonstrated in both helium and nitrogen carrier gasses with limits of detection of 0.056 ng injected on-column.

TABLE OF CONTENTS

LIST OF FIGURES

LIST OF ABBREVIATIONS AND SYMBOLS

”	inch
°C	degrees Celcius
2D	two dimensional
3D	three dimensional
A	Amp
AC	alternating current
AGC	automatic gain control
a.u.	arbitrary units
CIT	cylindrical ion trap
CITSIM	cylindrical ion trap simulator
cm	centimeter
CNC	computer numerical control
CTIA	capacitive transimpedance amplifier
DA-4	detector amplifier 4
DAQ	data acquisition
DC	direct current

DMMP	dimethyl methylphosphanate
EI	electron impact ionization
EM	electron multiplier
FC	Faraday cup
FET	field effect transistor
fF	femptoFarad
FID	flame ionization detector
FT-ICR	Fourier transform ion cyclotron resonance
FWHM	full width at half max
g	gram
GC	gas chromatography/chromatograph
GC-MS	gas chromatography - mass spectrometry
GD	glow discharge
GPU	graphics processing unit
H_2	hydrogen gas
He	helium
HPMS	high pressure mass spectrometry

Hz	Hertz
IC	integrated circuit
I.D.	inner diameter
IMS	ion mobility spectrometry
in.	inch
KE	kinetic energy
kg	kilogram
kHz	kiloHertz
lbs.	pounds
LDR	linear dynamic range
LIT	linear ion trap
LOD	limit of detection
µm	micometer/micron
µs	microsecond
µV	microVolt
m	meter
m/z	mass to charge ratio

MEMS	microelectromechanical system
MES	methyl salicylate
MHz	megaHertz
min	minute
mL	milliliter
mm	millimeter
MOSFET	metal oxide semiconductor field effect transistor
MS	mass spectrometry
ms	millisecond
MS/MS	tandem mass spectrometry
mTorr	milliTorr
mW	milliWatt
N_2	nitrogen gas
nA	nanoAmp
ng	nanogram
ns	nanosecond
NIST	national institute of standards and technology

O.D.	outer diameter
PEEK	polyether ether ketone
pF	picoFarad
ppb	part per billion
ppm	parts per million
QIT	quadrupole ion trap
R_2	coefficient of determination
r_o	inscribed radius of a QIT
RAM	random-access memory
RF	radio frequency (3 kHz – 300 GHz)
RGA	residual gas analyzer
RIT	rectilinear ion trap
RSD	relative standard deviation
s	second
sccm	standard cubic centimeter per minute
SLIT	stretched length ion trap
SMA	subminiature version A

S/N	signal to noise ratio
SWaP	size weight and power consumption
Th	Thompson (a unit equal to 1 Da/elementary charge)
TOF	time-of-flight mass analyzer
Torr	unit of pressure where 760 Torr = 1 atmosphere
UNF	unified screw thread
V	Volt
W	Watt
Xe	xenon
z_o	distance between endcap and center of trap

CHAPTER 1: MINIATURIZING MASS SPECTROMETERS AND THE QUADRUPOLE ION TRAP

Introduction

Mass spectrometry (MS) has long been among the most informative of analytical techniques. Due to its distinctive capability to selectively detect a large variety of analytes with both speed and sensitivity, MS has found wide-ranging applications in areas such as trace elemental analysis, biomolecule characterization in highly complex samples, and isotope ratio determination.[1] However, the large size, weight, and power consumption (SWaP) inherent to nearly all MS systems generally confines their use to laboratory settings rather than in-field analyses. Whether it is the rapid detection necessary for security applications or *in situ* analysis required for environmental studies, there exist many applications in which it is necessary or at least desirable to make these chemical measurements directly in the field. To meet this need, several successful efforts have gone into miniaturizing equipment for field work utilizing other analytical techniques such as ion mobility spectrometry (IMS) and Raman spectroscopy.[2] However, none of the current hand-portable instrumentation can offer the combination of speed, selectivity, and sensitivity that is possible with MS, and the fact that these instruments have found wide use despite their shortfalls is illustrative of the large impact that a hand portable mass spectrometer would have.

Not surprisingly, many efforts over several decades have been targeted at achieving ever smaller mass spectrometers with the eventual goal of hand-portability.

Attempts to miniaturize each of the common types of mass analyzers have been carried out and a historical treatment of these efforts will be the focus of Section 1.1. Of particular interest in the field of miniature mass spectrometry is the quadruple ion trap (QIT) for which a detailed explanation of its operation will be given in Section1.2. And finally, a description of the current state of the art in microscale ion traps and our laboratory's focus on their operation at high pressures will be described in the final section of this chapter.

1.1 Miniaturization of Common Mass Analyzers

All mass spectrometers consist of three core components: an ion source, a mass analyzer, and a detector. In addition, they also include several peripheral systems such as the control electronics, vacuum system, and data collection system. Upon initial examination one might not consider the miniaturization of the mass analyzer to be a vital step in the shrinking of the overall system since in many instances, the mass analyzer represents only a small portion of the instrument's total size and/or weight. However, reducing the mass analyzer dimensions can impact the SWaP of the peripheral systems in a number of ways. First, since all mass analyzers utilize electric fields in some manner to guide and separate ions, lower voltages can be used to create the same field strengths at smaller dimensions, leading to lower power electronics. Additionally, as the mass analyzer shrinks, so does the required mean free path for ion-neutral collisions. This reduced mean free path leads to higher allowable pressures and thus reduced vacuum requirements for all types of mass spectrometers, albeit to varying degrees. Since the vacuum system is almost always the largest contribution to a portable instrument's size and weight, significantly reducing the vacuum requirements is a necessity.

Sector Analyzers

The magnetic sector was one of the first mass analyzers to receive significant miniaturization efforts due to its long history and wide use in the field of mass spectrometry.[3] The sector MS is a 'beam type' instrument in which an ion beam is controlled and separated by means of a magnetic, and often an electric sector. (Figure 1.1a) Acting as a deterrent for miniaturization, sectors are larger than most other mass spectrometers due to the large and heavy magnetic and electric sectors employed. They also require comparatively strict vacuum requirements, typically 10^{-6} Torr or lower . Offsetting some of these challenges to miniaturization is the fact that unlike other mass analyzers, sectors can employ exclusively static fields, as in the Mattauch-Herzog geometry.[4] This property reduces both power draw and complexity, aiding in the miniaturization of the electronics package. In addition, miniaturization facilitates the use of small permanent magnets that draw no power at all.

Taking advantage of the ability of the Mattauch-Herzog geometry's high MS acquisition rate resulting from simultaneous detection of all ions at the array detector, Sinha *et al.* developed an early miniaturized sector MS to interface with a fast gas chromatography (GC) separation.[5] This instrument, based on a permanent magnet greater than 10 kg with a 12.7 cm detection plane was able to successfully detect fast eluting peaks of 200-300 ms from a microbore GC column. Other efforts have gone into packaging a sector of an alternative geometry into a portable, suitcase sized instrument able to detect a wide variety of organic compounds at a resolving power around 150.[6] The weight and power consumption of 20 kg and 30 W respectively, while impressive for the time period, comes at the cost of very low throughput and limited run times. Previously, even miniaturized sectors still had ion flight paths of tens of centimeters, but more recently, microfabrication techniques have

been used to create a 2 cm radius miniature sector with crossed electric and magnetic fields which achieve a resolving power of 106.[7]

Time-of-Flight

Time-of-flight (TOF) instruments are the most conceptually simple mass spectrometers consisting of an acceleration region where all ions are accelerated to the same kinetic energy (KE), a field free drift region where the ions are separated by flight time, and a high bandwidth ion detector. (Figure 1.1b) Compared to the sector MS, the TOF mass analyzer is typically much lighter in weight while the control electronics remain straightforward and draw little power. Challenges to the miniaturization of TOFs include their similar vacuum requirements to sector instruments as well as the fact that their resolving power is directly related to flight tube length. However, the precise control of ion kinetic energies achievable with simple electrode geometries can yield miniaturized TOF analyzers with resolution comparable to many benchtop mass spectrometers.

By far the largest TOF miniaturization effort has been conducted in the lab of Dr. Robert Cotter with their 'Tiny TOF' project yielding several successful instruments over the years.[8-10] This research has progressed in stages, starting with a modest reduction of the flight tube length from the common 1-1.5 m to 20 cm[8] and finishing with their smallest sized TOF with a flight tube of 5 cm.[9] Their instrument has been targeted towards biological samples and has a reported resolving power of 330. Knowledge gained from this work was later used in the development of a suitcase sized TOF MS directed towards first responders.[10] Another interesting application for miniaturized TOFs is in space exploration where the vacuum pumping requirements are far less stringent. To this purpose, a miniature laser

ablation TOF analyzer has been developed by Riedo *et al.* The prototype system conducts elemental analyses of solid samples at a resolving power of up to 600.[11]

Ion Cyclotron Resonance

When assessing mass analyzers for miniaturization, Fourier Transform Ion Cyclotron Resonance (FT-ICR) mass spectrometry is possibly the least suited for such an endeavor. FT-ICR instruments are both the largest of the conventional mass spectrometers due to the size of the superconducting magnets required as well as having pressure requirements of several orders of magnitude lower than sector or TOF analyzers. Large mean free paths are needed to provide adequate time to measure the ions' cyclotron resonant frequencies, and thus their mass to charge ratios, within the magnetic and electric trapping fields. (Figure 1.1c) However, FT-ICR instruments routinely achieve resolving powers well into the millions, making them the highest resolution instruments available. These characteristic advantages and disadvantages remain upon miniaturization of the FT-ICR, with Dietrich *et al.* developing a large suitcase sized instrument with a resolving power of 1000.[12-13] This lone example of FT-ICR miniaturization still represents the highest mass resolution obtained in miniaturized instruments, although significantly reducing its size much further seems unlikely.

Linear Quadrupoles

Operating in the $10^{-4} – 10^{-5}$ Torr pressure range, the linear quadrupole is relatively pressure tolerant when compared to the previously discussed mass analyzers, and again, even higher pressures are achieved as the ion path length is reduced in miniaturized instruments. A linear quadrupole consists of two sets of metal rods with opposing RF and DC voltages on

each pair creating a time varying quadrupolar field between the four rods. (Figure 1.1d) These voltages are set such that only a narrow range of mass to charge values are passed through the rods to the detector at a time, and a linked scan of the RF and DC voltages produces the full mass spectrum. There exist two primary challenges towards the miniaturizing of the linear quadrupole. The first challenge, having to do with the power requirements of the large RF voltages, scales favorably with miniaturization as discussed previously. The second challenge is that machining and alignment tolerances for the rods are tight enough to pose a manufacturing challenge even for full size instruments. However, microfabrication and next generation manufacturing techniques such as 3D printing show promise in overcoming this limitation as well. As such, the miniaturization of the linear quadrupole has been relatively successful, even finding commercial success as residual gas analyzers (RGA).

Full-scale linear quadrupole rods *ca.* 20 cm in length and 10 mm in diameter can be significantly reduced in size using conventional machining or high precision techniques such as electrical discharge machining, without sacrificing much in the way of overall performance. Research along these lines at Inficon, a gas analysis company, has led to a RGA as small as 1.27 cm long with an inscribed radius, r_o, of 0.33 mm.[14] The resolution of this device, ~0.9 Th, was found to be relatively constant even up to pressures of 10 mTorr (~250 times higher pressure than full-scale linear quadrupoles). However, typical of linear quadrupoles, sensitivity was reduced at higher pressures (~50% reduction at 2-3 mTorr) caused by ions being lost before reaching the detector due to scattering collisions with the background gas.

Microfabrication techniques are also being utilized in linear quadrupole construction to maintain dimensional tolerances as analyzer sizes are pushed ever smaller. As an example, Taylor *et al.* fabricated a device using 30 mm long, 0.5 mm diameter metallized glass fibers mounted on a microfabricated silicon support for alignment.[15] While this device resulted in only modest resolution, it likely merits further study due to the precision and scalable manufacturing potential of microfabricated devices. Also of note when moving to such small dimensions, ion throughput and thus sensitivity can be compromised. To ameliorate this trend, arrays of many linear quadrupoles have been operated in parallel, theoretically increasing the device sensitivity linearly with each set added.[16] This is a strategy we will see repeated with miniaturized quadrupole ion traps.

Quadrupole Ion Traps

While the quadrupole ion trap (QIT) has a shorter history, not becoming a viable mass analyzer until the mid-1980s, they represent the bulk of the research into miniaturized MS instruments due to their relatively small size, less stringent dimensional tolerances, and most importantly, pressure tolerance. An in-depth overview of this research on miniature ion traps and their operation at elevated pressures can be found in Section 1.3. However, as the remainder of this dissertation deals exclusively with the quadrupolar ion trap, a detailed description of its invention, development, and theory of operation will first be given in Section 1.2.

1.2 The Quadrupole Ion Trap: Theory and Operation

Qualitative Description of QIT Trapping

Based on initial work by Penning,[17] the first ion trapping devices employed a magnetic field trapping charged species in circular orbits while a cylindrically symmetric quadrupolar electric field formed a potential well in the axial dimension. This configuration has the limitation that it must be operated under high vacuum conditions, and as such, continues to find use only in FT-ICR instruments.

Confinement of ions in the absence of a magnetic field was first reported by Paul and Steinwedel[18] and was achieved simply by oscillating the quadrupolar electric field of the Penning trap. Because the field strength increases with the square of the distance from the center of the trap, where its value is zero, the net impulse over a single oscillation of the field on an ion is non-zero. Put more simply, an ion will be forced a distance towards the center of the trap during the attractive half of the cycle and repelled another distance during the repulsive half. Because the ion is closer to the trap's center during the repulsive half, the average repulsive force will be weaker than the original attractive force resulting in a net movement of the ion towards the trap's center. The fact that the field is axially attractive while being radially repulsive and *vice versa* is of no consequence, as over a period of oscillation a net focusing impulse is achieved in both directions.

To achieve this cylindrically symmetric quadrupolar field, electrodes are constructed along isopotential lines. This configuration yields three electrodes with hyperbolic surfaces consisting of two endcap electrodes with a 'ring' electrode sandwiched between them (Figure 1.2). The electrode size is defined by the shortest distance from the center of the trap to the

ring electrode, r_o, and the shortest distance from the center to the endcaps, z_o. To form an ideal quadrupolar field, a ratio or $r_o^2 = 2z_o^2$ is required.

Mathematical Treatment of QIT Operation

Several detailed descriptions of the theory of ion motion in a QIT have been previously presented,[19-22] and the reader is directed to these for reference beyond the overview provided here. In a purely quadrupolar field, the potential, $\phi_{x,y,z}$, at any point varies quadratically with distance from the origin and can be written in its most simple form as

$$\phi_{x,y,z} = A(\lambda x^2 + \sigma y^2 + \gamma z^2) + C \tag{1.1}$$

where A is a non-zero term including the electric potential applied between the electrodes, C is a fixed potential applied to the whole system, and λ, σ, and γ are weighting constants applied to the x, y, and z coordinates, respectively. It can be seen that there are no cross terms (e.g. xy terms) which has the important implication that the force and thus ion motion in each coordinate direction can be treated independently. As with all electric fields with zero volume charge density, it is necessary for the Laplace condition to be met where the second partial differential of the potential at any point must be equal to zero.

$$\nabla^2\phi = \frac{\partial^2\phi}{\partial x^2} + \frac{\partial^2\phi}{\partial y^2} + \frac{\partial^2\phi}{\partial z^2} = 0 \tag{1.2}$$

From which Eq. (1.2) becomes

$$\nabla^2\phi = A(2\lambda + 2\sigma + 2\gamma) = 0 \tag{1.3}$$

And because A is non-zero

$$\lambda + \sigma + \gamma = 0 \tag{1.4}$$

Because the QIT is cylindrically symmetric about the z-axis, λ and σ must be equal leading to the simplest values for all three coefficients as

$$\lambda = \sigma = 1; \quad \gamma = -2 \tag{1.5}$$

Substituting these values into Eq. (1.1) and converting to cylindrical coordinates yields

$$\phi_{r,z} = A(r^2 - 2z^2) + C \tag{1.6}$$

We now evaluate the general coefficients A and C in terms of the potential within the actual ion trapping electrodes. First we define ϕ_o as the potential applied between the ring electrode and endcaps. Combination of the cases $\phi_{r_o,0}$ and ϕ_{0,z_o} leads to the expression

$$\phi_o = A(r_o^2 + 2z_o^2) \tag{1.7}$$

Thus solving for A and substituting into Eq. (1.6) yields

$$\phi_{r,z} = \frac{\phi_o(r^2 - 2z^2)}{(r_o^2 + 2z_o^2)} + C \tag{1.8}$$

The easiest and most common way to operate a QIT is to apply the desired potential to the ring electrode and ground the endcaps. Thus we can use the fact that ϕ_{0,z_o} is equal to zero to solve for the final coefficient C and substitute back into Eq. (1.8) yielding

$$\phi_{r,z} = \frac{\phi_o(r^2 - 2z^2)}{(r_o^2 + 2z_o^2)} + \frac{2\phi_o z_o^2}{(r_o^2 + 2z_o^2)} \tag{1.9}$$

As noted in the qualitative QIT description, the applied potential, ϕ_o, is oscillating. In addition, there can also be a DC component applied in series to the ring electrode resulting in the expression for ϕ_o of

$$\phi_o = (U + V\cos\Omega t) \tag{1.10}$$

where V is the maximum AC voltage amplitude, U is the DC voltage amplitude, t is time, and Ω is the angular frequency of the AC voltage. Upon substitution into Eq. (1.9) we arrive at the full equation for the potential inside a QIT as conventionally operated

$$\phi_{r,z} = \frac{(U + V\cos\Omega t)(r^2 - 2z^2)}{(r_o^2 + 2z_o^2)} + \frac{2(U + V\cos\Omega t)z_o^2}{(r_o^2 + 2z_o^2)} \tag{1.11}$$

Recalling that forces in each coordinate direction can be treated independently, we will start with the z dimension. Combining the Lorentz force law for charged particles and Newton's second law we can write the expression for the force on an ion, F_z, of mass m and charge *e* as

$$F_z = -e\left(\frac{d\phi}{dz}\right) = e\frac{4(U + V\cos\Omega t)z}{(r_o^2 + 2z_o^2)} = m\left(\frac{d^2z}{dt^2}\right) \tag{1.12}$$

The expression for F_r is identical with the exception of the -2:1 relationship given by the Laplace condition earlier, representative of the fact that the force on an ion is attractive towards the origin in the z direction while being repulsive in the r dimension and *vice versa*. The final equality above represents the differential equation of ion motion in a QIT. Fortunately, a solution to this form of differential equation was determined by Mathieu in 1868 from his study of vibrating stretched skins.[23] When Eq. (1.12) is rewritten and expanded as shown below,

$$\left(\frac{d^2z}{dt^2}\right) + \left[-\frac{4eU}{m(r_o^2 + 2z_o^2)} - \frac{4eV\cos\Omega t}{m(r_o^2 + 2z_o^2)}\right]z = 0 \tag{1.13}$$

it becomes evident that this is a special form of the Mathieu equation as shown below in its common form.

$$\frac{d^2u}{d\xi^2} + (a_u - 2q_u \cos 2\xi)u = 0 \tag{1.14}$$

Where u is a displacement; ξ is a parameter equal to $\Omega t/2$ in this case; and *a* and *q* are dimensionless parameters which in the special case of the QIT are known as "trapping parameters." A detailed walkthrough of the transformations made to yield the expressions for the trapping parameters can be found here,[19] but for the purposes of this description they will simply be given as

$$a_z = -\frac{16eU}{m(r_o^2 + 2z_o^2)\Omega^2} \tag{1.15}$$

and

$$q_z = \frac{8eV}{m(r_o^2 + 2z_o^2)\Omega^2} \tag{1.16}$$

Again, the expressions for a_r and q_r are identical after accounting for the -2:1 ratio. The parameters a_u and q_u are seen to be of particular interest as they are functions not only of an ion's mass to charge ratio, but of all the relevant instrumental parameters. Thorough examination of the solutions to the Mathieu equations as they relate to the QIT, again shown in detail elsewhere,[19] reveal several regions in the a-q space where ion motion is stable and periodic. Figure 1.3 shows both the r-stable regions (upward pointing) and the z-stable regions (downward pointing). An ion which resides in one of the several overlapping regions will undergo stable motion in both dimensions and will thus remain trapped. The practically useful region of ion stability near the *a*-*q* origin is shown in Figure 1.4. The regions of stability are bound by lines corresponding to the β parameter equal to 0 and 1 for the r and z dimensions. This new parameter will now be described below.

Motion of Trapped Ions in the QIT

There remain a few aspects of ion motion in the QIT left to consider. Recall from the qualitative description that for each RF cycle, a net force acts upon the ion toward the trap's center. The aggregate of these forces can be accurately modeled as the ion residing in a parabolic pseudopotential well in which the ion undergoes stable simple harmonic motion. The frequency of this motion can be expressed by a new trapping parameter, β_u, which is a complex function of a and q given by the continued fraction

$$\beta_u^2 = a_u + \cfrac{q_u^2}{(\beta_u+2)^2 - a_u - \cfrac{q_u^2}{(\beta_u+4)^2 - a_u - \cfrac{q_u^2}{(\beta_u+6)^2 - a_u - \cdots}}} + \cfrac{q_u^2}{(\beta_u-2)^2 - a_u - \cfrac{q_u^2}{(\beta_u-4)^2 - a_u - \cfrac{q_u^2}{(\beta_u-6)^2 - a_u - \cdots}}} \tag{1.17}$$

While this is straightforward to solve computationally, Hans Dehmelt, who shared the 1989 Nobel Prize in Physics with Paul for the development of the QIT, developed an approximation valid for $q_z << 1$ shown below.[21]

$$\beta_z^2 \cong a_z + \frac{q_z^2}{2} \tag{1.18}$$

This equation was verified experimentally to be valid within 1% for $q_z < 0.4$ by Wuerker *et al.*[22] Owing to β being a dimensionless frequency, it can be converted to an ion's real fundamental frequency of motion within a QIT which we will refer to as the ion's secular frequency, ω, by the following relationship

$$\omega_z = \frac{\beta_z \Omega}{2} \tag{1.19}$$

Because β varies between 0 and 1 for a trapped ion, we can see that an ion's secular frequency of motion can vary between zero and half the RF drive frequency depending on the trapping parameters. Again turning to the theory of the simple harmonic oscillator, the depth of the pseudopotential well, D_z, can be derived[24] to be

$$D_z = \frac{eV^2}{4mz_o^2\Omega^2} = \frac{q_z V}{8} \tag{1.20}$$

for the ideal case of $r_o^2 = 2z_o^2$.

Higher Order Fields

To this point, the discussion of the QIT has assumed a perfect cylindrically symmetric quadrupolar field. In practice however, truncated hyperbolic electrodes, holes for ion injection/ejection, and machining tolerances produce deviations from the ideal. A more general approach to solving Laplace's equation for a system with axial symmetry is given here,[25] the result of which yields an expanded equation for the potential in the ion trap.

$$\phi_{r,z} = \phi_o \left(A_0 + A_1 \frac{z}{r_o} + A_2 \frac{r^2 - 2z^2}{2r_o^2} + A_3 \frac{3r^2 z - 2z^3}{2r_o^3} + A_4 \frac{3r^4 - 24r^2 z^2 + 8z^4}{8r_o^4} + A_5 \frac{15r^4 z - 40r^2 z^3 + 8z^5}{8r_o^5} \ldots \right) \tag{1.21}$$

where the coefficients A_0, A_1, A_2, A_3, A_4, etc. are the weighting factors given to the monopole, dipole, quadrupole, hexapole, octopole, etc. components respectively. For an ideal quadrupolar field, all coefficients other than A_2 become zero, resulting in an equivalent form

of Eq. 1.8 derived earlier. In a real trap, the coefficients change based on the geometrical imperfections introduced.

Inspection of Eq. 1.21 reveals several 'cross terms' in the higher order field components. This has the important consequence that we can no longer consider the motions in the r and z dimensions as strictly uncoupled in a real world device. However, due to the higher order nature of these fields, the quadrupolar field remains dominant near the center of the trap. This becomes an important point when performing mass spectrometry with a QIT.

The QIT as a Mass Spectrometer

Considering the substantial academic and commercial success of the QIT, it is somewhat surprising that it took 30 years after the initial invention of the QIT for it to find wide use as a mass spectrometer. Following the initial report[18] and patent[26] by Paul, the QIT was used primarily by physicists to study fundamental ion properties and ion-neutral interactions. During this period there were some initial attempts to use the new device as a MS starting with the realization by Dawson and Whetten that ions could be ejected through holes drilled in the endcaps and detected with an electron multiplier.[27-28] This same work pioneered the use of mass selective storage to generate mass spectra. This method sets the RF and DC values so that a single mass to charge ratio (m/z) is trapped at the apex of the a-q stability diagram before being ejected by a DC pulse on an endcap. This process is repeated for each m/z generating the full mass spectrum. While this was an important step in QIT development, this method offered little advantage over the already prevalent linear quadrupole mass filter.

The QIT remained relatively obscure as a mass analyzer until the early 1980s when George Stafford conceived of a novel method of mass analysis, leading to the successful commercialization of the QIT by the Finnigan Corporation.[29] This method of mass analysis, known as the mass selective instability scan, traps ions using only an RF voltage so that all the ions exist on the $a_z = 0$ axis in descending order of m/z. The RF amplitude is then ramped linearly causing each ion's q_z to increase as per Eq. 1.16 until it reaches the stability boundary at $q_z = 0.908$, upon which it will be ejected from the trap in the z direction. In this manner, ions are ejected in order of m/z from low to high values. While this method of generating mass spectra worked comparatively well, two more important contributions came out of Finnigan's research before a successful commercial instrument was realized.

Even the most pressure tolerant instruments at that time saw deterioration in performance when background pressures increased much above 10^{-5} Torr, and the same was also expected of the QIT. However, because the goal of Finnigan's QIT project was to produce an inexpensive GC-MS detector, the QIT's performance was evaluated at increasing helium pressures. Unexpectedly, upon introduction of *ca.* 1 mTorr of He background gas, both the resolution and sensitivity were drastically improved. It was eventually realized that the many ion collisions with the He buffer gas reduced the kinetic energy of the ions, 'cooling' them into a very small area in the center of the trap. From here, the ions could be ejected far more efficiently out of the endcap to the detector. Additionally, with the ions cooled very near the center of the trap where the quadrupolar term dominates, any effects of higher order fields from non-ideal electrodes are largely mitigated. This leads to alignment and machining tolerances being much less stringent than in the closely related linear quadrupole.

Even with buffer gas cooling effects, the Finnigan researchers found that large field deviations from the endcap holes and truncated electrodes caused unpredictable mass shifts for certain ions. An evaluation of the possible effects of higher order fields on mass analysis led them to try increasing the ring-endcap distances symmetrically, introducing even term (octopolar, dodecapolar, etc) higher order fields. They found that a 10.4% stretch in the z dimension adequately compensated for the inherent electrode non-idealities and solved the mass shift problem. Most of the QITs today still feature this type of modification.

This final breakthrough allowed for the successful commercialization of the QIT as both a GC-MS instrument (1984) and a standalone research instrument (1985) with both using the now standard trap size of r_o = 1 cm. No longer being limited to a few instrumentation labs, research into applications and development of the QIT exploded. Its ruggedness, low cost, ability to interface with multiple ion sources, and ability to perform multiple stages of mass spectrometry (MS/MS) efficiently has secured its place as a workhorse MS even today.

1.3 Miniature Ion Traps and High Pressure Operation

As stated in Section 1.1, ion trapping instruments have received the most attention in terms of miniaturized MS. This section covers the benefits and challenges of using ion traps as miniature mass analyzers as well as some of the strategies to overcome some of these challenges.

The Cylindrical Ion Trap

A major challenge when miniaturizing the QIT is maintaining adequate tolerances for the hyperbolic electrodes at ever smaller scales. Both conventional machining[30-31] and more

recently developed additive manufacturing techniques[32] have been utilized to recreate hyperbolic trap surfaces at r_o around 2 mm, representing a 5x decrease in size from the conventional QIT. This however appears to be near the current limit in the ability to create these precisely shaped electrodes. In response, much work has gone into the development of a simplified geometry in which flat surfaces are used for the endcap electrodes and a straight cylindrical surface is used as the ring electrode as shown in Figure 1.5b. This cylindrical ion trap (CIT) is far easier to manufacture by both conventional and microfabrication techniques down to scales that are several orders of magnitude smaller than the conventional QIT.

The CIT was patented by Langmuir *et al.* as a simple ion storage device in 1962,[33] which of course predated the mass selective instability mode of operation. It took until 1998 for the use of a CIT as a mass analyzer to be explored.[34] In this work, a 'full size' CIT of r_o = 1 cm was used to generate mass spectra with better than unit mass resolution and an upper mass limit of 600 Th, which is comparable in performance to a QIT with hyperbolic electrodes. As shown in Figure 1.5, the quadrupolar field of the QIT is well approximated by the CIT in the center of the trap where the ions reside. This allows the CIT to be operated in exactly the same manner as the QIT without much loss in performance. Building on information learned from the initial CIT work, the Cooks group from Purdue University soon after developed an entire miniaturized MS system based on a 1/4 scale CIT (r_o = 2.5 mm).[35-36] Performance was adequate with resolving power of ~100 and a 250 Th mass limit, even employing a membrane inlet system for atmospheric sampling. This initial system was relatively large at 55 kg including a 20 kg battery but represented an important first step toward designing a battery-powered miniature MS around an ion trapping instrument.

These initial results spawned several subsequent generations of miniature trapping instruments, culminating in the 'Mini 10' instrument weighing in at 10 kg and drawing 70 W of power.[37] The group was able to maintain performance in terms of mass resolution and range while iteratively reducing the size of the various instrumental components with each generation. This approach to miniaturization, consisting of starting with a laboratory scale instrument and systematically reducing component size while retaining performance, has been termed the "top-down approach."[38]

Microscale Cylindrical Ion Traps

The top-down approach to miniaturizing instruments has the major benefit of retaining much of the performance of their benchtop counterparts, but this high performance typically accompanies higher costs and lower durability. For these reasons, high performing portable instruments such as these have yet to find their way into general use. The alternative, deemed the "bottom-up approach" to miniaturization, starts with a microscale mass analyzer and designs the system around this element. This method seeks to produce smaller instruments of modest performance while taking advantage of the inherent low cost of microfabricated devices. The end goal is a low cost, durable, hand-portable device that can bring mass spectrometry into a variety of new fields.

The research into microscale CITs has varied in scale considerably from r_o values in the 500 μm range[39-43] that can be made with conventional machining or microfabrication, down to the tens of microns and below[44-46] which can require advanced microfabrication techniques. The first attempt at operating a CIT with critical dimensions below 1 mm was by Ramsey and coworkers utilizing a 'sandwich' technique where thin sheets of metal with the

requisite endcap and ring electrode holes were separated by insulating sheets to maintain electrical isolation and achieve proper electrode spacing.[39] Using this same trap, they also described a method of double resonance ejection which improved signal intensity and resolution in microscale traps.[40] It had long been useful to interact with and even eject trapped ions by employing an AC signal on the endcaps at the ion's secular frequency,[47] but Ramsey *et al.* demonstrated improved performance by setting this frequency to a non-linear resonance of the trap, taking advantage of the increased presence of higher order fields.

An obvious consequence of smaller CITs is that they hold fewer ions, leading to poor sensitivity. In fact, simulations predict that once r_o values reach *ca.* 1 μm, this capacity falls to a single ion.[45] However, utilizing arrays of many CITs operated in parallel, one can gain back this sensitivity and even hold more ions than a single trap occupying the same footprint. Geometrically, when r_o is reduced by a factor of n, it is possible to fit 2^n traps in the same footprint. Additionally, it has been simulated that the number of ions a trap can hold scales with r_o^x with x = 1.55 (and even lower as the drive frequency is increased).[48] This results in a net increase in ions stored in a given footprint as the trap size is reduced but comes with the caveat that to maintain resolution all traps must be made identical to tight tolerances. This concept has been utilized in microfabricated trap arrays of 256 and 2304 elements, each of which is a CIT with r_o = 20 μm.[44] The mass spectrum of xenon shown, while modest in resolution, represents the operation of the smallest mass analyzer to date. Blain *et al.* utilized state of the art microfabrication techniques to construct CIT arrays with r_o = 1, 2, 5, and 10 μm but several issues including high device capacitance and exposed dielectric material near the traps prevented their use as mass analyzers.[46] However, traps of this size range meet

the theoretical requirements for operation at atmospheric pressure, and therefore successful operation at this scale is a future goal of the field.

High Pressure Operation of CITs

As mentioned earlier, operation at higher vacuum pressures, allowing the elimination of heavy and power hungry vacuum pumps, is vital for the development of a hand-held mass spectrometer. Because ion traps already operate at background pressures several orders of magnitude higher than other mass analyzers, they have the greatest potential for achieving small handheld size. Several theoretical papers have explored CIT operation at elevated pressures.[49-50] Out of this work, a simple relationship between pressure, P; drive frequency, Ω; and resolution, $\Delta m/m$ of

$$\frac{\Delta m}{m} \propto \frac{P}{\Omega} \tag{1.22}$$

The equation above shows peak widths in the mass spectrum increase linearly with pressure while raising the drive frequency has the opposite effect. This relationship is qualitatively reasonable; the increased number of ion-neutral collisions when the pressure is raised starts to compete with the electric field for control of ion motion leading to wider MS peaks. On the other hand, increasing the frequency along with the pressure so that the number of collisions per RF cycle stays relatively constant keeps the ion motion RF-dominated, leaving the resolution unchanged.

To date, there has been little reported in the way of experimental verification of the above relationship, save for one study that evaluated performance of an ion trap up to 50 mTorr in air buffer gas.[51-52] The results gained from these experiments were concerning for those attempting to develop the field of high pressure mass spectrometry. The peak

widths of about 2 Th at 50 mTorr were used to model the predicted peak widths at 250 mTorr as *ca.* 10 Th. Mass spectrometry at 1 Torr background pressures represents a reasonable benchmark for developing a device with small, lightweight pumps, but it is clear that a mass analyzer with this pressure dependence would be quite useless with peak widths near 40 Th at this pressure.

However, there are several reasons to have optimism in the face of this study. First, it is unclear how the authors determined the pressure inside the MS as there was only indirect measurement and back-calculations of pressures are very dependent on the assumptions made. More importantly, the trap used was relatively large (critical dimensions near 4 mm) and was operated using a low RF frequency of 1.08 MHz. From Eq. 1.22, we know that increasing the RF frequency will reduce peak widths. However, the RF voltage requirements scale with Ω^2 as seen in Eq. 1.16, necessitating a corresponding decrease in trap dimensions to keep the voltages in an attainable range. This relationship between RF drive frequency, pressure, and trap size outlines a clear path towards MS instrumentation capable of operation under ever lower vacuum conditions. The goal of our laboratory is to utilize small, high frequency ion traps to facilitate their operation at pressures at or exceeding 1 Torr.

1.4 Figures

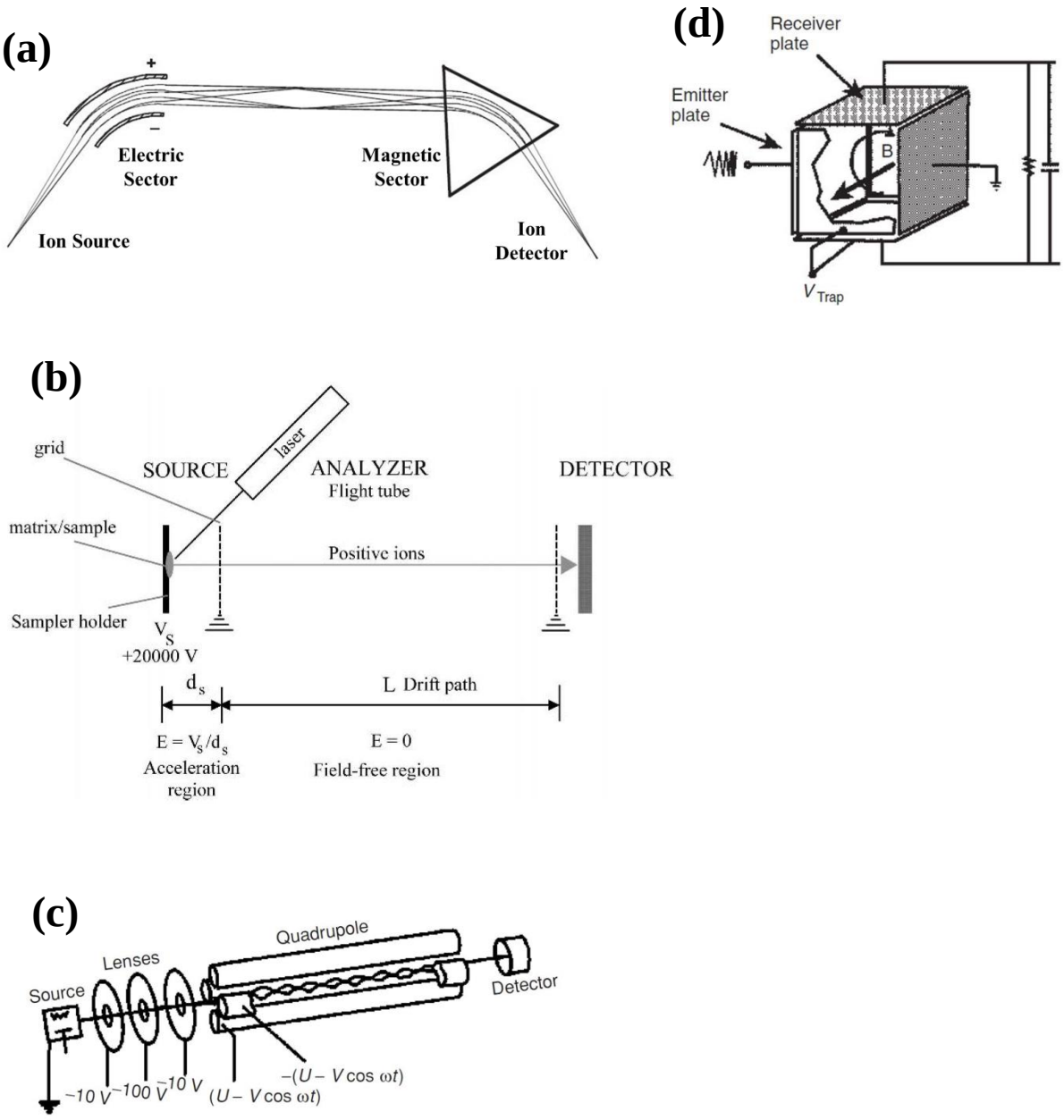

Figure 1.1: Diagrams of several different mass analyzers that have been subject to miniaturization efforts including (a) sector, (b) time-of-flight, (c) linear quadrupole, and (d) ion cyclotron resonance mass analyzers. Reproduced with permission from Mass Spetrometry Principles and Applications by de Hoffmann and Stroobant, Wiley and Sons, 2007.[1]

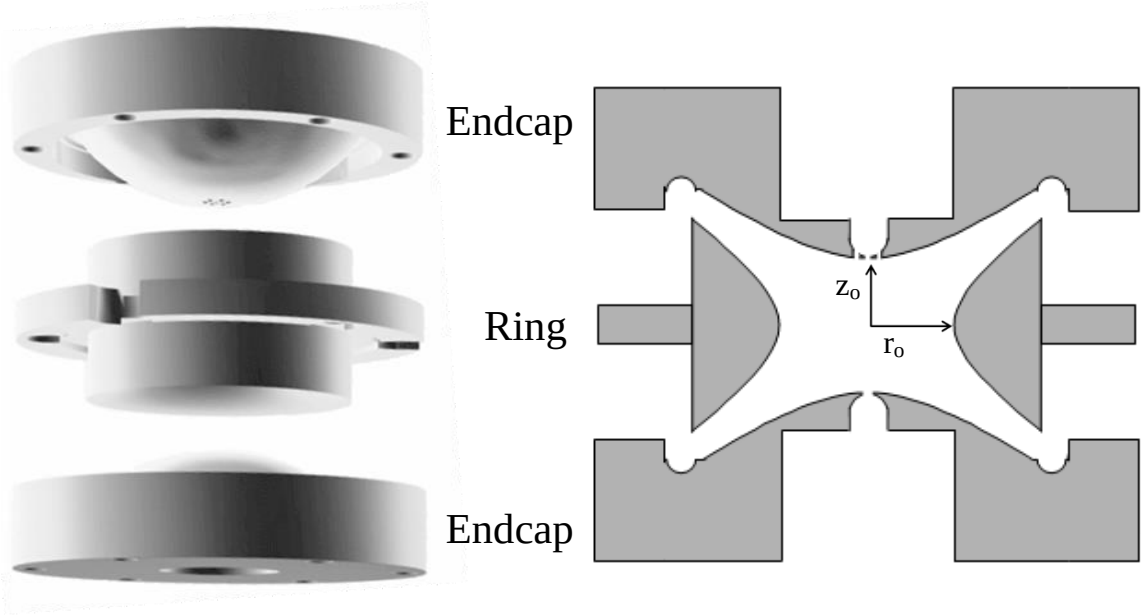

Figure 1.2: A 3D exploded view (left) and 2D cross section (right) of a quadrupole ion trap showing the hyperbolic ring and endcap electrodes. Spacing and alignment is typically achieved via precision ceramic spacers (not shown).

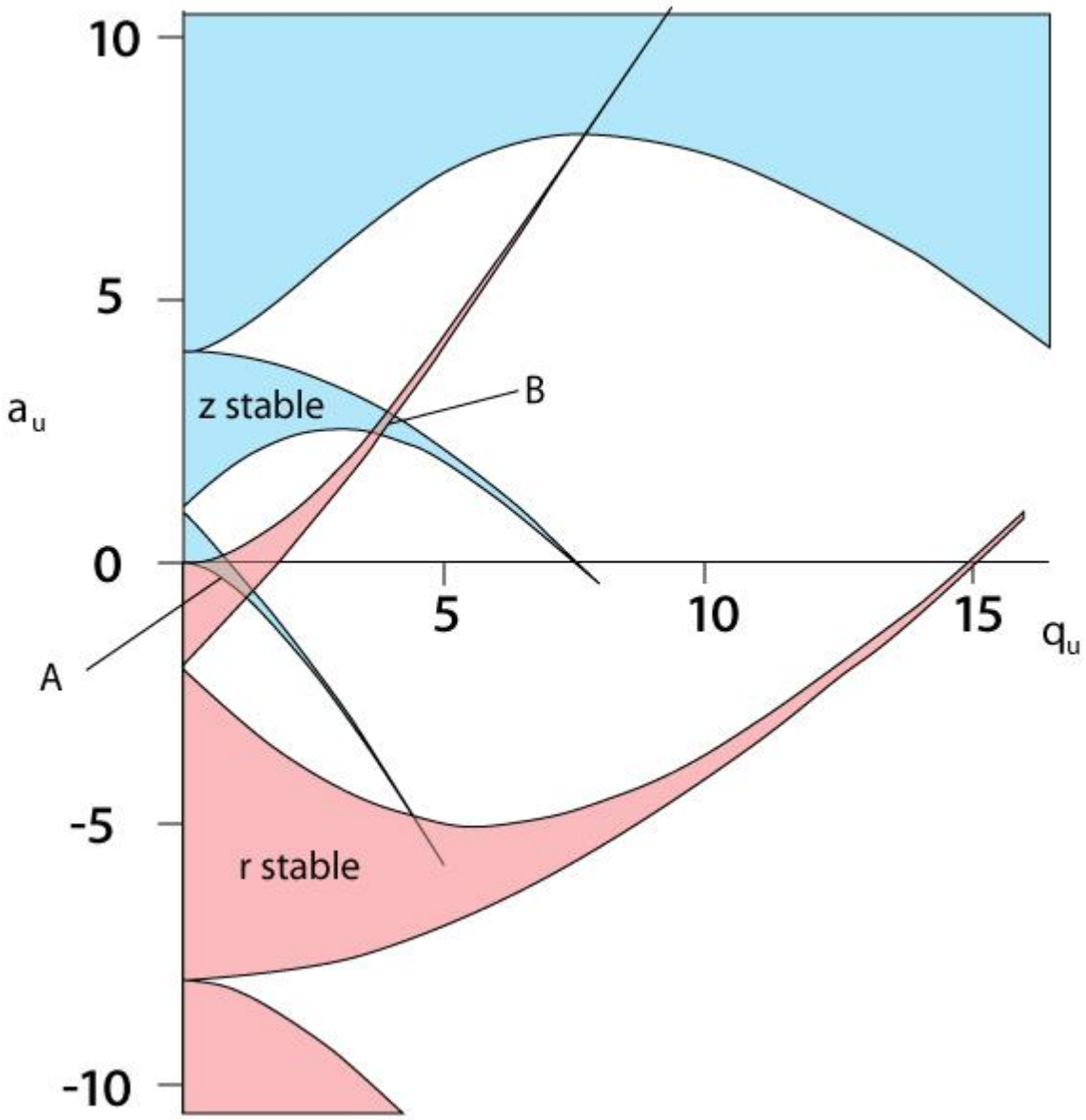

Figure 1.3: Mathieu regions of stability for an ideal 3D quadrupolar field. The regions of stability in the r and z dimensions are seen as identical save the -2:1 relationship stemming from equation 1.5. Stable ion trapping in both dimensions occurs in regions of overlap, of which the two principal areas are indicated as A and B.

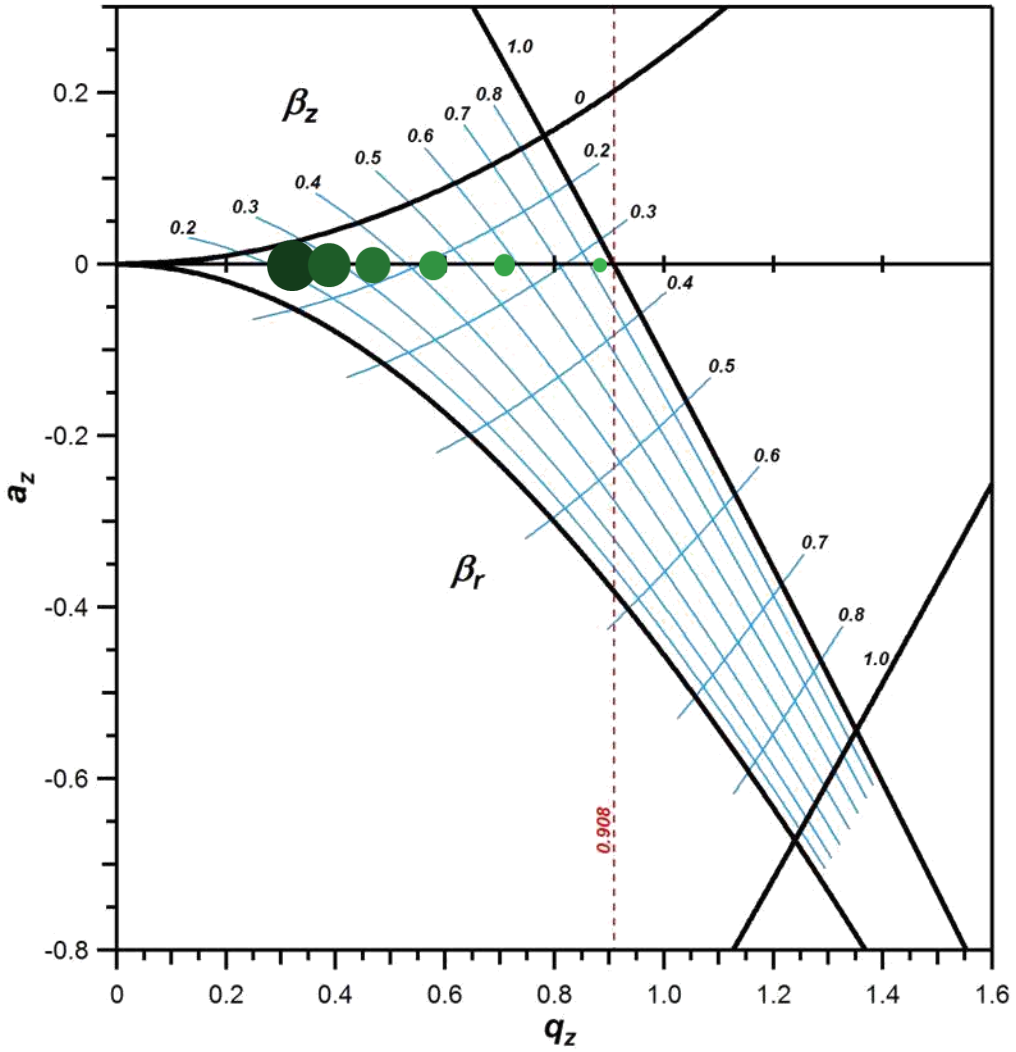

Figure 1.4: A zoomed in view of the principal region of stability near the origin in which all ion traps operate with iso-beta lines shown in light blue. Green circles represent ions of different masses lying along the $a_z = 0$ line corresponding to the normal RF only mode of operation. Ions are scanned to higher q_z values until they reach 0.908 at which point they become unstable in the z dimension and are ejected from the trap.

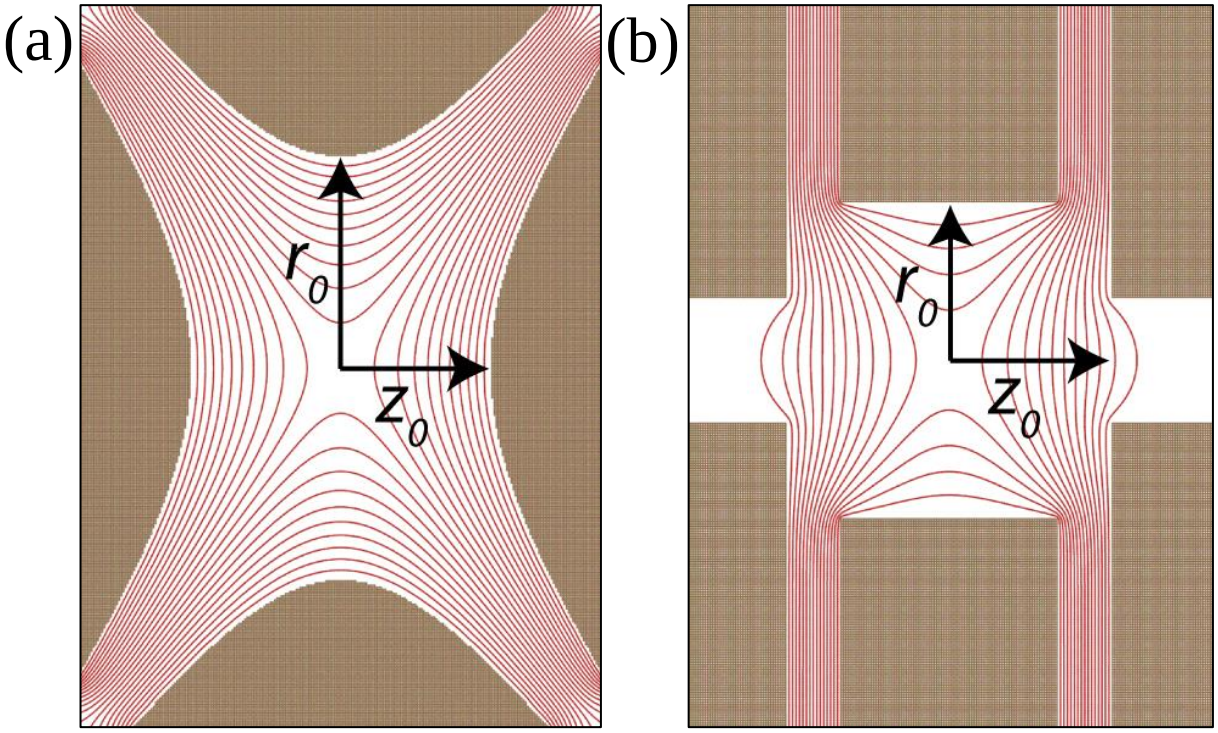

Figure 1.5: Field lines from an ideal quadrupolar field formed by (a) hyperbolic electrodes shown in comparison to (b) those resulting from the cylindrical ion trap geometry. This comparison illustrates that the CIT closely approximates a quadrupolar field near the center of the trap where the ions are held.

1.5 References

1. de Hoffmann, E.; Stroobant, V., *Mass Spectrometry Principles and Applications*. 3rd ed.; John Wiley & Sons: West Sussex, England, 2009; p 489.

2. Janasek, D.; Franzke, J.; Manz, A., Scaling and the design of miniaturized chemical-analysis systems. *Nature* **2006,** *442* (7101), 374-380.

3. Badman, E. R.; Graham Cooks, R., Miniature mass analyzers. *Journal of Mass Spectrometry* **2000,** *35* (6), 659-671.

4. Mattauch, J.; Herzog, R., Über einen neuen Massenspektrographen. *Z. Physik A* **1934,** *89*, 786-795.

5. Sinha, M. P.; Gutnikov, G., Development of a miniaturized gas chromatograph-mass spectrometer with a microbore capillary column and an array detector. *Analytical Chemistry* **1991,** *63* (18), 2012-2016.

6. Kogan, V. T.; Pavlov, A. K.; Chichagov, Y. V.; Tubol'tsev, Y. V.; Gladkov, G. Y.; Kazanskii, A. D.; Nikolaev, V. A.; Pavlichkova, R., Design and testing of a portable magnetic mass spectrometer. *Field Analytical Chemistry & Technology* **1997,** *1* (6), 331-342.

7. Diaz, J. A.; Giese, C. F.; Gentry, W. R., Sub-miniature ExB sector-field mass spectrometer. *Journal of the American Society for Mass Spectrometry* **2001,** *12* (6), 619-632.

8. Bryden, W. A.; Benson, R. C.; Ecelberger, S. A.; Phillips, T. E.; Cotter, R. J.; Fenselau, C., The Tiny-TOF Mass-Spectrometer for Chemical and Biological Sensiing. *Johns Hopkins APL Tech. Dig.* **1995,** *16* (3), 296-310.

9. Cotter, R. J.; Fancher, C.; Cornish, T. J., Miniaturized time-of-flight mass spectrometer for peptide and oligonucleotide analysis. *Journal of Mass Spectrometry* **1999,** *34* (12), 1368-1372.

10. Ecelberger, S. A.; Cornish, T. J.; Collins, B. F.; Lewis, D. L.; Bryden, W. A., Suitcase TOF: A Man-Portable Time-of-Flight Mass Spectrometer. *Johns Hopkins APL Tech. Dig.* **2004,** *25*, 14-19.

11. Riedo, A.; Bieler, A.; Neuland, M.; Tulej, M.; Wurz, P., Performance evaluation of a miniature laser ablation time-of-flight mass spectrometer designed for in situ investigations in planetary space research. *Journal of Mass Spectrometry* **2013,** *48* (1), 1-15.

12. Dietrich, D. D.; Keville, R. F. Portable ion trap mass spectrometer for pollutant detection - has electron source, mass analyser and ion detector assembly combined into single device and mounted in hollow permanent magnet. U.S. 5,451,781 A, US5451781-A 19 Sep 1995 H01J-049/38 199543 Pages: 13, 1994.

13. Henry, C. M., Focus: The incredible shrinking mass spectrometers. *Analytical Chemistry* **1999,** *71* (7), 264A-268A.

14. Holkeboer, D. H.; Karandy, T. L.; Currier, F. C.; Frees, L. C.; Ellefson, R. E., Miniature quadrupole residual gas analyzer for process monitoring at milliTorr pressures. *Journal of Vacuum Science & Technology A* **1998,** *16* (3), 1157-1162.

15. Taylor, S.; Tunstall, J. J.; Leck, J. H.; Tindall, R. F.; Jullien, J. P.; Batey, J.; Syms, R. R. A.; Tate, T.; Ahmad, M. M., Performance improvements for a miniature quadrupole with a micromachined mass filter. *Vacuum* **1999,** *53* (1–2), 203-206.

16. Orient, O. J.; Chutjian, A.; Garkanian, V., Miniature, high-resolution, quadrupole mass-spectrometer array. *Review of Scientific Instruments* **1997,** *68* (3), 1393-1397.

17. Penning, F. M., Glow discharge at low pressure between coaxial cylinders in an axial magnetic field. *Physica* **1936,** *3* (9), 873-894.

18. Paul, W.; Steinwedel, H., A new mass spectrometer without a magnetic field. *Z Naturforsch* **1953,** *8a*, 448-450.

19. March, R. E., Quadrupole ion traps. *Mass Spectrometry Reviews* **2009,** *28* (6), 961-989.

20. March, R. E., An Introduction to Quadrupole Ion Trap Mass Spectrometry. *Journal of Mass Spectrometry* **1997,** *32* (4), 351-369.

21. Major, F. G.; Dehmelt, H. G., Exchange-Collision Technique for the rf Spectroscopy of Stored Ions. *Physical Review* **1968,** *170* (1), 91-107.

22. Wuerker, R. F.; Shelton, H.; Langmuir, R. V., Electrodynamic Containment of Charged Particles. *Journal of Applied Physics* **1959,** *30* (3), 342-349.

23. Mathieu, E., Mémoire sur le mouvement vibratoire d'une membrane de forme elliptique. *J. Math. Pure Appl.* **1868,** *13*, 137.

24. Todd, J. F. J.; Lawson, G.; Bonner, R. F., *Quadrupole Mass Spectrometry and its Applications*. Elsevier: 1976; p 181-224.

25. March, R. E.; Londry, F. A., Chapter 2 - Theory of Quadrupole Mass Spectrometry. In *Practical Aspects of Ion Trap Mass Spectrometry*, March, R. E.; Todd, J. F. J., Eds. CRC Press: 1995; Vol. 1, pp 25-48.

26. Paul, W.; Helmut, S. Apparatus for separating charged particles of different specific charges. U.S. Patent 2,939,952 A, 1960.

27. Dawson, P. H.; Whetten, N. R., Ion Storage in Three-Dimensional, Rotationally Symmetric, Quadrupole Fields. I. Theoretical Treatment. *Journal of Vacuum Science & Technology* **1968,** *5* (1), 1-10.

28. Dawson, P. H.; Whetten, N. R., Ion Storage in Three-Dimensional, Rotationally Symmetric, Quadrupole Fields. II. A Sensitive Mass Spectrometer. *Journal of Vacuum Science & Technology* **1968,** *5* (1), 11-18.

29. Syka, J. E. P., Chapter 4 - Commercialization of the Quadrupole Ion Trap. In *Practical Aspects of Ion Trap Mass Spectrometry*, March, R. E.; Todd, J. F. J., Eds. CRC Press: 1995; Vol. 1, pp 169-205.

30. Kaiser Jr, R. E.; Graham Cooks, R.; Stafford Jr, G. C.; Syka, J. E. P.; Hemberger, P. H., Operation of a quadrupole ion trap mass spectrometer to achieve high mass/charge ratios. *International Journal of Mass Spectrometry and Ion Processes* **1991,** *106* (0), 79-115.

31. Lammert, S. A.; Rockwood, A. A.; Wang, M.; Lee, M. L.; Lee, E. D.; Tolley, S. E.; Oliphant, J. R.; Jones, J. L.; Waite, R. W., Miniature Toroidal Radio Frequency Ion Trap Mass Analyzer. *Journal of the American Society for Mass Spectrometry* **2006,** *17* (7), 916-922.

32. Clare, A. T.; Gao, L.; Brkić, B.; Chalker, P. R.; Taylor, S., Linear Ion Trap Fabricated Using Rapid Manufacturing Technology. *Journal of the American Society for Mass Spectrometry* **2010,** *21* (2), 317-322.

33. Haywood, S.; Langmuir, D. B.; Langmuir, R. V.; Wuerker, R. F. Containment device. U.S. Patent 3,065,640, 1962.

34. Wells, J. M.; Badman, E. R.; Cooks, R. G., A Quadrupole Ion Trap with Cylindrical Geometry Operated in the Mass-Selective Instability Mode. *Analytical Chemistry* **1998,** *70* (3), 438-444.

35. Patterson, G. E.; Guymon, A. J.; Riter, L. S.; Everly, M.; Griep-Raming, J.; Laughlin, B. C.; Zheng, O.; Cooks, R. G., Miniature Cylindrical Ion Trap Mass Spectrometer. *Anal. Chem.* **2002,** *74* (24), 6145-6153.

36. Riter, L. S.; Peng, Y.; Noll, R. J.; Patterson, G. E.; Aggerholm, T.; Cooks, R. G., Analytical Performance of a Miniature Cylindrical Ion Trap Mass Spectrometer. *Analytical Chemistry* **2002,** *74* (24), 6154-6162.

37. Gao, L.; Song, Q.; Patterson, G. E.; Cooks, R. G.; Ouyang, Z., Handheld Rectilinear Ion Trap Mass Spectrometer. *Anal. Chem.* **2006,** *78* (17), 5994-6002.

38. Ouyang, Z.; Gao, L.; Fico, M.; Chappell, W. J.; Noll, R. J.; Cooks, R. G., Quadrupole ion traps and trap arrays: geometry, material, scale, performance. *Eur. J. Mass Spectrom.* **2007,** *13* (1), 13-18.

39. Kornienko, O.; Reilly, P. T. A.; Whitten, W. B.; Ramsey, J. M., Micro ion trap mass spectrometry. *Rapid Communications in Mass Spectrometry* **1999,** *13* (1), 50-53.

40. Moxom, J.; Reilly, P. T. A.; Whitten, W. B.; Ramsey, J. M., Double resonance ejection in a micro ion trap mass spectrometer. *Rapid Communications in Mass Spectrometry* **2002,** *16* (8), 755-760.

41. Moxom, J.; Reilly, P. T. A.; Whitten, W. B.; Ramsey, J. M., Analysis of Volatile Organic Compounds in Air with a Micro Ion Trap Mass Analyzer. *Analytical Chemistry* **2003,** *75* (15), 3739-3743.

42. Blakeman, K.; Wolfe, D. W.; Cavanaugh, C. A.; Ramsey, J. M., Mass Spectrometry at Pressures Exceeding 1 Torr in a Microscale Cylindrical Ion Trap. **2014,** *In Preparation*.

43. Chaudhary, A.; van Amerom, F. H. W.; Short, R. T.; Bhansali, S., Fabrication and testing of a miniature cylindrical ion trap mass spectrometer constructed from low temperature co-fired ceramics. *Int. J. Mass Spectrom.* **2006,** *251*, 32-39.

44. Pau, S.; Pai, C. S.; Low, Y. L.; Moxom, J.; Reilly, P. T.; Whitten, W. B.; Ramsey, J. M., Microfabricated quadrupole ion trap for mass spectrometer applications. *Phys. Rev. Lett.* **2006,** *96* (12), 120801.

45. Blain, M. G.; Riter, L. S.; Cruz, D.; Austin, D. E.; Wu, G.; Plass, W. R.; Cooks, R. G., Towards the hand-held mass spectrometer: design considerations, simulation, and fabrication of micrometer-scaled cylindrical ion traps. *Int. J. Mass Spectrom.* **2004,** *236* (1-3), 91-104.

46. Cruz, D.; Chang, J. P.; Fico, M.; Guymon, A. J.; Austin, D. E.; Blain, M. G., Design, microfabrication, and analysis of micrometer-sized cylindrical ion trap arrays. *Rev. Sci. Instrum.* **2007,** *78* (1), 015107/1-015107/9.

47. March, R. E.; Todd, J. F. J., *Quadrupole Ion Trap Mass Spectrometry*. 2nd ed.; John Wiley & Sons: Hoboken, NJ, 2005.

48. Tian, Y.; Higgs, J.; Li, A.; Barney, B.; Austin, D. E., How far can ion trap miniaturization go? Parameter scaling and space-charge limits for very small cylindrical ion traps. *Journal of Mass Spectrometry* **2014,** *49* (3), 233-240.

49. Whitten, W. B.; Reilly, P. T. A.; Ramsey, J. M., High-pressure ion trap mass spectrometry. *Rapid Communications in Mass Spectrometry* **2004,** *18* (15), 1749-1752.

50. Arnold, N. S.; Hars, C.; Meuzelaar, H. L. C., Extended theoretical considerations for Mass resolution in the resonance ejection mode of quadrupole Ion Trap Mass Spectrometry. *Journal of the American Society for Mass Spectrometry* **1994,** *5* (7), 676-688.

51. Xu, W.; Song, Q.; Smith, S.; Chappell, W.; Ouyang, Z., Ion trap mass analysis at high pressure: A theoretical view. *Journal of the American Society for Mass Spectrometry* **2009,** *20* (11), 2144-2153.

52. Song, Q.; Xu, W.; Smith, S. A.; Gao, L.; Chappell, W. J.; Cooks, R. G.; Ouyang, Z., Ion trap mass analysis at high pressure: an experimental characterization. *J. Mass Spectrom.* **2010,** *45* (1), 26-34.

CHAPTER 2: THE STRETCHED LENGTH ION TRAP

Introduction

Quadrupole ion traps remained largely unchanged from their commercialization in 1984 until 2002, when the first linear ion trap (LIT) was reported by Hager[1] and improved by Schwartz *et al.* later that year.[2] Shown in Figure 2.1a, the LIT is simply a linear quadrupole with hyperbolic faces split into three segments. Ions are contained in the x and z dimensions by the RF potential as in the linear quadrupole but are now also contained along the y axis by holding the outer sections at a higher DC potential. Ions are scanned out of the trap in the same manner as the QIT, with ramping of the RF amplitude until ions become unstable and are ejected through slots cut into the rods. The symmetry of the electrodes results in ions being ejected in both x and z dimensions simultaneously so a resonant AC voltage is added to one rod pair, directing ejection only in the z dimension.

The linear trapping geometry operates under similar pressures as the QIT, and in addition has several major advantages over QITs. The most obvious advantage is that due to trapping of ions along a line rather than a point, the total ion capacity is greatly increased (near 40x for a commercial LIT),[2] making the LIT less sensitive to space charge effects. Second, by operating with opposite phase RF on each electrode pair, the potential along the y-axis is zero. Therefore, ion injection along this axis can be near 100% efficient. This is in stark contrast to the QIT where external ion injection is only a few percent due to its

dependence on RF phase. Lastly, because the ion source is orthogonal to ion detection, an electron multiplier detector can be placed at each of the two exit slots, making it possible to detect all ejected ions rather than just 50% as occurs in the QIT. All three of these benefits lead to the LIT being a more sensitive mass analyzer with a greater linear dynamic range than the QIT. The chief disadvantage is that fabrication and alignment tolerances are much tighter for the LIT because electric field variances across the whole of the y-dimension lead to deterioration of resolution.

The advantages of linear trapping soon led to the design of miniaturized LITs. Like the CIT approximates the QIT's hyperbolic surfaces, an analogous simplification can be made with the LIT to yield the rectilinear ion trap (RIT) shown in Figure 2.1b. The RIT uses four flat electrode surfaces to replace the hyperbolic rods of the LIT while using two additional flat plates with ion injection holes to cap the ends. The ion ejection slots are located far enough from these end plates that fringing fields do not affect the ejected ions. The RIT, first developed by the Cooks lab at Purdue,[3] quickly replaced the CIT as their focus for several generations of miniaturized mass spectrometers. The RIT combined with a pulsed inlet system[4] has led to a 5 kg mass spectrometer (external computer not included), albeit with low throughput.[5-6] However, compared to miniaturized CITs, the RIT used was relatively large with interelectrode distances in the 4-5 mm range. As outlined in Chapter 1, these large dimensions necessitate the use of low buffer gas pressures (*ca.* 1 mTorr) and turbomolecular pumps. Without substantial further miniaturization of the RIT to ease these vacuum requirements, it is unclear how an RIT based MS can be made significantly smaller.

Constructing a microscale RIT with its six electrode structure presents a much greater challenge, as its geometry does not lend itself to planar fabrication and 'electrode sandwich'

construction like microscale CITs.[7] Even so, several attempts have been made to miniaturize the RIT and RIT arrays to sub-millimeter scales using conventional construction,[8] metal plated polymer,[9-11] or printed circuit boards.[12] These efforts have resulted in traps as small as x_o = 1.3 mm with modest performance. Unfortunately, the diminishing performance in terms of resolution upon further miniaturization suggests that these techniques will be unsuccessful down to the scales necessary for high pressure operation. Several other geometries and advanced fabrication techniques have been used to miniaturize linear type traps,[13-16] but to date there have been no reports of these traps with critical dimensions below 1 mm.

This chapter describes a novel ion trapping geometry that combines several beneficial properties from both the cylindrical and rectilinear ion traps. It is essentially a modification of the CIT in order to trap ions linearly, gaining sensitivity while retaining the favorable manufacturing properties of the CIT. This geometry has led to the construction of the first micrometer scale linear type ion trap to be successfully fabricated and operated. The following is a detailed description of this work including the design, construction, and characterization of this novel ion trap at pressures up to and exceeding 1 Torr, i.e. the target pressure necessary for operation without turbomolecular pumps.

2.1 Concept

The new linear ion trapping geometry shown in Figure 2.2 is similar in construction and operation to the CIT but with the trapping volume stretched along a line orthogonal to the rotational symmetry axis. The resulting stretched length ion trap (SLIT) consists of a center electrode rectangular void that is truncated on each end by half-cylindrical voids. An RF potential is applied to this central electrode, trapping ions along the entire length of the

trap. In this manner, ions are confined along the y-axis by the same RF pseudopotential well confining ions in the x and z dimensions rather than by the DC potential well used in other linear traps. Due to its similarity to the CIT, the SLIT's central electrode will still be referred to as the "ring" electrode and the remaining two electrodes as the "endcaps." One option for SLIT endcap electrodes is to make the analogous modification to the CIT endcaps; that is, to make use of narrow slots for ion ejection. However, as alignment is already a concern for miniaturized CITs, the added alignment constraints from this configuration would be undesirable. Therefore, in place of ejection slots, planar mesh electrodes are used which require no alignment. Mass analysis can be carried out as with the CIT, by ramping the RF potential to sequentially eject ions from low to high m/z.

The many-fold increase in ion capacity is not simply due to the SLIT's larger volume but rather to its greater efficiency in ion storage. Thus even when using an array of CITs (a common method of increasing storage capacity) of the same footprint as a SLIT, the SLIT still holds significantly more ions. This efficiency increase stems from the relatively small size of the ion cloud when compared with the trapping volume, shown schematically in Figure 2.3. While there is debate over ion cloud size and density, since these parameters can change with RF frequency among other variables,[2] it is clear that as long as the ion cloud radius is significantly smaller than the trap radius (as it must be for a useful MS), the SLIT design can contain several times more ions than an equivalent footprint CIT array. What's more, just like the CIT, many SLITs can be operated in a parallel array to increase ion storage even further.

In summary, the increased dimensionality of the SLIT yields higher storage capacity than the CIT while the three electrode design maintains the same ease of fabrication and thus potential for extreme miniaturization, including arrays of trapping features.

2.2 General Operation

Instrumentation

A major limitation to conducting mass spectrometry at high pressures is ion detection. Nearly all MS instruments detect ions with an electron multiplier (EM) due to their high gain ($\sim 10^7$) and large bandwidth. Unfortunately, EMs begin to fail at pressures much above 10 mTorr due to autoionization of the background gas and they are therefore unsuitable for HPMS. High pressure ion detection will be the subject of Chapter 3, but for the initial SLIT work an electron multiplier was used inside a custom differentially pumped chamber. The chamber was designed such that the detection volume containing the EM can be pumped separately and kept to a lower pressure than the mass analysis volume. In this configuration, shown in Figure 2.4, the ion trap electrodes act as the gas conductance limit between the two chambers. The 'trap side' vacuum chamber was pumped using a TPS Bench pumping system (Agilent Technologies) consisting of a small turbomolecular pump (Turbo-V 81) backed by a dry scroll roughing pump (SH110). A similar system, the TPS Compact (Turbo-V 81, IDP-3, Agilent Technologies), was used to pump the detector chamber.

The instrument uses typical in-trap electron ionization (EI) to form and trap ions in which electrons from a heated filament (yttria coated disk emitter, ES-525, Kimball Physics) are guided and accelerated into the trap with sufficient energies to ionize neutral analyte molecules. The formed ions are then stably trapped in the pseudopotential well created by

the applied RF potential. After a set period of ionization, the electron beam is gated off with a mesh electrode in between the filament and trap. The ions are then allowed time to cool (via ion-neutral collisions) to the center of the trap before the RF voltage is ramped, ejecting the ions from the trap towards the electron multiplier detector (2300, DeTech). A timing diagram outlining this operation is shown in Figure 2.5.

A more complete control diagram showing the relevant inputs, outputs, and power supplies is given in Figure 2.6. All control voltages and data input/processing are handled via custom written LabVIEW software controlling National Instruments hardware (NI PXI-6733, NI PXI-6122). Starting with the ionization source, the filament current supply provides between 1.7 and 2.2 A of current to heat the filament to the point of electron emission. This filament is biased to typically -70 V relative to the trapping electrodes by another DC power supply to give the electrons enough kinetic energy for ionization. Both the electron gate electrode and the EM detection voltage are controlled by a custom high voltage pulsing circuit. The RF trapping signal is generated with an RF signal generator (HP8648A, Hewlett-Packard), amplified first by an RF preamplifier (603L, ENI), second by a custom built RF power amplifier (AR305), and finally voltage amplified up to as much as 1000 $V_{0\text{-}p}$ by a resonant tank circuit using an external inductor and the ion trap as the tank circuit capacitor. The axial RF voltage, up to 10 V in amplitude, is used directly from an arbitrary function generator (AFG3022, Tektronics). The current resulting from the EM amplification is then converted to an easily measurable voltage by a current-to-voltage preamplifier (SR570, Stanford Research Systems) at a gain of 200 nA/V.

Introduction and measurement of the sample and buffer gasses were controlled by a separate system. Sample gasses were introduced into vacuum via a precision leak valve

(ULV-150, MDC Vacuum Products) to pressures in the 10^{-5} Torr range. These pressures were measured via a combination Pirani/cold-cathode ionization gauge (FRG-700, Varian) and are reported as uncorrected values. Buffer gasses of helium or nitrogen were introduced via a mass flow controller (FMA5408, Omega) to pressures ranging from a few mTorr to 1 Torr. The buffer gas pressure was measured directly by means of a capacitance manometer (627D, MKS) with a 0.12% rated accuracy.

Initial SLIT Construction and Performance

The ring and endcap electrodes were fabricated by a combination of chemical etching and conventional machining. Copper sheet stock (800 μm thick) used for the middle electrode and beryllium copper sheet stock (250 μm thick) used for the endcap electrodes were patterned and chemically milled to the general shapes pictured in Figure 2.7. Ring electrode voids were then manually machined with endmills of various diameters yielding traps up to 6 mm long with x_o values in the 500 μm range. The endcap support electrodes were milled out to a wider diameter than the ring electrode void before 80 lines per inch, woven stainless steel mesh was soldered across the opening. A spacing of 250 μm between endcap and center electrodes was achieved with Kapton® polyimide washers yielding traps of z_o = 600 μm including the thickness of the mesh.

After confirming that this new trap design did indeed function as a mass analyzer (the green trace in Figure 2.8), the first step taken was to determine the optimal geometrical characteristics, most notably the z_o/x_o ratio. The analogous z_o/r_o ratio for the CIT has been studied previously[7, 17-18] and not surprisingly has been found to be different than the ideal value for a QIT of 0.707. Prior studies all report values greater than or equal to unity while

our own laboratory's CIT research suggests the optimal ratio is near 1.3. To determine an optimal ratio for the SLIT geometry, traps with varying z_o/x_o ratios were fabricated by machining three separate ring electrodes to x_o values of approximately 585, 500, and 470 µm. All three were machined to a length, $2y_o$, of 6 mm and constructed such that z_o = 600 µm, yielding z_o/x_o ratios of 1.03, 1.20, and 1.27, respectively.

Xenon gas was used to characterize trap performance because its distinctive stable isotope pattern can be used to qualitatively and quantitatively evaluate trap resolution. All three traps were run under similar conditions in 10 mTorr helium buffer gas and 0.055 mTorr xenon sample gas with 1 ms of ionization at an emitter current of 1.7 A. The RF frequency was held constant at 6.4 MHz while axial RF conditions were adjusted for each trap to maximize resolution but was always near the hexapolar resonance (~1/3 the RF drive frequency) shown to work the best with a CIT. Mass spectra were collected as averages of 1000 individual scans, low pass filtered at 50 kHz to remove high frequency noise associated with electron multipliers, and manually mass calibrated by choosing two peaks of known mass. The resultant data shown in Figure 2.8 clearly shows an improvement in resolution as the z_o/x_o ratio is increased up to 1.27 at which all seven stable isotopes of Xe are able to be distinguished. This shows that the optimal ratio is very similar to that of the CIT and also agrees quite well with the z_o/x_o ratio determined for the RIT of 1.25.[3]

Xenon is an atomic ion and cannot therefore undergo fragmentation due to leftover energy from ionization which occurs for the majority of molecular analytes. Fragmentation can complicate the characterization of mass analyzers because the fragmentation patterns can change based on experimental conditions. For this reason, xenon is the analyte of choice for the majority of data presented in this chapter. However, the narrow mass range of the xenon

isotope peaks could possibly mask issues with mass biases or non-linear mass scans, so spectra of organic analytes with fragmentation patterns covering a wider mass range were also taken. Shown in Figure 2.9 is an example, a spectrum of methyl salicylate (MES) chosen due to its relevance as a chemical warfare simulant. This spectrum was taken with the higher resolution ($z_o/x_o = 1.27$) trap under identical experimental conditions as above save for the wider mass range. The spectrum serves as evidence that the SLIT can detect ions over a useful mass range for ambient organic analysis, also demonstrating that the same mass fragments as in the NIST standard spectra appear, but not necessarily at the same relative intensities. This is not unexpected since the rates of fragment ion formation depend on the energetics of the ion source and experimental time scale, which are different for the linear quadrupole instruments used to generate the NIST data. It should be noted that performance of the SLIT while analyzing a much broader variety of organic analytes will be presented in Chapter 5.

The final experiment of the initial SLIT characterization explored the ion trapping capacity versus SLIT length, which is expected to follow a linear trend. In this case, SLITs with z_o/x_o ratios of 1.27 machined to lengths ($2y_o$) of 2, 3, 5, and 6 mm were operated under identical conditions in order to directly compare signal intensities from 0.15 mTorr of xenon analyte in 10 mTorr of helium buffer gas. The integrated signal from each trap plotted as a function of trap length shown in Figure 2.10 indeed shows a linear dependence with a $R^2 = 0.9944$. This data further illustrates the promise of the SLIT as a microscale ion trap; it suggests that as the traps are made ever narrower in width, the relative gain in signal of a SLIT versus a CIT with the same critical dimensions will continue to increase, assuming a constant trap length, y_o. Again, it should be recalled that moving to ever smaller dimensions

and correspondingly higher frequencies in greater pressure tolerance and/or higher resolution.

Performance Improvements and Comparison to CIT

While the initial performance of the SLIT was promising, the peak widths were wider than the typical sub 0.5 Th widths obtained with CITs operated under similar conditions. This result was most likely due to electrode fabrication imperfections in both the ring and endcaps. To improve ring electrode fabrication, the central feature was milled with a precision CNC Micro Mill followed by wet sanding with high grit sandpaper to remove any remaining burrs. The improvements, especially in the semicircular end features, can be seen in comparison to the manually machined electrodes in Figure 2.11. Also shown is the third method of fabrication explored, wet chemical etching. The most notable difference is the cusp feature formed inside the etched electrode void as a result of the isotropic nature of the etching. Interestingly, prior work in our lab with etched CITs suggests that this cusp feature might actually result in higher performance.[19] This is fortunate as chemical etching can be low cost due to batch processing and is the preferred method for making trap features much smaller than 500 μm.

An important improvement was also made to the mesh endcap electrodes. The initial woven mesh used produced a rough surface relative to the scale of the trap and made it difficult to maintain a precise flat surface while soldering to the support electrode. To alleviate these issues, new endcap electrodes were designed with a simple 5 mm diameter hole in the center and were then sent offsite to have 200 line per inch electroformed, non-woven copper mesh stretched and bonded to them by means of electrodeposition (Precision

Electroforming). A close up view of the resulting electrodes in Figure 2.12 shows a flat and uniform surface. Additionally, this mesh has a greater percentage of open area than the original woven mesh, leading to greater electron and ion transmission and resulting in improved sensitivity.

The fabrication improvements result in creation of a more precise trapping field, leading to improvements in resolution. Using the CNC machined electrodes and electroformed mesh endcaps, the SLIT was able to achieve comparable resolution to a CIT as shown in Figure 2.13. The SLIT ($2y_o$ = 5 mm) and CIT in this comparison had identical critical dimensions of z_o = 650 μm and $x_o = r_o$ = 500 μm, a ratio of 1.30. Additionally, the same set of electroformed mesh endcaps were used for both traps to obtain as direct a comparison as possible. Xenon was again used as the sample and was leaked in to a pressure of 0.10 mTorr in 35 mTorr of helium buffer gas. Identical ionization and mass analysis conditions were used with the exception of tuning the axial RF to slightly different values to obtain maximum resolution for each trap. Very near baseline resolution was obtained with both traps for all seven stable isotopes of xenon corresponding to average peak widths of 0.41 Th and 0.44 Th for the SLIT and CIT, respectively. Also of note in this data is the higher signal-to-noise ratio for the SLIT spectrum. This illustrates the sensitivity increase stemming from the greater trapping capacity of the SLIT.

The increased sensitivity of the SLIT over the CIT was quantified as well. The same experimental conditions previously used to compare the resolution of the two traps were repeated, but this time spectra were taken with each trap while increasing the xenon pressure. The integrated signal taken across all xenon peaks was plotted versus xenon pressure to yield a calibration curve for each trap shown in Figure 2.14. The sensitivities of the SLIT and CIT

were 5.4 and 0.52 μV·s/Torr, respectively, making the SLIT 10X more sensitive in this case. To consider experimental variance, this experiment was repeated at a single xenon pressure (0.12 mTorr) for three traps of each type. This data agreed well with the original calibration curves generated, with a signal increase of 10.4 ± 3.8 times for the SLIT as shown in the Figure 2.14 inset.

High Pressure SLIT Operation

As discussed in Chapter 1, a vital aspect of a handheld mass spectrometer is the ability to conduct mass analysis at high background pressures in order to reduce vacuum pumping requirements. CIT operation at pressures up to and exceeding 1 Torr have been previously demonstrated in our laboratory[20] and peak widths have been found to be directly proportional to pressure as expected from eq 1.22. Again, it is expected that the SLIT geometry should closely follow the CIT performance as pressure is increased due to their similarities.

Before SLIT performance could be studied as a function of increasing pressure, an instrumental modification was required in order to maintain a suitably low pressure for the electron multiplier. The relatively small endcap apertures used with the CIT (0.4 mm diameter) acted as a strong gas conductance limit, restricting the detector pressures to a few mTorr when the trapping pressures were 1 Torr. Comparatively, the large gas conductance offered by the SLIT with its mesh endcaps results in detector pressures in the hundreds of mTorr range. To maintain greater differential pressure, a 5 mm long, 200 μm wide slot feature was machined into a blank endcap electrode and placed directly behind the rear endcap of the SLIT. In this manner, ejected ions are allowed to pass through to the detector

while the narrow slot provides enough of a conductance limit to maintain low detector pressures as the trap pressure is raised. While this configuration almost certainly reduces the trap's sensitivity due to some population of the ejected ions being lost to this new electrode, its effect on resolution, the parameter of interest, should be negligible.

A 5 mm long, x_o = 500 μm SLIT run at 6.4 MHz RF frequency was used with the above conductance modification to acquire xenon spectra at buffer gas pressures ranging from 200 to 1000 mTorr of helium. It should be noted that the buffer gas pressure was increased by adjusting the flow of helium into the chamber rather than restricting the pumping speed. This adjustment keeps the number density of analyte molecules constant while decreasing the concentration in terms of parts per million. Another requirement for performing high-pressure mass spectrometry is the adjustment of filament emitter conditions as increased buffer gas pressure drastically reduces the amount of ionizing electrons in the trap. This reduction is due to the increased buffer gas collisions cooling the filament electron emitter (emission is proportional to temperature squared) as well as scattering of the emitted electrons before they reach the trap. These effects are compensated for by respectively increasing the filament current to increase its temperature and by increasing the magnitude of the filament bias to -250 V, resulting in a stronger field to guide ionizing electrons towards the trap. Due to these conflating factors, it is difficult to separate their individual effects on signal intensity and thus no attempt was made in these experiments to keep the number of trapped ions constant. Therefore the signal-to-noise ratios of the resulting spectra shown in Figure 2.15 should be understood to be the result of factors other than the buffer gas pressure. When considering the effect of pressure on spectral resolution, the data show deterioration

similar to that of the CIT as expected, ranging from the sub 0.5 Th peak widths seen in Figure 2.13 to the ~1.5 Th FWHM peak widths at 1 Torr.

All the data presented thus far has been taken using helium buffer gas which is exclusively used in ion trapping instruments due to its low mass. Because all organic analytes are at least several times the mass of helium, each individual collision in the trap has a relatively small effect on the motion of an ion and the multitude of random collisions as a whole can thus be modeled well as a drag force, efficiently cooling the ion motion to the trap's center. However, helium is not readily available in the field and thus its use necessitates the addition of a high pressure tank to a portable instrument. A much more desirable buffer gas for portability would be nitrogen as it is readily extracted from ambient air. The ideal case would be to use ambient air as a buffer gas which requires no purification and has the added benefit of making sample introduction straight forward. A possible concern for the use of air rather than nitrogen is that the more reactive oxygen might undergo in-trap ion-molecule reactions causing unknown and possibly unpredictable peaks to arise in the mass spectra. Fortunately, our laboratory's research into MS in air has thus far showed no evidence of this phenomenon, finding spectra taken in air and nitrogen buffer gasses to be functionally identical. However, as the mass of nitrogen (and the approximate average mass of air) is 7X higher than that of helium, significant peak broadening was seen to occur due to increased ion scattering from collisions with the buffer gas.

A similar setup to the high pressure helium work, including the same trapping electrodes, was used to study SLIT performance in nitrogen buffer gas. However, because electron multipliers are even less pressure tolerant with respect to nitrogen, the EM was replaced by a simple Faraday cup detector with a commercial charge sensitive amplifier

("CoolFET" A250CF, Amptek). This and other Faraday cup detector systems are the subject of Chapter 3 and will be covered in detail therein. In this experiment, the analyte mesitylene (1,3,5-trimethylbenzene) was leaked into the chamber to a pressure of 0.11 mTorr before nitrogen buffer gas was introduced to a pressure of 9 mTorr. After collecting spectra at this pressure, the vacuum pumping speed was reduced incrementally by means of a conductance limiting valve to achieve pressures of 89 and 1000 mTorr. The increase in peak width upon moving from helium to the heavier nitrogen buffer gas is apparent from the resulting spectra shown in Figure 2.16. These peak widths are again found to be similar to that of a CIT operated at the same pressures.

Clearly, these large peak widths on the order of 6 Th stemming from the use of nitrogen buffer gasses will result in a mass spectrometer of less utility than its benchtop counterparts. However, operation in nitrogen or air buffer gasses remains a necessity for creating the smallest, most portable instrument possible. A tradeoff between portability and performance is a common theme to this research and while some amount of utility is lost with miniaturization, this level of performance is already on par with competing miniaturized instrumentation, namely IMS. However, efforts are already underway to reclaim some of the lost selectivity that comes with the lowered resolution in the form of GC separation prior to mass analysis and resolution improvements by increasing the RF frequency, both of which will be discussed later in this dissertation.

To summarize the initial SLIT characterization, the stretched length ion trap provides an order of magnitude higher sensitivity than the CIT while showing similar resolution through the entire pressure regime studied in both helium and nitrogen buffer gasses.

2.3 Alternative SLIT Configurations and Tolerance Studies

This section presents research exploring trap configurations beyond that of a single element SLIT. To further increase the ion storage capacity and thus sensitivity, SLIT arrays and serpentine configurations were explored. This research led to a more detailed investigation of how ion storage and ejection are affected by geometry.

SLIT Arrays and Serpentine Traps

Like the CIT, it is straightforward to construct arrays of SLIT elements to be operated in parallel with the aim of further increasing charge capacity. This objective was accomplished by simply machining several SLIT elements adjacent to one another in the same central electrode with a single mesh electrode forming an endcap for each trapping volume. Theoretically, as long as equal numbers of ions are formed in each trap, an array with N traps should have a signal intensity increase of N times the signal of a single trap. However, this assumption only holds if each array element is identical. Trap to trap variability will cause ion ejection at slightly different points in time for each trap element leading to deterioration in both resolution and signal intensity. This limitation makes fabrication tolerances much more important for arrays than for single traps.

Another concern for ion trap arrays is that individual trap elements will all contain differing numbers of trapped ions due to variations in the ionizing electron flux across the array. Space charge effects that occur when many ions are simultaneously trapped can shift ion ejection based on the amount of charge stored, thus again deteriorating signal intensity and resolution for arrays storing varying amounts of charge. A modified SLIT geometry in which SLIT array elements were connected end to end in a serpentine pattern was developed

in response to this concern. The idea behind this serpentine trap is that as ionization occurs unevenly, the ions are free to redistribute through the entirety of the trap volume resulting in a uniform charge density. Thus any effects due to space charging occur evenly throughout the trapping volume so as not to deteriorate resolution. Images of both the SLIT array and serpentine trap can be seen in Figure 2.17 in addition to xenon spectra of each taken in low pressure (30 mTorr) helium to illustrate the traps' resolution. Both trap geometries exhibited similar peak widths that are similar to those obtained with a single element SLIT from Figure 2.13, near 0.5 Th FWHM.

For the serpentine trap to have any advantage over a SLIT array, ions must freely distribute along the trap's length on a timescale relevant to the mass spectrometry experiment, that is less than a few milliseconds. An experimental setup shown in Figure 2.18 was developed in order to explore this ion travel. As depicted, a grounded copper electrode was placed between the ion source and the trap to prevent ionization from occurring in the bottom two thirds of the trap. A second grounded electrode was placed between the trap and the detector to neutralize ejected ions from the top two thirds of the trap. With this configuration the only way to observe ions at the detector is for ions to be formed in the top third of the trap and travel to the bottom third before being ejected. A mass spectrum of xenon in 30 mTorr helium taken in this manner is shown in Figure 2.18. No difference in the spectra was observed upon varying the time between ionization and ion ejection from 10 ms down to 1.6 ms, suggesting that the ions effectively distribute themselves across this 15 mm of trap length faster than 1.6 ms.

While the serpentine trap performed as expected, little further work was attempted with this geometry for two main reasons. First, there was concern for the long, unsupported

electrode areas between the trapping channels creating a cantilever effect, reducing the trap's durability. More importantly, further research has shown that even up to the space charge limit of the traps, the changes in resolution or ejection times observed have remained small, especially when compared to the peak broadening effects of high pressure. Therefore, the simpler SLIT array geometry was found to be a more appropriate way to increase trapping capacity. The discussion on the serpentine trap research above was included largely because it illustrates in a simple manner how ions can move freely and rapidly along a linear type trap's central axis.

SLIT Tolerance Considerations

As mentioned earlier, dimensional tolerances are tighter for the linear ion trap compared to 3D traps due to the requirement that all four rods must be strictly parallel to one another. This issue is somewhat reduced in the case of the SLIT as the electrode surfaces defining the x-dimension are locked in a parallel configuration since they are machined into the same electrode. Additionally, the mesh electrodes eliminate several degrees of freedom, namely x and y linear movement and z-axis rotation. Therefore there is only a single parameter left to consider upon trap construction, the degree to which the ring electrode and endcaps are parallel to one another, i.e. the z_o dimension uniformity. As with all quadrupole trap tolerances, the squared dimension terms in equations 1.15 and 1.16 result in even minor dimensional variations having significant effects on trap resolution.

An example of how a variation in z_o across a SLIT array can affect the spectra generated can be seen in Figure 2.19 where once again xenon analyzed in 30 mTorr helium buffer gas was used to qualitatively access trap resolution. In the first spectrum shown, care

was taken to construct the three element SLIT array such that the electrode stack was as close to parallel as possible (matched Kapton spacers and equal torque applied to mounting screws). The second spectrum was generated by taking this same trap and simply over-tightening the upper screw as indicated. This introduced a slant in the endcaps relative to the ring electrode so that the z_o dimension decreases across each of the three trap elements. The result is that the normal xenon spectrum from the parallel endcap trap splits into several distinct xenon spectra in the slanted endcap trap due to ions being ejected at different voltages in each trap element. The difference in z_o between the array elements can be estimated from the peak splitting distance to be on the order of 5 μm. These results illustrate how dimensional variations across array elements can lead to significant deterioration in resolution.

In a similar manner to arrays, variations in z_o across a single SLIT should also lead to poor resolution. The previous experiment was repeated for a single SLIT with similar tightening of one mounting screw in order to vary the z_o across the trap's length. However, the expected peak broadening was not observed from this ~5 μm slant. The endcaps were then further slanted to a total z_o change of ~80 μm by the addition of extra Kapton spacers as indicated in Figure 2.20, but the resulting spectrum remained identical to that of a trap with parallel endcaps. This puzzling lack of sensitivity to z_o variation across the length of the trap led to the conclusion that ions must not be ejecting evenly across the trap's length, rather they eject from a narrow enough portion of the trap across which the z_o variation is not significant enough to degrade resolution. This hypothesis was tested by using a grounded electrode between the trap and detector to block ion ejection from each half of the SLIT independently and comparing the resulting spectra. Figure 2.20 is the result of these

experiments. A spectrum from the unmodified SLIT with parallel electrodes (top) is compared with spectra resulting from traps with slanted endcaps (middle). Even though ion ejection is blocked from the right half of the slanted traps, the signal intensity and resolution are nearly equivalent to the parallel trap. This suggests that the vast majority of the ions are ejected from the left half of the trap no matter the endcap slant. This is confirmed by moving the blocking electrode to cover the left half, resulting in no spectra observed for the bottom trace in Figure 2.20. In other experiments, ion ejection continued to occur from the same half of the ring electrode when it was rotated relative to the endcap, suggesting that this localized ejection is a result of some property of the ring electrode as opposed to the endcaps.

In summary, ejection of ions from a SLIT follows the well-established quadrupole trapping equations (eqs 1.15 and 1.16) as evidenced by shifting of the ejection voltage with varying z_o dimensions. However, ions are observed to eject from a narrow area of the SLIT, causing ions to eject with good resolution even as trap dimensions vary across the length of the SLIT. As this is a fairly interesting phenomenon, a new experimental apparatus was developed in order to further study ion ejection profiles from linear type traps.

Ion Ejection Profiling

In order to efficiently study ion ejection profiles from various traps, a new experimental setup was devised to precisely measure the ion ejection profile across the entirety of the trap length without the need to break vacuum. In contrast to the experiments described thus far, this setup was built in a single 6" ConFlat vacuum chamber in which ion source, trap, and detector were all held at a single pressure. This chamber was chosen so that the apparatus depicted in Figures 2.21 and 2.22 could be constructed easily on a single 6"

flange. The operative portion of this setup is a thin, grounded electrode placed between the trap and detector, spanning the length of the ion trap. This electrode is solid with the exception of a 1 mm slot that can be slid across the trap's length, allowing ions ejected from each small segment of the trap to reach the detector independently. This electrode is able to slide freely back and forth by means of a miniature cart and rail system mounted above the trap (9829K1 and 9829K11, McMaster-Carr). The cart position is in turn controlled by a rack-and-pinion structure (57655K61 and 57655K13, McMaster-Carr) mechanically linked outside the vacuum chamber by a 1/4 brass shaft and Ultra-Torr vacuum fitting. Thus by rotating this shaft from outside the vacuum chamber, the cutout portion of the grounded electrode slides across the entire trap length.

With the aim of determining how different buffer gas conditions affect the spatial distribution of ion ejection, experiments were conducted in helium and nitrogen buffer gasses at both low and high pressures, and general conditions for each will now be described. Xenon was once again used as the analyte due to its narrow mass range and absence of fragmentation. For all experiments, the trapping RF voltage and the maximum RF ramp voltage remained the same and were produced at a frequency of 6.51 MHz. For helium buffer gas experiments, a hot cathode electron emitter was used for ionization as before, while a glow discharge electron source was used for the nitrogen buffer gas experiments. The glow discharge source provides a greater flux of electrons at high pressures than a filament emitter and will be discussed in further detail in Chapter 4. An electron multiplier was used for low pressure experiments, and the same Faraday cup detection system referenced in Section 2.2 was used for the high pressure experiments. In each profiling experiment, a spectrum was taken with the center of the 1 mm electrode void at a position of

-2.5 mm relative to the SLIT's center. Spectra were then taken after translating the electrode void 0.625 mm for each spectrum until the final position of 2.5 mm relative to the SLIT's center was reached, yielding nine spectra collected across the trap's length.

The first traps profiled were several conventional, i.e. x_o = 500 μm, SLITs in low pressure helium (30 mTorr) in an attempt to reproduce the localized ejection observed in Figure 2.20. Results indicate that although all traps were fabricated using the same procedure, each trap exhibited differing ion ejection profiles including single ejection location, bimodal distributions, or more uniform ejection across the trap. However, when operated in more relevant 1 Torr nitrogen buffer gas conditions, these traps all exhibited roughly the same uniform ion ejection across the trapping length. This change in ejection distribution is attributed to greater ion scattering due to the larger mass of nitrogen. An example of a SLIT ion ejection distribution converting from a bimodal distribution in low pressure helium to a uniform distribution in high pressure nitrogen can be seen in Figure 2.23a. The ejection 'hot spots' observed in low pressure helium are not entirely surprising as full size linear type traps with poor tolerances have also exhibited this behavior.

Although it would be beneficial to control the ion ejection location, these initial experiments made no attempt to do so. As evidenced by the 'endcap slant' experiments of the previous section, a trap design that consistently ejected ions from a small portion of the SLIT would be much more tolerant to variations in trap dimensions due to construction inconsistencies. As prior evidence suggests that ejection distributions were produced by ring electrode imperfections, a modification was made to the SLIT, purposefully introducing a ring electrode artifact by enlarging one end as pictured in Figure 2.23b. The resulting ion ejection profile indeed shows ~90% of the total ion signal being ejected near the electrode

artifact for low pressure helium. However as with the unmodified SLIT, upon switching to nitrogen buffer gas a similar ejection distribution smoothing effect was seen. As shown, the strong spatially specific ejection was moderately suppressed at low pressure nitrogen (15 mTorr) and was suppressed to a greater extent in high pressure nitrogen (1 Torr), reducing the effect of the SLIT modification.

Several other modifications to the SLIT geometry were studied with the trap profiling setup to varying degrees of success. One geometry yielded particularly interesting results in high pressure nitrogen and will be discussed here. In place of the standard SLIT ring electrode, a 10% tapered ring electrode design was fabricated in which the x_o dimension varied linearly from 500 µm on one end of the SLIT to 550 µm on the opposite end. The ion ejection profile shown in Figure 2.24 exhibits a large preference for ejection from the narrow end of the SLIT with a decrease in intensity moving toward the wider end. There are two possible explanations for this behavior with the first being that ion storage density in the trap mirrors the ejection distribution, and the ions are simply ejected from their storage location. The second explanation is that trapped ions are able to freely move along the trap's length, rapidly sampling the entire trapping area. This mobility still leads to preferential ejection from the narrow end because as the trap dimensions change along its length, an ion's q_z value becomes location dependent, and ions will simply eject from the portion of the trap in which its q_z is first equal to the ejection point ($q_z = 0.908$), i.e. the narrow end of the tapered electrode.

In order to determine the correct explanation an experiment was conducted to discern the distribution of trapped ions prior to ejection. In this case, the ions were held at a constant RF trapping potential and positive DC pulse with fast rise time (~100 ns) was applied to the

front endcap, rapidly ejecting all ions in the location in which they were stored. The ejection profile of this experiment (Figure 2.24) shows a symmetric distribution about the center of the SLIT. This provides good evidence that the second explanation is correct, that stored ions rapidly sample the entire trap area and preferentially eject from the location in which their q_z first reaches 0.908. Since there is a limited time in which $q_z > 0.908$ on the narrow end of the trap and $q_z < 0.908$ on the wide end (~100 μs), it is clear that ions must regularly traverse the trap distance on the order of this timescale. This agrees well with the data from ion travel in the serpentine trap presented earlier. It should also be noted that this distribution remains unchanged when varying the trapping RF potential, suggesting that the pseudopotential well depth the ions are trapped in has little effect on their y-dimension motion within the trap.

To summarize this section of trap profiling experiments, it is possible to control the ion ejection 'hot spots' in a SLIT by making geometrical modifications to the ring electrode. However, when moving from low pressure helium to high pressure nitrogen buffer gas, the ejection profiles are largely smoothed out, making this strategy less effective under the most desired operating conditions, high-pressure operation. Finally, ions appear to be stored relatively evenly throughout the trap but can still be preferentially ejected from one location over another due to their movement through the trapping area being rapid in relation to the experiment timescale.

2.4 Conclusions

The novel stretched length ion trapping geometry is an effective design for the fabrication of linear type quadrupole ion traps in the microscale regime. The SLIT

geometries exhibited a tenfold increase in sensitivity over cylindrical ion traps with the same critical dimensions, and arrays of SLIT features can be used to increase device sensitivity even further. The SLIT spectral resolution under low and high pressure buffer gasses of both helium and nitrogen was also consistent with previously characterized CIT performance. Modifications to the ring electrode geometry have the ability to effectively control ion ejection location under low pressure buffer gas conditions, possibly leading to devices with wider fabrication tolerances. However, as this ability to control the ejection location is greatly diminished when moving to high pressure nitrogen or air buffer gasses, standard geometry SLIT arrays remain the trap of choice for a hand portable instrument.

2.5 Figures

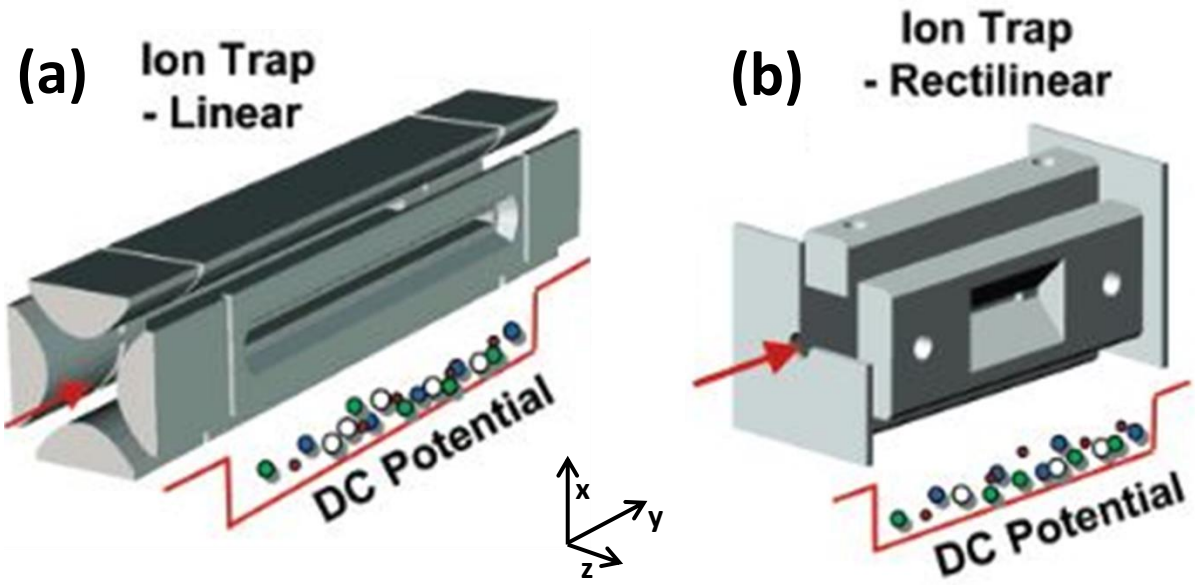

Figure 2.1: Graphical depictions comparing (a) the linear ion trap and (b) rectilinear ion traps. The relationship between the LIT and RIT is analogous to that of the QIT and CIT depicted in Figure 1.5 where the complex hyperbolic electrode shapes are replaced by flat electrode surfaces in order to facilitate miniaturization. Both of these traps utilize a DC potential well in order to trap ions along their axis and an RF pseudopotential well created by applying 180° out of phase RF voltages to adjacent electrodes to trap ions in the other two dimensions. Red arrows depict where ions are typically injected.

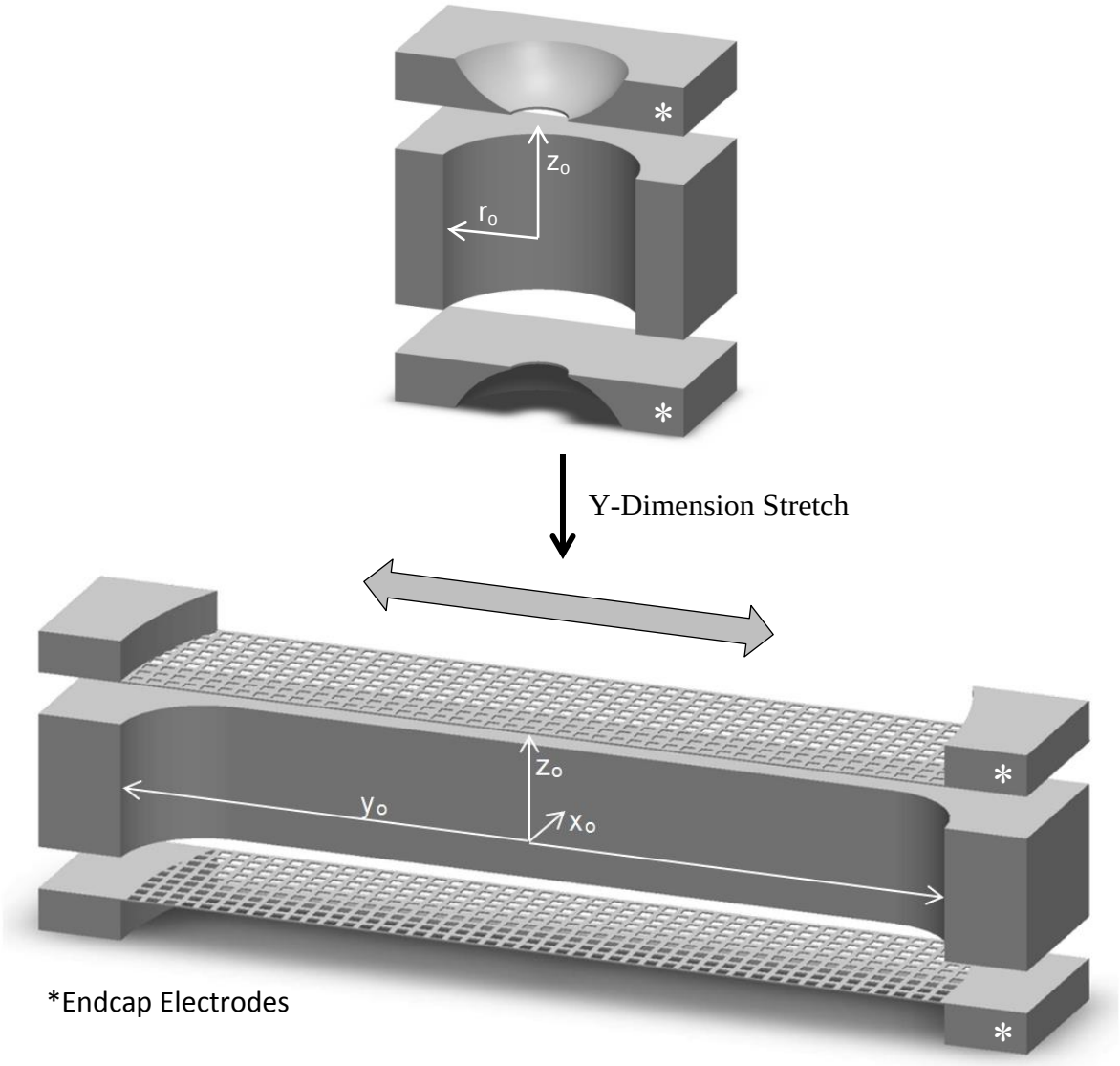

Figure 2.2: Graphical depiction of the formation of the stretched length ion trap formed by taking the CIT geometry and stretching the trapping volume along a direction perpendicular to the z-axis, greatly increasing the ion trapping capacity. In contrast to the RIT, the SLIT is constructed of three rather than six electrodes making it possible to be miniaturized even further. An RF potential is applied only to the middle ring electrode forming a trapping field in combination with the grounded endcaps. Electrons are injected along the z-axis, forming ions inside the trap as in CIT operation. Trapped ions are free to move along the y-axis inside the trap but are confined at the ends by the same RF trapping field as the x and z dimensions.

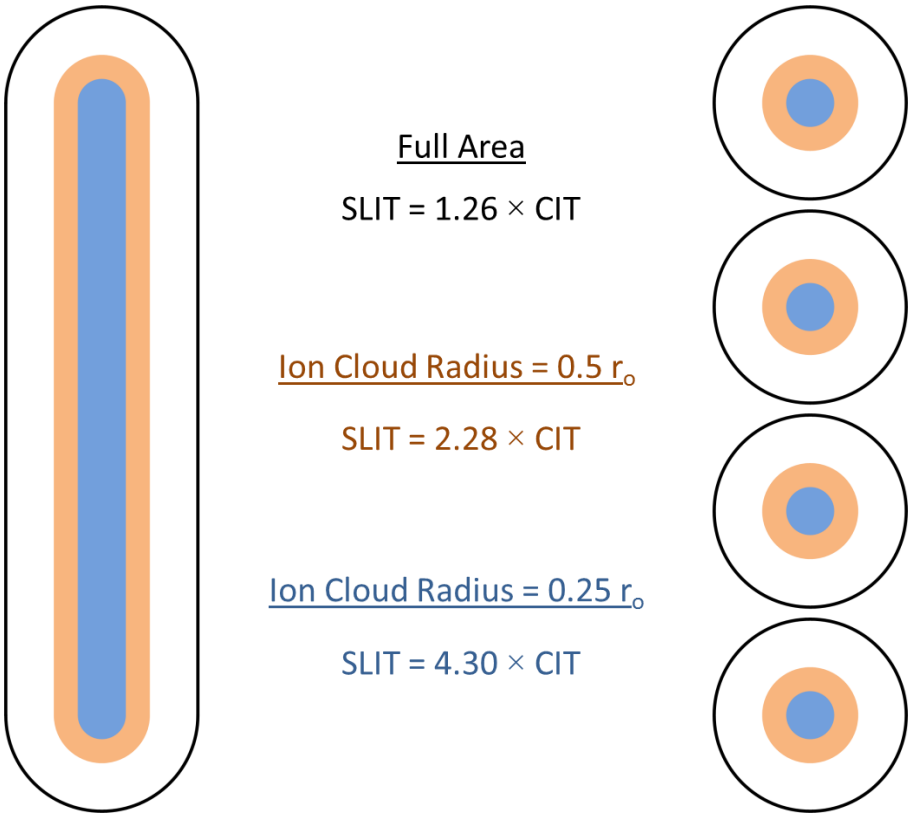

Figure 2.3: Graphical depiction of the increased ion trapping efficiency of the SLIT vs. a CIT array of equal footprint. The orange area represents an ion cloud of half the radius of the trap while the blue area represents an ion cloud of one quarter the radius of the trap. As the ion cloud radius shrinks from 0.5 r_o to 0.25 r_o, the relative trapping efficiency of the SLIT over the CIT array increases from 2.28X to 4.3X. Actual ion cloud radii vary based on conditions such as operating pressure and RF frequency. Ion clouds are also not of uniform density, making this graphic a simplified illustration of how a linear geometry more efficiently stores ions.

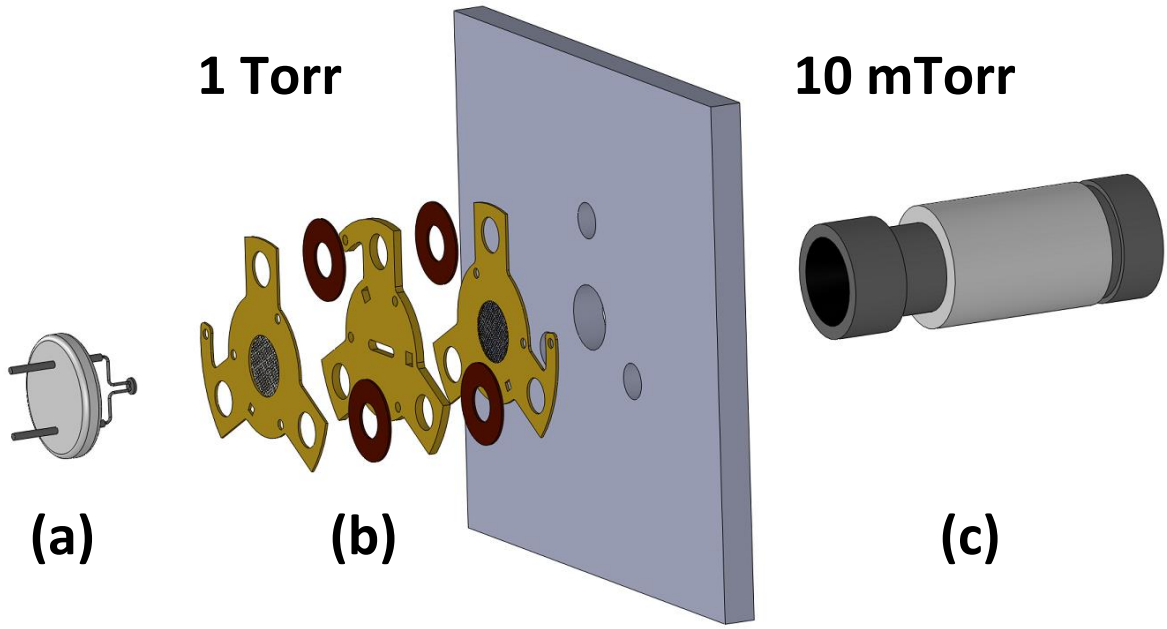

Figure 2.4: An exploded view of the differential pressure chamber used to conduct the SLIT testing showing (a) a thermionic electron emitter for ionization with the mesh gate electrode omitted for clarity, (b) the SLIT electrode stack with Kapton spacers, and (c) the electron multiplier detector. The vacuum pumping of the chamber is such that the ion source and ion trap region on the left can be held at up to 1 Torr of background pressure while still maintaining the low pressures needed for electron multiplier operation on the right.

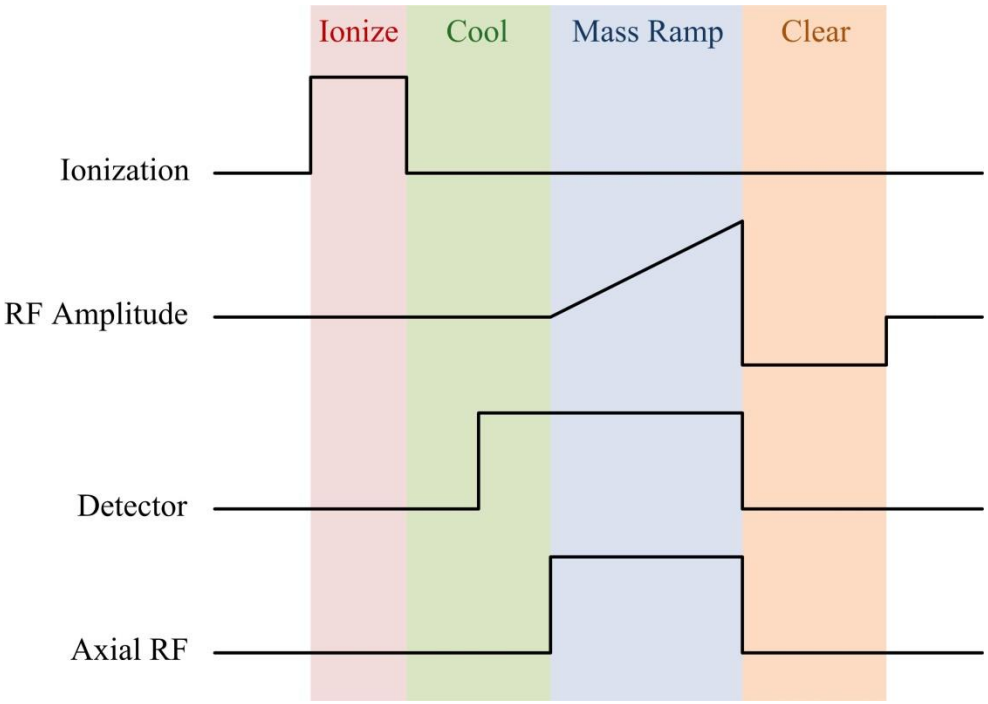

Figure 2.5: Timing diagram of a typical MS experiment showing the four phases of operation and associated control signal changes with time. The relative lengths of these phases vary with the type of experiment but their sum is typically on the order of 10 ms. During the ionization phase, electrons are accelerated into the trap to ionize analyte molecules, the RF amplitude is kept at a trapping potential where a wide range of ions can be trapped, and the detector high voltage is kept off to avoid detector saturation. The detector is turned on during the cooling phase to prepare for ion detection during the mass ramp. After the RF amplitude ramp is complete, the RF level is dropped below the trapping potential to clear any remaining ions from the trap before starting the cycle over again. The optional axial RF voltage, used to improve signal level and resolution, can be run in pulsed mode as shown or run continuously.

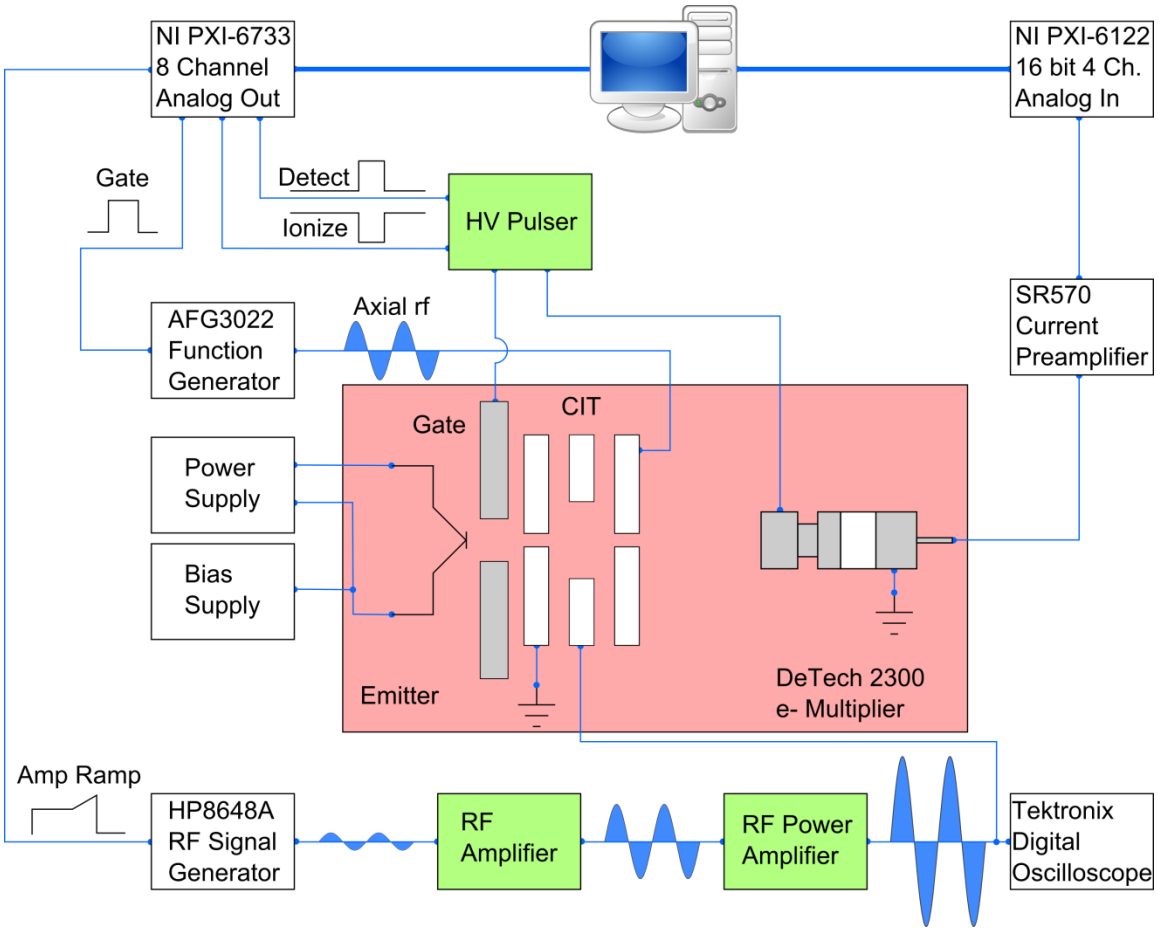

Figure 2.6: Complete control diagram of the instrument used with the pink highlighted section representing components inside the custom vacuum chamber.[19]

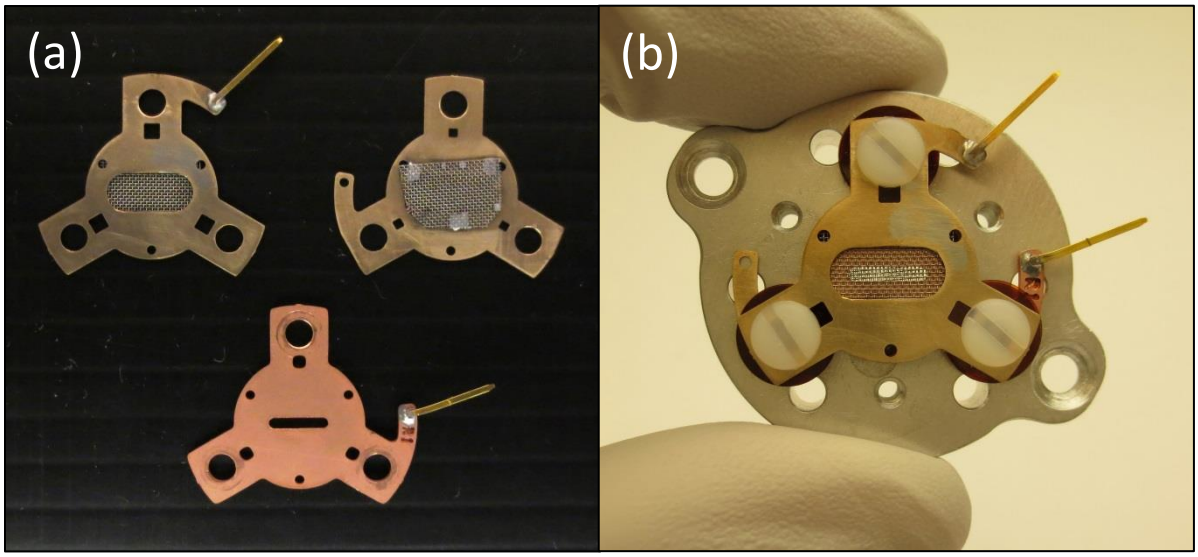

Figure 2.7: Photographs of early versions of the beryllium copper endcap electrodes and SLIT copper ring electrode (a) showing the soldered stainless steel endcaps. Also pictured is a fully constructed SLIT (b) with Kapton spacers, nylon mounting screws, aluminum trap mount, and soldered pins for electrical connections.

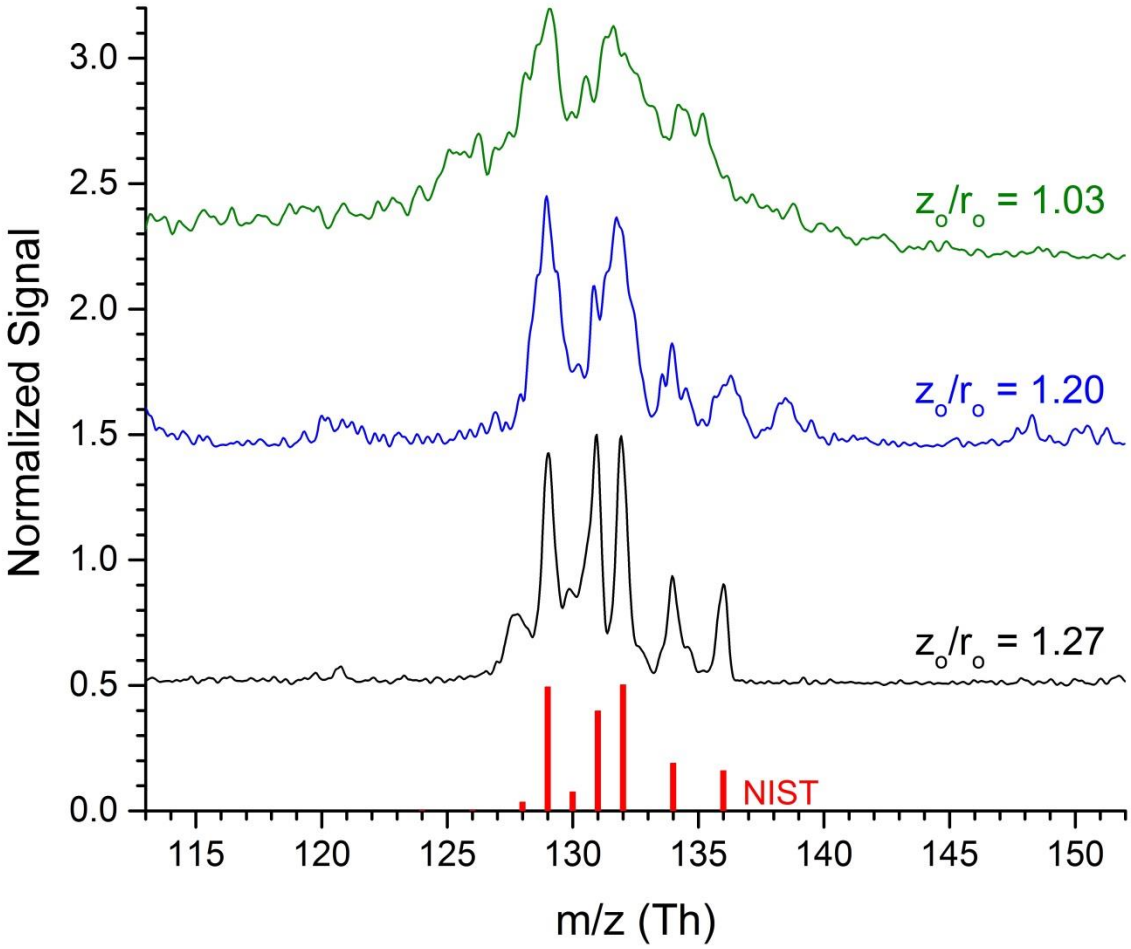

Figure 2.8: Spectra of 0.055 mTorr xenon gas in 10 mTorr helium buffer gas taken using an RF frequency of 6.4 MHz and SLITs with z_o/r_o ratios of 1.03 (green), 1.20 (blue), and 1.27 (black). The NIST standard spectrum for the major xenon isotopes is shown for comparison. The best resolution occurs at a z_o/r_o ratio of 1.27, agreeing well with prior data for cylindrical ion traps.

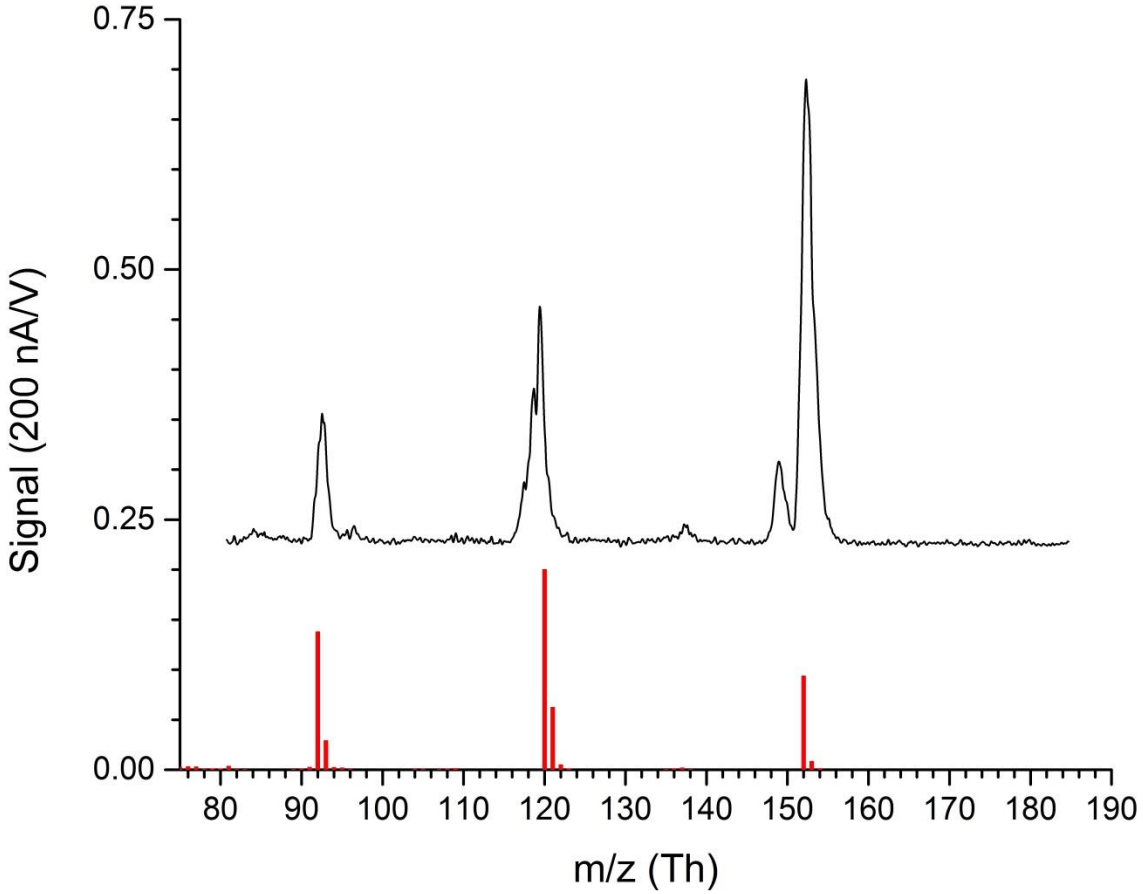

Figure 2.9: An example spectrum of an organic analyte, methyl salicylate, compared to its NIST standard spectrum (in red) taken with the highest performing SLIT from Fig. 2.8. The three main peaks from the NIST spectrum are observed with the SLIT with an additional peak at 149 Th believed to be a contaminant in the MES sample. As the fragment ion pathways are dependent on experimental timescale, it is not surprising that the ion trap data shown here does not follow the same fragment ion intensities since the NIST data is taken on a linear quadrupole which conducts mass spectrometry at a different timescale.

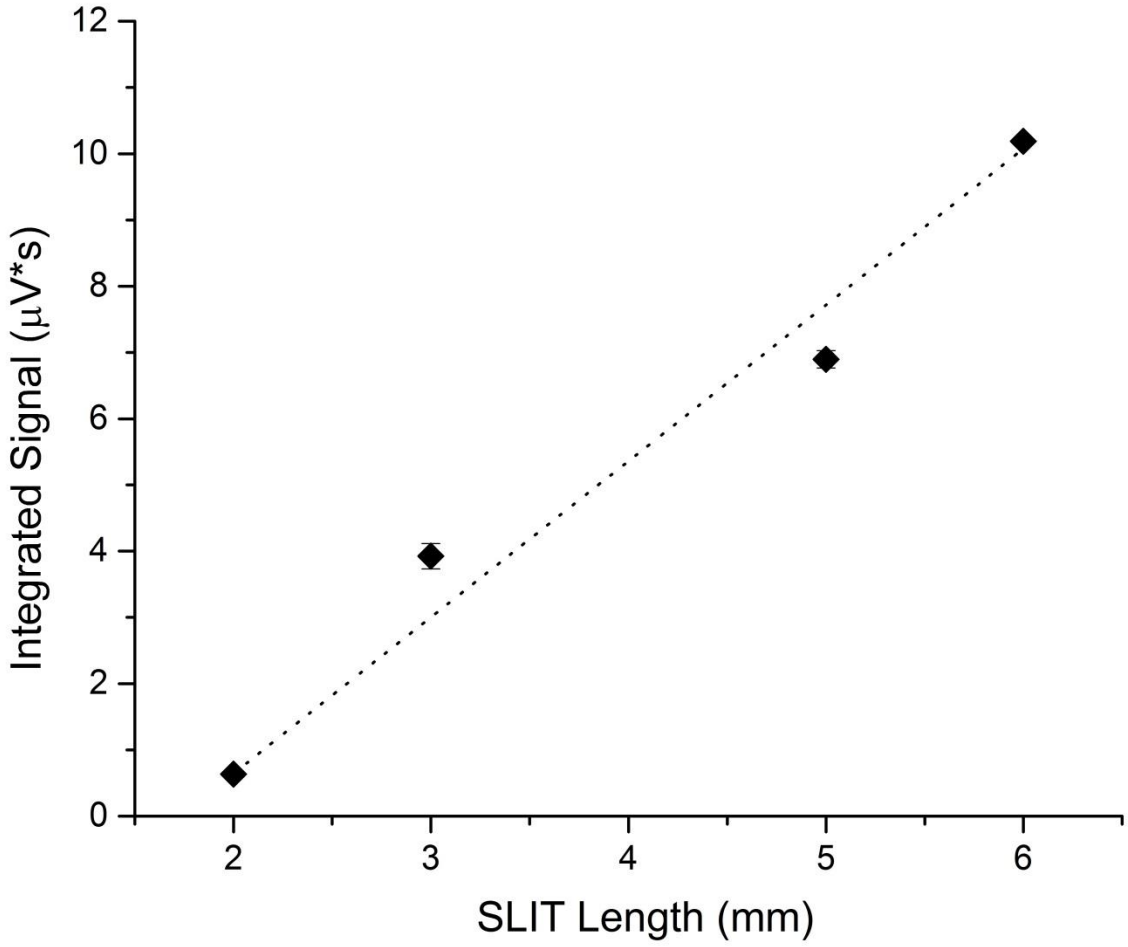

Figure 2.10: Plot of integrated signal intensity for 0.15 mTorr xenon in 10 mTorr helium vs SLIT length ($2y_o$) showing a roughly linear increase ($R^2 = 0.9944$) in the number of trapped ions with increasing length. Error bars are the standard deviation from the replicates of each data point taken sequentially.

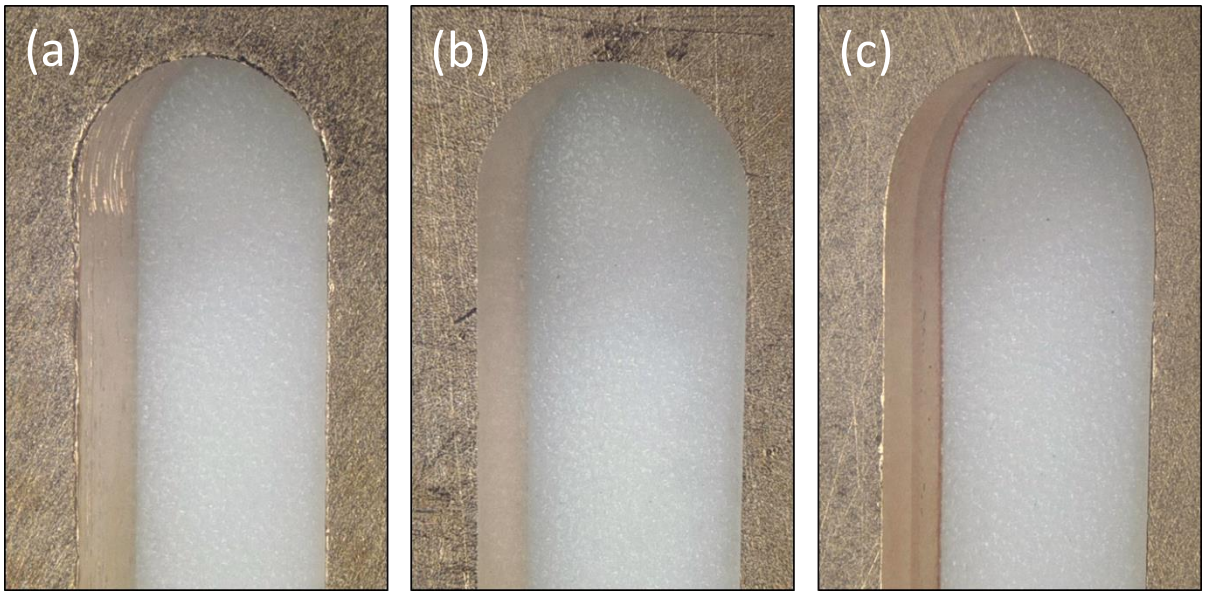

Figure 2.11: Images of SLIT ring electrodes at 100X magnification fabricated via manual machining (a), CNC machining (b), and wet chemical etching (c). The manually machined electrode exhibits visible roughness on the inside surface, a widening of the end portion due to jitter in the milling, and a burred surface protruding from the edge of the machined portion. Both the CNC milled and the etched electrodes have much smoother surfaces with their only apparent difference being the cusp formed as the result of the isotropic etch.

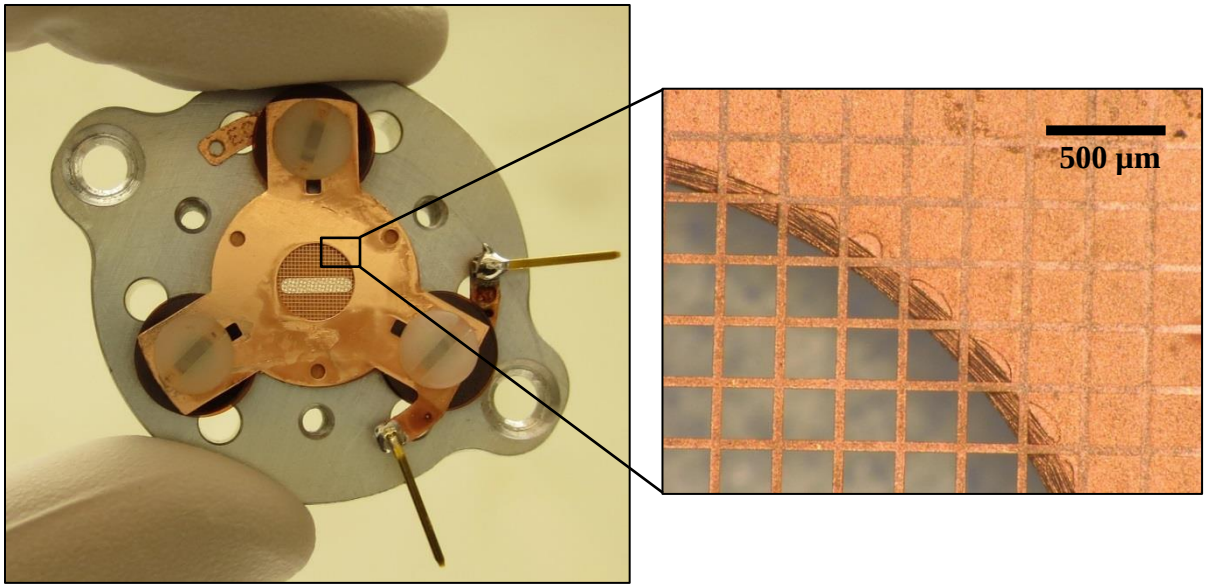

Figure 2.12: Photograph of a constructed second-generation SLIT incorporating the improved CNC milled ring electrode and the flat, electroformed copper mesh shown in the zoomed in portion. These two improvements result in a more uniform field and thus greater resolution and reproducibility.

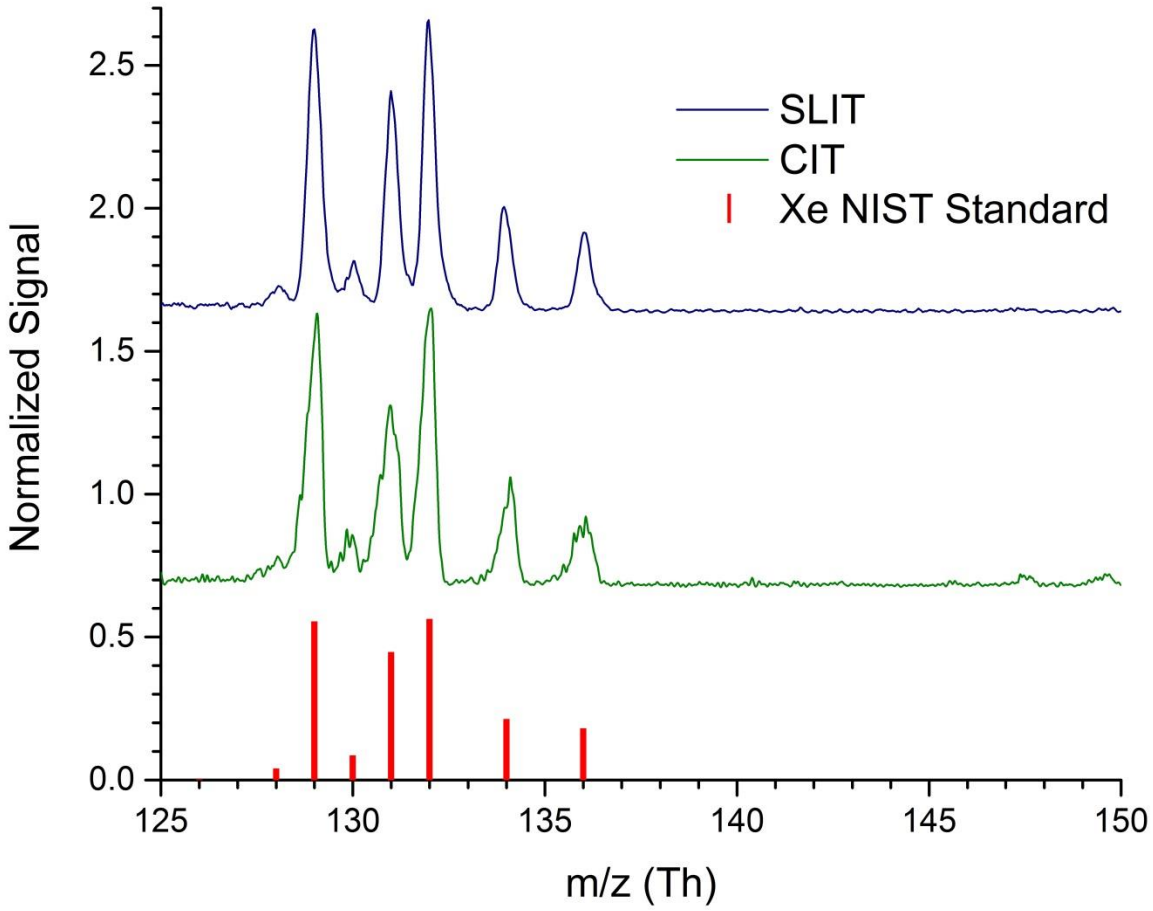

Figure 2.13: Spectra comparing the resolution between a CNC machined SLIT (blue) and CIT (green), both with the same critical dimensions (z_o and x_o/r_o). Xenon was analyzed in 30 mTorr of helium buffer gas under identical conditions save for adjustment of the axial RF signal for maximum resolution. The average peak width of the five major isotope peaks was 0.41 Th and 0.44 Th for the SLIT and CIT, respectively. Additionally, one can see a higher signal to noise ratio for the SLIT, indicating its ability to trap and analyze a greater number of ions than a CIT with the same critical dimensions.

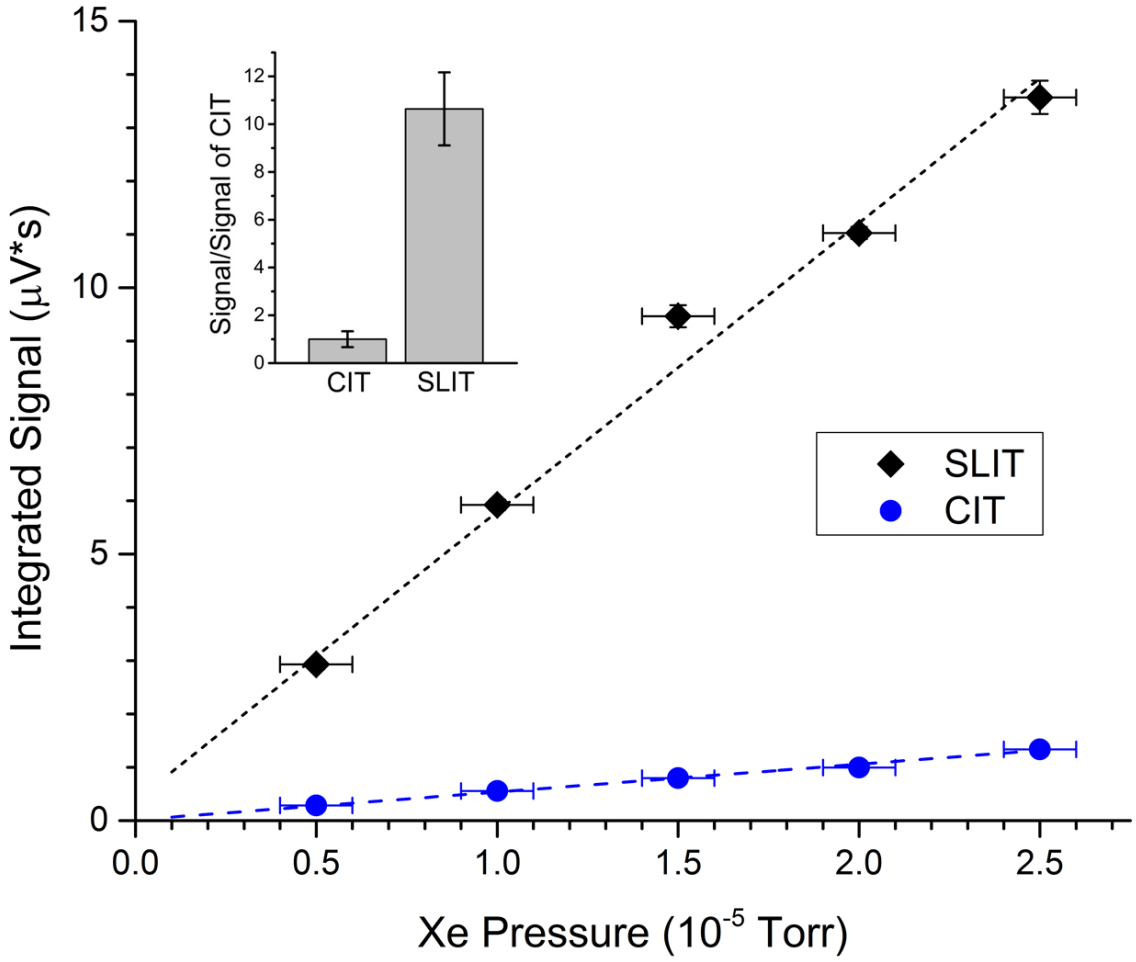

Figure 2.14: Calibration curves comparing the sensitivity of a CNC machined SLIT (black) and CIT (blue), both with the same critical dimensions (z_o and x_o/r_o). Horizontal error bars represent the uncertainty in the measure of the xenon pressure while vertical error bars are the standard deviation of the integrated signal over three replicates taken sequentially. The slopes of a linear fit are 5.4 and 0.52 μV*s for the SLIT and CIT respectively, showing an order of magnitude increase in sensitivity for a 5 mm long SLIT over a CIT with identical critical dimensions. The bar graph is the result of this same experiment being run at a single xenon pressure (0.12 mTorr) for each of three individual traps each of the SLIT and CIT geometries. This shows greater variability but with the same result of a 10.4 ± 3.8 times signal increase for the SLIT.

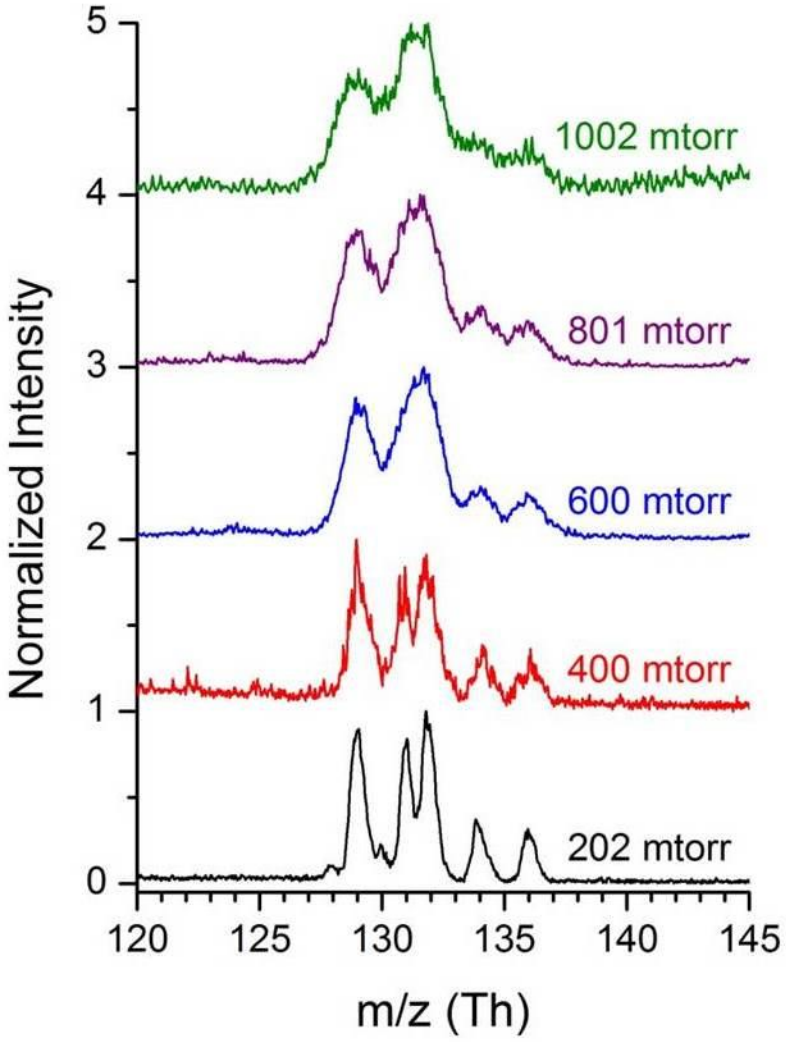

Figure 2.15: Spectra of xenon taken with increasing helium buffer gas pressures. Increasing the helium pressure to 1000 mTorr resulted in peak width increases up to ~1.5 Th FWHM using a 500 µm x_o, 5 mm long SLIT. This deterioration in peak widths corresponds to that observed for a CIT operated under similar conditions.[19] It should be noted that ionization conditions were adjusted at each pressure to maintain adequate signal intensity and thus relative signal to noise levels should not be directly attributed to the variation in buffer gas pressure.

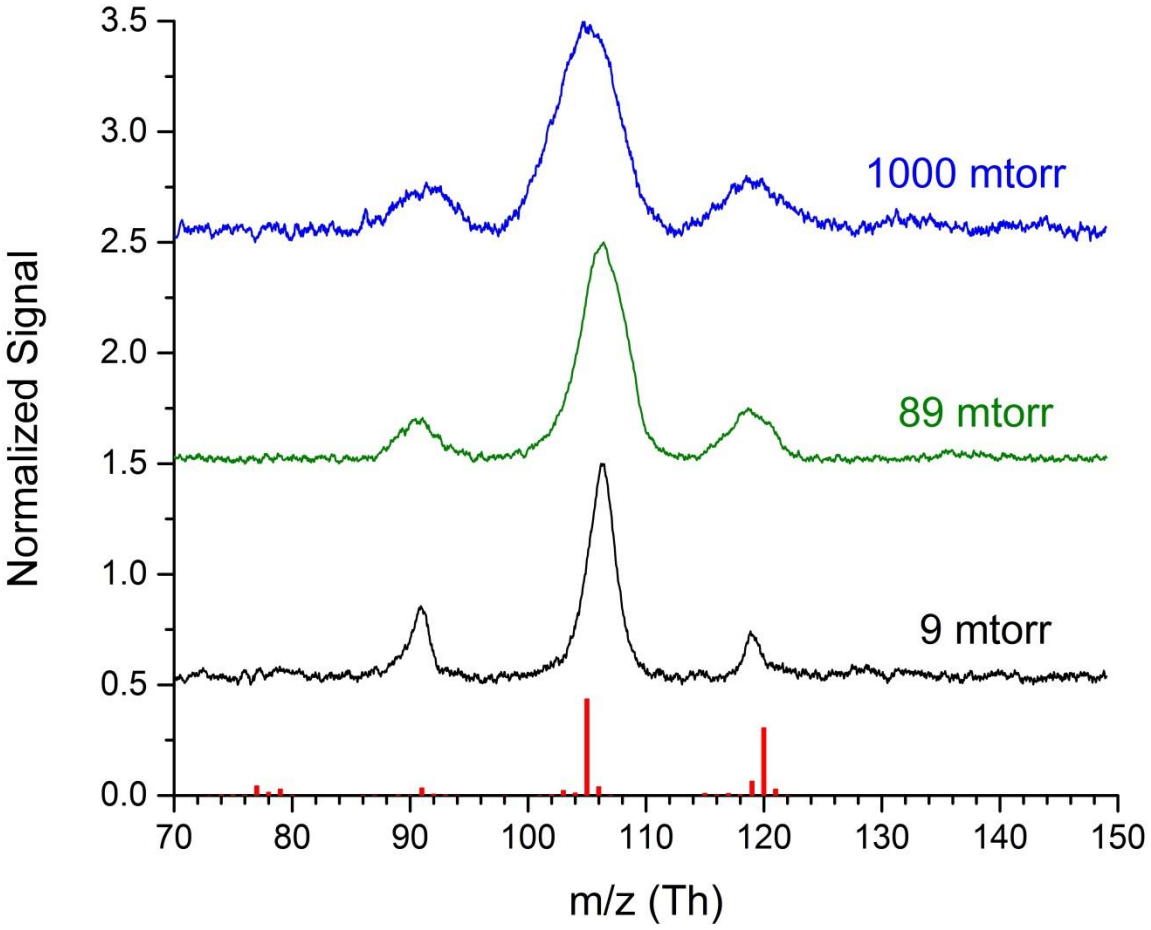

Figure 2.16: Mass spectra of mesitylene (1,3,5-trimethylbenzene) demonstrating SLIT performance at elevated pressures of nitrogen buffer gas. Mesitylene at 0.11 mTorr was detected with a 500 µm x_o, 5 mm long SLIT under 9, 89, and 1000 mTorr nitrogen pressures yielding peak widths of 2.3, 4.6, and 6.2 Th, respectively.

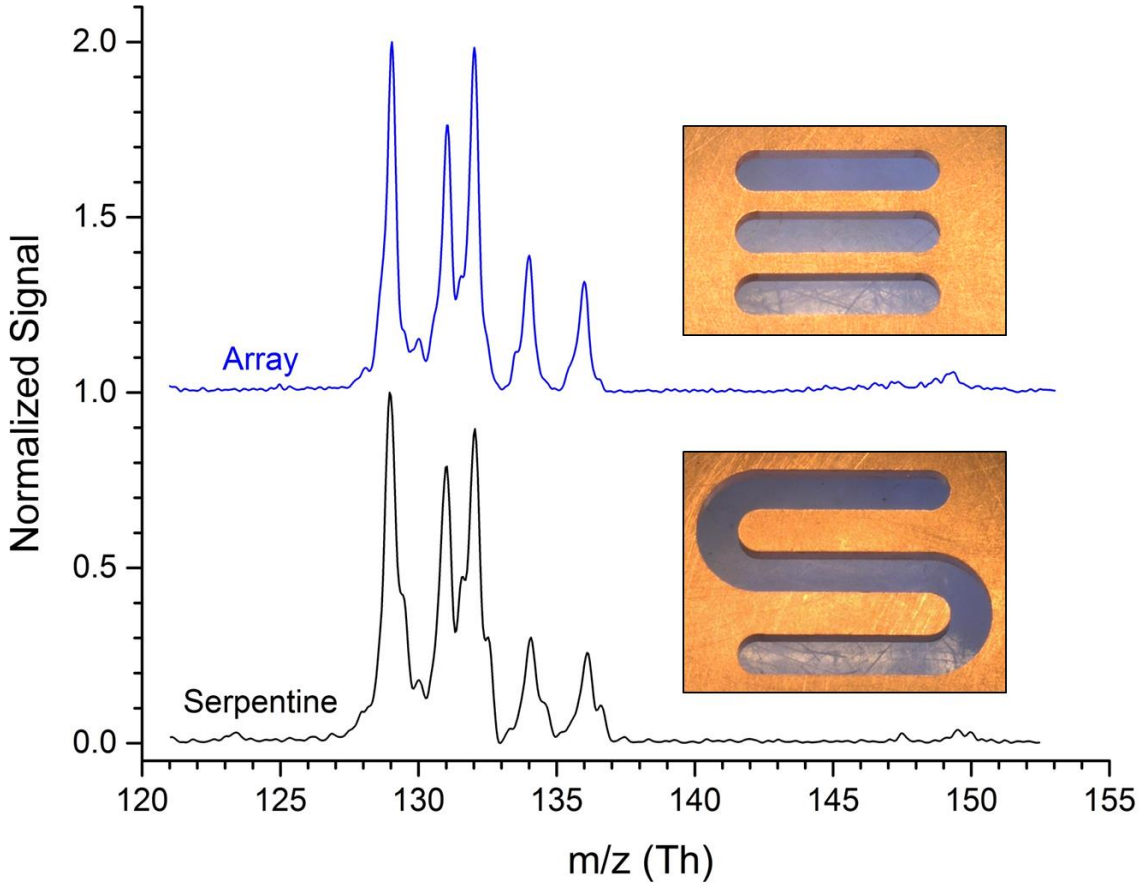

Figure 2.17: Proof of concept spectra for two alternative SLIT geometries pictured, SLIT arrays and serpentine traps. Xenon spectra taken in 30 mTorr helium buffer gas conditions for both geometries showed comparable resolution to that of a single SLIT element trap.

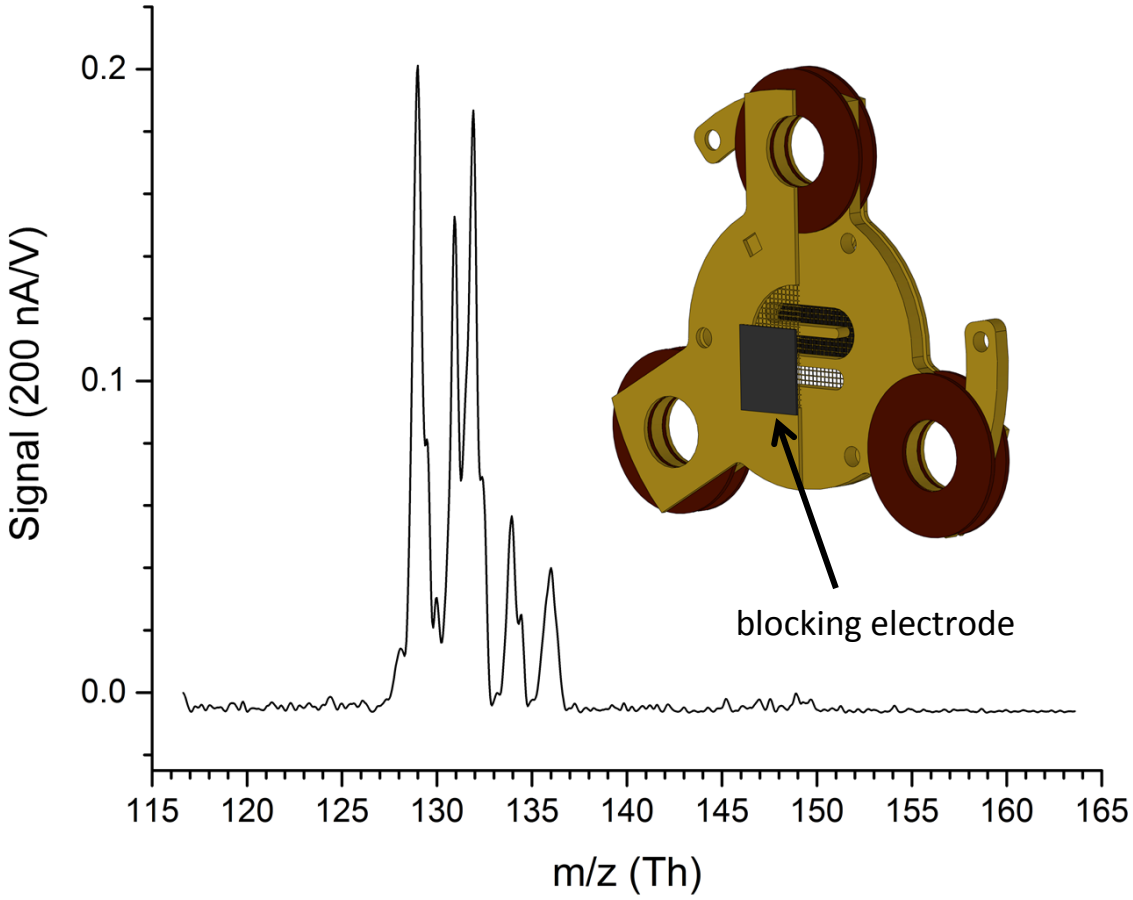

Figure 2.18: Experimental setup and resulting data showing ion travel in a serpentine geometry ion trap. The serpentine trap graphic is shown with the front endcap half cut away to show the positioning of the two black "blocking electrodes." These were placed in such a way that ions detected by ejection from the bottom third of the trapping volume must have been formed in the top third, demonstrating that ions rapidly distribute throughout the trapping volume after formation. A spectrum of xenon in 30 mTorr helium buffer gas taken in this configuration is shown.

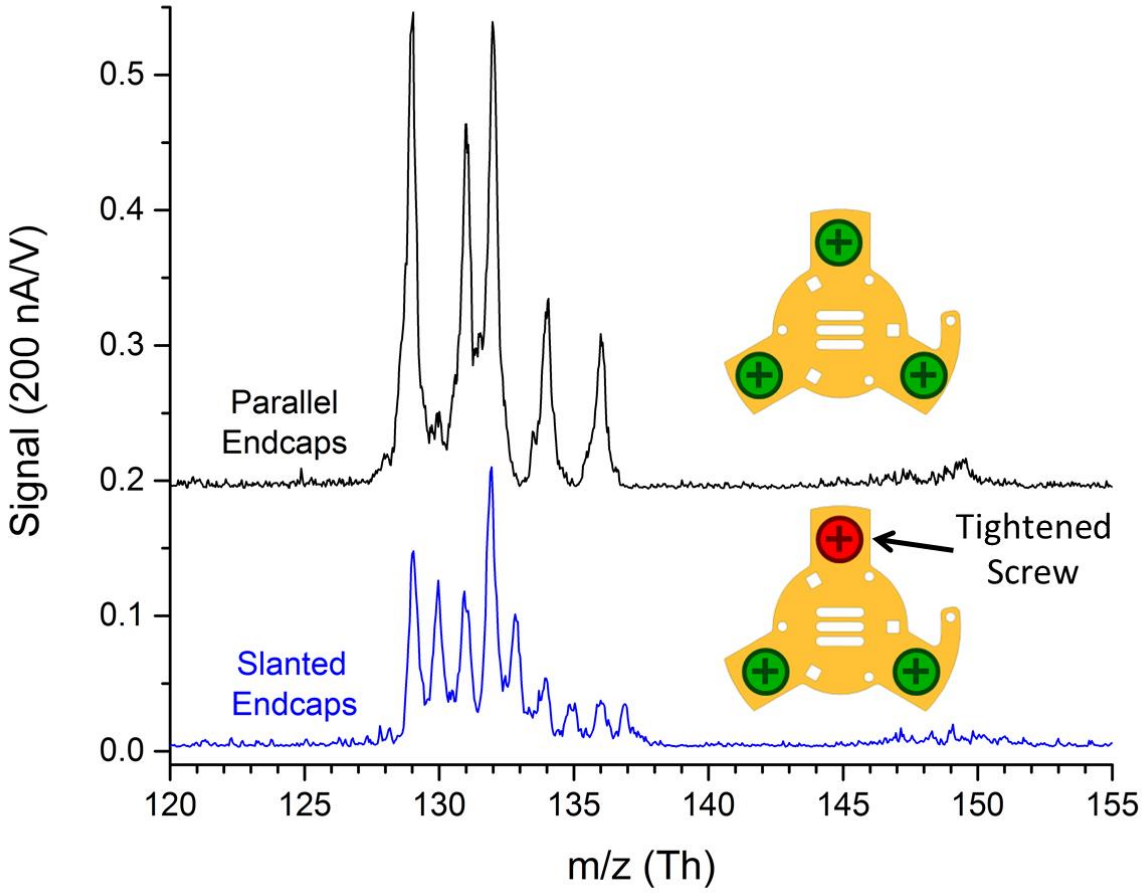

Figure 2.19: Spectra demonstrating ion ejection variation across a three SLIT element array of differing z_o values in 30 mTorr helium. The xenon spectrum in black taken with a trap constructed with all three mounting screws tightened evenly leading to parallel endcap electrodes and good resolution. The blue spectrum is a result of over-tightening one mounting screw and introducing an approximately 5 µm variation in z_o between traps leading to peak splitting. It is believed that spectra from only two of the three trapping elements were observed due to ionizing electron flux differences across the trapping area.

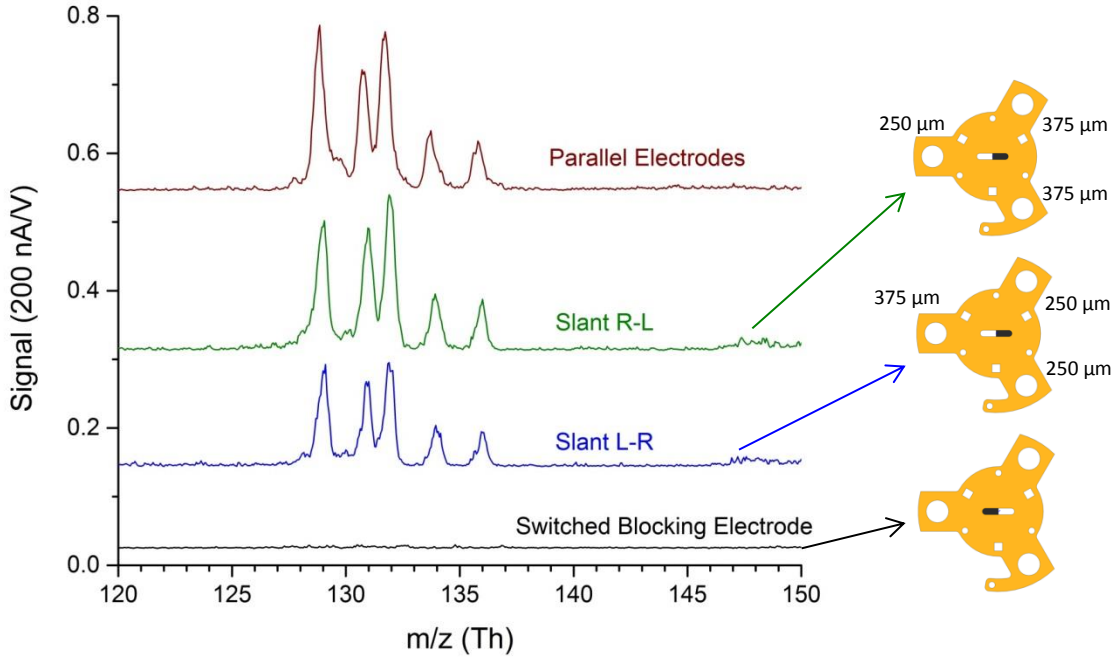

Figure 2.20: A summary of the single SLIT element tolerance study showing xenon spectra generated from both parallel and slanted endcap electrodes. The slant was introduced by changing the interelectrode spacing as indicated by adding additional 125 µm Kapton spacers on either the right side (green trace) or left side (blue trace). The spacing in µm is indicated next to each mounting screw hole. In either case, the trap's resolution was maintained. This was due to the ion population being ejected from only the left side of the trap as shown and was confirmed by way of introducing blocking electrodes shown in black to sample ions ejected from only one half. When ions were blocked from ejecting from the left side (black trace) no ion signal was observed under any conditions.

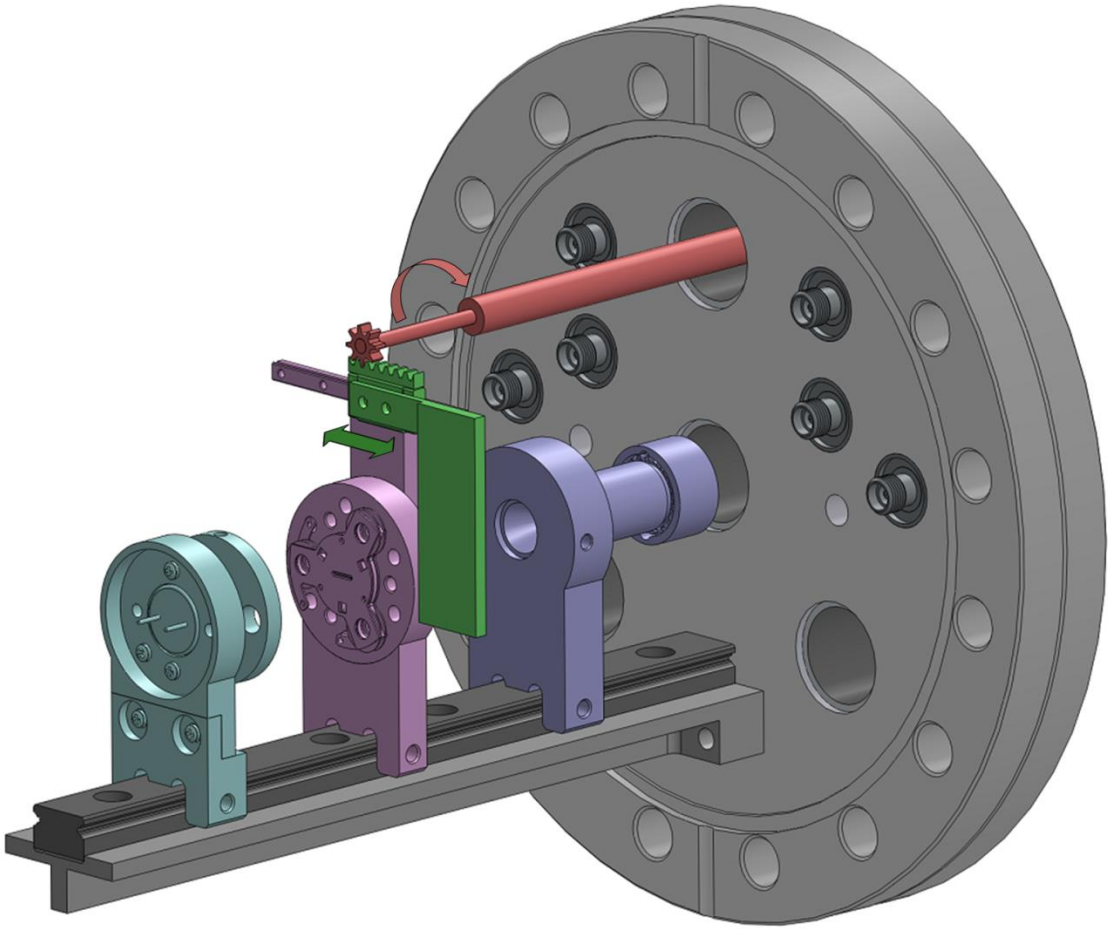

Figure 2.21: A simplified mechanical drawing of the SLIT profiling apparatus for low buffer gas pressures showing the setup's moving parts. The shaft and spur gear in red can be turned via an indicating knob outside the vacuum chamber. This action causes the green cart and attached electrode support to slide back-and-forth along the stationary rail shown in purple. The profiling electrode is attached to the green support and is thus made to slide behind the ion trap electrode stack, exposing the detector to different areas of ion ejection. This low pressure setup uses an electron multiplier (blue) for detection and a thermionic electron emitter (teal) as an ion source.

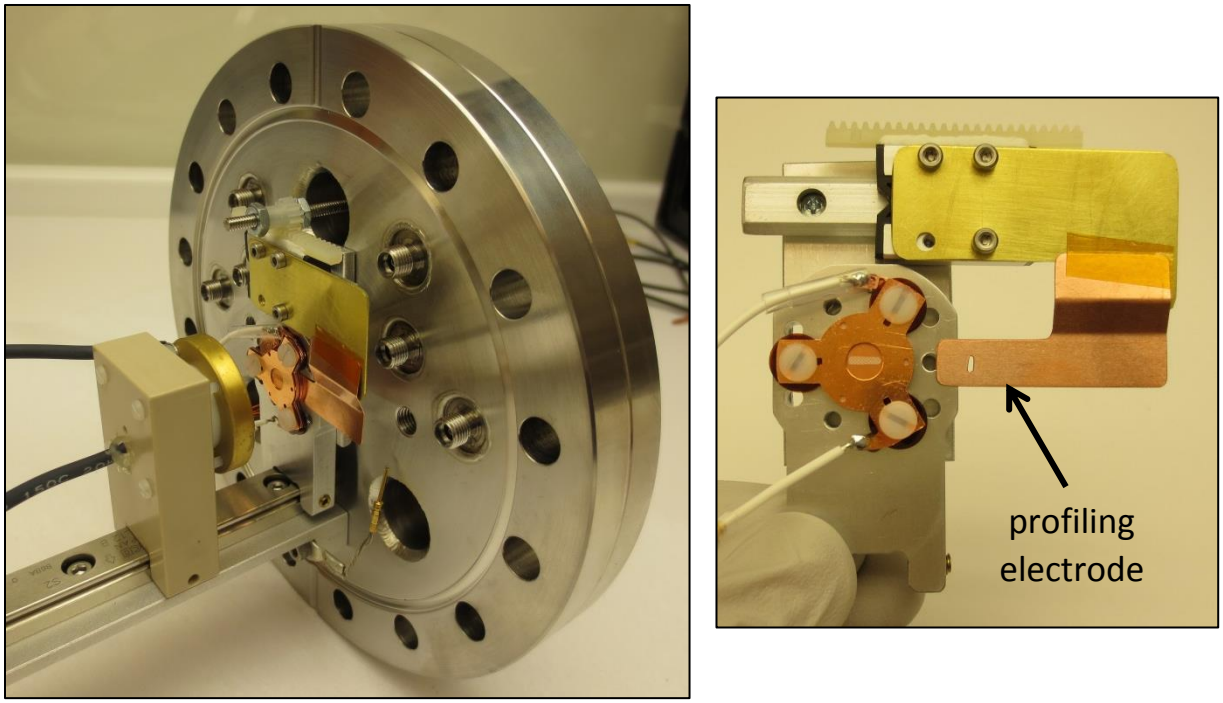

Figure 2.22: Photographs of the SLIT profiling setup. The full setup (left) is identical in operation to that depicted in Figure 2.21 but now uses a glow discharge electron source for ionization and a faraday cup detector for ion detection (not able to be seen behind the trap holder. A close up of the cart and rail linear motion system (right) shows the thin profiling electrode mechanically attached to the cart. Motion of the cart allows the 1 mm slot cut into the profiling electrode to be slid back and forth behind the SLIT electrode stack. In this way, ion ejection from each section of the SLIT can be observed without the need to break vacuum.

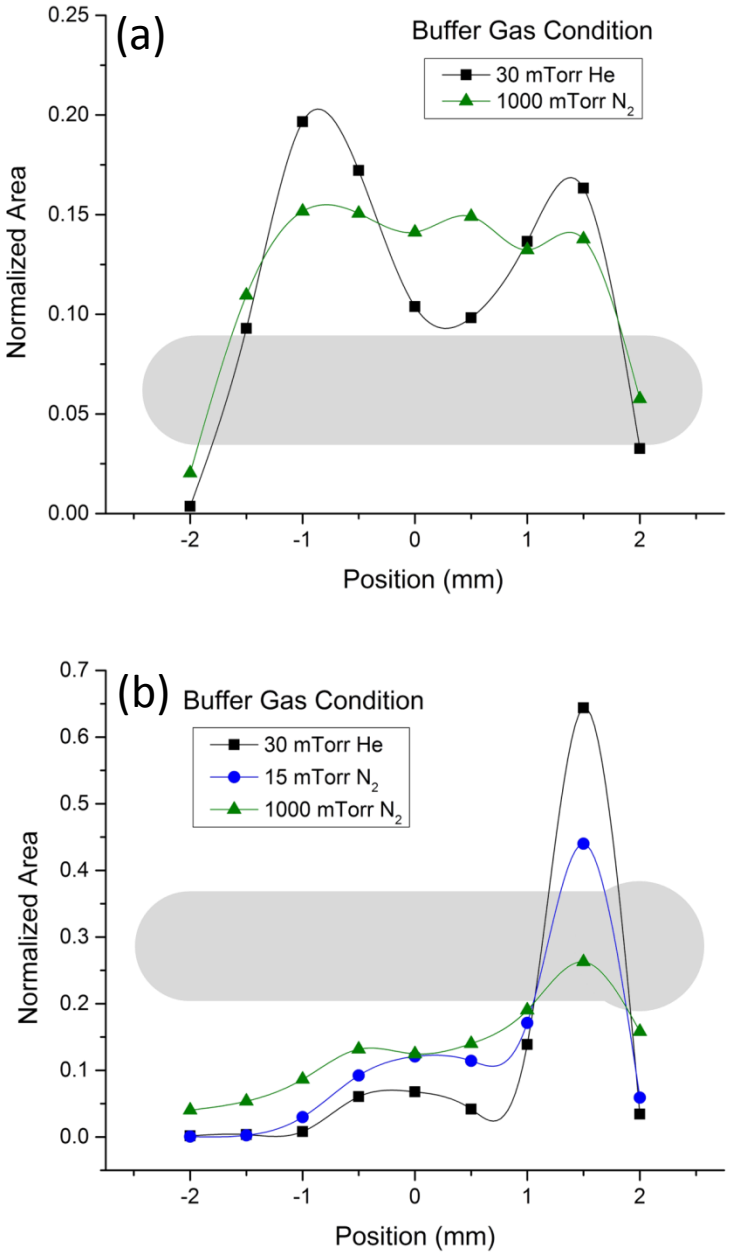

Figure 2.23: An example of xenon ion ejection profiles (with connecting curves to guide the eye) from (a) a conventional SLIT geometry and (b) one in which the geometry has been modified to induce the majority of ion ejection from one section with the shape of the ring electrodes shown in gray. In the conventional SLIT, a modest amount of localized ejection was seen at low pressure helium and was believed to be due to minor ring electrode imperfections. However, in both the conventional and modified SLITs, the localized ejection was greatly suppressed when the buffer gas was changed to high pressure nitrogen. This is due to the increased scattering effect due to nitrogen's higher mass relative to helium.

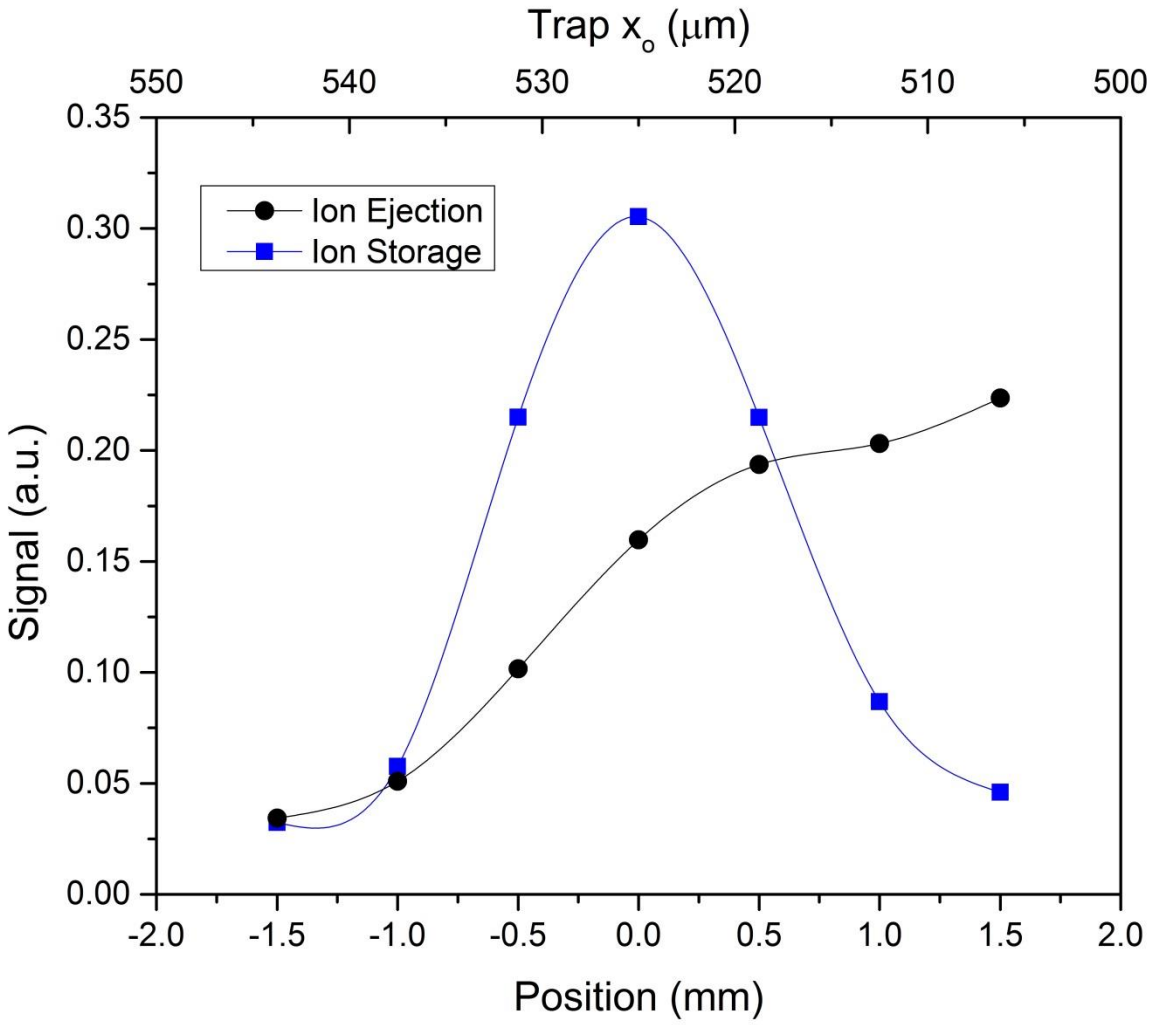

Figure 2.24: Ion ejection and ion storage profiles (with connecting curves to guide the eye) obtained from a tapered SLIT in which the x_o was varied from 550 μm (-2 mm side of graph) to 500 μm (+2 mm side). The ion ejection profile (black) was taken of xenon mass analyzed in the normal manner of a linear RF ramp and demonstrated a preference for ejection from the narrow end where an ion's q_z first reaches 0.908. By contrast, the ion storage profile (blue) was obtained by means of a rapid DC pulse, ejecting ions from wherever they happened to be stored at that moment. The combination of the two profiles suggests that ions are stored symmetrically and rapidly traverse nearly the entire trapping volume. Then they are simply ejected whenever their q_z reaches 0.908, which happens first at the narrow end of the tapered trap studied here.

2.6 References

1. Hager, J. W., A new linear ion trap mass spectrometer. *Rapid Commun. Mass Spectrom.* **2002,** *16* (6), 512-526.

2. Schwartz, J. C.; Senko, M. W.; Syka, J. E. P., A two-dimensional quadrupole ion trap mass spectrometer. *J. Am. Soc. Mass Spectrom.* **2002,** *13* (6), 659-669.

3. Ouyang, Z.; Wu, G.; Song, Y.; Li, H.; Plass, W. R.; Cooks, R. G., Rectilinear Ion Trap: Concepts, Calculations, and Analytical Performance of a New Mass Analyzer. *Analytical Chemistry* **2004,** *76* (16), 4595-4605.

4. Gao, L.; Cooks, R. G.; Ouyang, Z., Breaking the Pumping Speed Barrier in Mass Spectrometry: Discontinuous Atmospheric Pressure Interface. *Analytical Chemistry* **2008,** *80* (11), 4026-4032.

5. Gao, L.; Song, Q.; Patterson, G. E.; Cooks, R. G.; Ouyang, Z., Handheld Rectilinear Ion Trap Mass Spectrometer. *Anal. Chem.* **2006,** *78* (17), 5994-6002.

6. Gao, L.; Sugiarto, A.; Harper, J. D.; Cooks, R. G.; Ouyang, Z., Design and Characterization of a Multisource Hand-Held Tandem Mass Spectrometer. *Anal. Chem.* **2008,** *80* (19), 7198-7205.

7. Kornienko, O.; Reilly, P. T. A.; Whitten, W. B.; Ramsey, J. M., Micro ion trap mass spectrometry. *Rapid Communications in Mass Spectrometry* **1999,** *13* (1), 50-53.

8. Hendricks, P.; Duncan, J.; Noll, R. J.; Ouyang, Z.; Cooks, R. G., Performance of a low voltage ion trap. *International Journal of Mass Spectrometry* **2011,** *305* (1), 69-73.

9. Fico, M.; Yu, M.; Ouyang, Z.; Cooks, R. G.; Chappell, W. J., Miniaturization and Geometry Optimization of a Polymer-Based Rectilinear Ion Trap. *Anal. Chem.* **2007,** *79* (21), 8076-8082.

10. Fico, M.; Maas, J. D.; Smith, S. A.; Costa, A. B.; Ouyang, Z.; Chappell, W. J.; Cooks, R. G., Circular arrays of polymer-based miniature rectilinear ion traps. *Analyst* **2009,** *134* (7), 1338-1347.

11. Maas, J. D.; Hendricks, P. I.; Ouyang, Z.; Cooks, R. G.; Chappell, W. J., Miniature Monolithic Rectilinear Ion Trap Arrays by Stereolithography on Printed Circuit Board. *J. Microelectromech. Syst.* **2010,** *19* (4), 951-960.

12. Li, X. X.; Jiang, G. Y.; Luo, C.; Xu, F. X.; Wang, Y. Y.; Ding, L.; Ding, C. F., Ion Trap Array Mass Analyzer: Structure and Performance. *Anal. Chem.* **2009,** *81* (12), 4840-4846.

13. Peng, Y.; Austin, D. E., New approaches to miniaturizing ion trap mass analyzers. *TrAC Trends in Analytical Chemistry* **2011,** *30* (10), 1560-1567.

14. Song, Y. S.; Wu, G. X.; Song, Q. Y.; Cooks, R. G.; Ouyang, Z.; Plass, W. R., Novel linear ion trap mass analyzer composed of four planar electrodes. *J. Am. Soc. Mass Spectrom.* **2006,** *17* (4), 631-639.

15. Lammert, S. A.; Rockwood, A. A.; Wang, M.; Lee, M. L.; Lee, E. D.; Tolley, S. E.; Oliphant, J. R.; Jones, J. L.; Waite, R. W., Miniature Toroidal Radio Frequency Ion Trap Mass Analyzer. *Journal of the American Society for Mass Spectrometry* **2006,** *17* (7), 916-922.

16. Taylor, N.; Austin, D. E., A simplified toroidal ion trap mass analyzer. *Int. J. Mass Spectrom.* **2012,** *321*, 25-32.

17. Wells, J. M.; Badman, E. R.; Cooks, R. G., A Quadrupole Ion Trap with Cylindrical Geometry Operated in the Mass-Selective Instability Mode. *Analytical Chemistry* **1998,** *70* (3), 438-444.

18. Moxom, J.; Reilly, P. T. A.; Whitten, W. B.; Ramsey, J. M., Double resonance ejection in a micro ion trap mass spectrometer. *Rapid Communications in Mass Spectrometry* **2002,** *16* (8), 755-760.

19. Wolfe, D. W. High-Pressure Cylindrical Ion Trap Mass Spectrometry. UNC at Chapel Hill, North Carolina, 2012.

20. Blakeman, K.; Wolfe, D. W.; Cavanaugh, C. A.; Ramsey, J. M., Mass Spectrometry at Pressures Exceeding 1 Torr in a Microscale Cylindrical Ion Trap. **2014,** *In Preparation*.

CHAPTER 3: FARADAY CUP SYSTEMS FOR ION DETECTION AT HIGH PRESSURES

Introduction

With the exception of Fourier transform instruments that detect ion image currents, all modern mass spectrometers use some form of electron multiplier (EM) detection. In general, these detectors consist of a resistive glass tube across which a large voltage is applied to create a constant accelerating field for electrons. To be detected, an ion must hit the tube's surface (or the surface of a separate dynode) with enough velocity to cause the emission of secondary electrons from the specially coated surface. These electrons are then accelerated down the tube gaining enough velocity to eject further electrons upon each impact, thereby creating an electron avalanche whose current is collected and amplified. The EM detector's high gain of greater than 10^6 enables single ion detection with detector noise as low as 1 count per second and pulse widths as narrow as 1 ns for some geometries.[1] Large gain combined with a dynamic range of 6-8 orders of magnitude makes the EM an ideal detector for nearly all mass spectrometers. However, at pressures much above 10^{-3} Torr, EMs start to experience ion feedback, where the secondary electrons ionize background gasses which go on to form further secondary electrons. This cyclic feedback creates large continuous currents causing the detector to fail prematurely. Laboratory based mass spectrometers are not susceptible to feedback failure modes due to their low operating pressures, but as discussed in the two prior chapters, it is desirable to operate portable mass

spectrometers at pressures up to 1 Torr. This high pressure operation necessitates the development of pressure tolerant ion detectors.

With the absence of any high voltages, a Faraday cup (FC) detector is an example of an ion detector able to operate under any pressure conditions. It consists of a simple metal electrode upon which ions strike and lose their charge, yielding a signal that can be subsequently amplified. Faraday cup detectors suffer in comparison to electron multipliers in almost every figure of merit but they still fit some niche applications in modern mass spectrometry. In isotope ratio mass spectrometry in which RSDs of 0.001% are typically necessary, several Faraday cups can be used in parallel to simultaneously monitor several isotopes of interest in a sector mass analyzer.[2] Electron multipliers are too unstable for this work due to deterioration of their emissive surface over time. Another shortcoming of EMs is their inability to detect very large m/z ratios due to the ion's low impact speeds failing to emit secondary electrons. Since Faraday cups are a direct measure of charge, no such mass biases exist and FCs have been utilized in TOF instruments to detect ions as high as 300,000 Th.[3] Most recently, and most relevant to the work presented here, Faraday cups have started to see use in miniaturized instruments using FC arrays in ion dispersive mass analyzers[4-5] and single element FCs in ion mobility instruments operating at or near atmospheric pressure.[6-7]

3.1 Feasibility of Faraday Cups as Ion Trap Detectors

Very sensitive current amplifiers such as picoammeters rely on large value feedback resistors for their sensitivity, making them slow on the timescale of an ion trap experiment (e.g. with mass ramp of several ms). Thus, the major challenge of utilizing Faraday cups as

ion trap detectors is in the development of charge sensitive amplifiers that have adequate sensitivity while maintaining enough bandwidth to avoid peak distortion. For the miniaturized ion traps of interest, the required bandwidth falls in the 5 – 30 kHz range depending on the MS peak widths (lower bandwidths for the wide peak widths at high pressure and higher bandwidths for the narrow peak widths at low pressure). As will be demonstrated in this chapter, the amplifiers require sufficient sensitivity to detect MS peaks made up of 10s to 100s of charges. Furthermore, the RF voltage and DC pulses necessary for ion trap operation create an electrically noisy environment in which to place the Faraday cup detector. This noise is combatted by shielding of the Faraday cup and amplifier components and by spectral averaging, the latter of which creates a tradeoff between sensitivity and measurement time that will be further discussed in detail in Chapter 5.

Custom CTIA Faraday Cup Amplifier

The stretched length ion trap (SLIT) from Chapter 2 aids in the implementation of a Faraday cup detector for microscale ion traps because the increase in the amount of trapped ions afforded by the SLIT lowers the sensitivity requirements of the FC amplifier. To demonstrate this property, spectra from a single element SLIT and a 19 element CIT array were compared using the same Faraday cup detector. The CIT array data was taken from earlier work done in our laboratory[8] with a single channel Faraday cup amplifier system developed by collaborators at The University of Arizona, based on their previous work with Faraday cup arrays.[9] This initial Faraday cup characterization in low pressure helium buffer gas was conducted in the same isobaric cube vacuum chamber as the SLIT profiling experiments described in Section 2.3. A simplified depiction of the experimental apparatus can be found in Figure 3.1, with the most notable feature being the added box surrounding

the Faraday cup for electromagnetic shielding. This box was held at ground potential to shield the FC from noise stemming from the RF trapping potential and other electronic noise sources while the mesh grid in between the ion trap and FC could be biased in order to guide ions through the mesh to the detector. This mesh grid was also connected to the shielding box by a bypass capacitor to provide a low impedance path to ground for any RF noise. Experiments were completed with Faraday cup systems in which the FC and amplifier were both housed in the shielding box and with systems in which the amplifier was operated outside the vacuum chamber with only the Faraday cup electrode inside the box.

The Faraday cup system used in the SLIT/CIT array comparison was a second generation capacitive transimpedance amplifier (CTIA), built on the same PCB board that housed the Faraday cup input electrode. Both FC and amplifier were operated inside the shielding box in this case. A simplified schematic and photograph of the CTIA can be found in Figure 3.2. The CTIA consists of a differential input to reduce common mode noise. A 10 fF capacitor integrates the charge impinging on the FC during the ion trap mass ramp and can be cleared for the next ramp by shorting this capacitor in between spectra. The output is also differential in nature so any noise picked up post amplification can be eliminated by subtracting the two signal outputs from one another. The FC and amplifier circuitry were biased to attract the ions ejected from the trap, and the bias circuitry and the means of decoupling the signal from this bias is described thoroughly elsewhere.[8] Since the output is an integrated spectrum, post processing was applied, first differentiating to obtain a traditional mass spectrum and then low pass filtering at 40 kHz to remove high frequency noise.

The SLIT (5 mm long, x_o = 500 µm) and the CIT array (19 elements, r_o = 500 µm) were both operated under similar conditions in 30 mTorr helium buffer gas except for the xenon sample pressure which was 2.6×10^{-5} Torr and 5.9×10^{-5} Torr, respectively. The shielding grid, the FC, and the amplifier were all biased to -100 V to attract the positive ions ejected from the trap. A relatively long ionization period of 15 ms at 1.7 A of emitter current was used in order to achieve the signal to noise ratios shown in Figure 3.3. As can be seen, when accounting for the sample pressure difference, the SLIT has similar signal to noise ratios (55 vs. 25) as the 19 element CIT array. This is promising for FC detector development as the SLIT achieves similar signal to noise values while occupying $1/5^{th}$ the footprint of the CIT array. Additionally, the resolution is improved for the SLIT which is attributed to dimensional variations among the 19 CIT elements leading to peak broadening. Because of the higher signal levels afforded by the SLIT, this geometry was chosen for the majority of the work presented in this chapter.

Commercial FC Amplifier Testing

The CTIA detector contained a custom fabricated IC, contributing to the CTIA's high cost and long lead times. For these reasons, the performance of a commercially available charge sensitive amplifier was also explored. A suitable candidate was found in Amptek's A250CF CoolFET amplifier. Compared to the CTIA, the A250CF operates in a slightly different manner than the CTIA and will be described breifly due to the differences the operation causes in how the spectra are collected and analyzed.

A simplified electrical diagram of the A250CF is shown in Figure 3.4. Like the CTIA, the input from the Faraday cup charges a small feedback capacitor. The resulting

voltage acts as the gate on a FET which is thermoelectrically cooled to -50°C to reduce electronic noise. Finally, the current from the FET is amplified by the A250 amplifier IC to a voltage suitable for the computer DAQ. Instead of shorting the feedback capacitor in between spectra, the A250CF uses a large drain resistance to let the input charge slowly clear. This slow charge dissipation results in a pseudo-integrated spectrum where detected peaks appear as a pulse with a fast rise time (2.5 ns) and a decay time of 100s of ms. This time disparity has two consequences for its use as an ion trap detector. The first is that the signal after a MS peak in the differentiated spectra will always fall slightly below baseline in proportion to the height of the preceding peak. In most cases it has been a minor effect and its correction was only found necessary for some of the GC data presented in Chapter 5. The second consequence is that the detector is always actively integrating charge, leading to the presence of a massive influx of charge being detected during the ionization portion of the scan function. Due to the detection scheme, the ion cooling portion of the scan function has to be lengthened from the typical 2-3 ms to 6-10 ms to allow the detector time to recover prior to the analytical scan.

To determine if the A250CF could detect ion peaks with sufficient resolution to be a useful MS detector, xenon spectra were taken in the usual manner and compared to xenon spectra gathered with an electron multiplier and the CTIA detector using the same SLIT described in the prior section. In this case the A250CF was operated outside the vacuum chamber with a shielded coaxial cable transferring the signal from the Faraday cup through to the amplifier. Example spectra of 3.5×10^{-5} Torr xenon in 30 mTorr helium from each detector can be seen in Figure 3.5. The two Faraday cup spectra are seen to have nearly the same resolution as the electron multiplier spectrum, with the peak widths of the A250CF

being slightly wider. Because peak widths are narrower than we could expect to see in a handheld MS operated at high pressures, we can be confident moving forward that the two FC detectors studied here have sufficient bandwidth for that purpose.

3.2 High Pressure Faraday Cup Operation

As an essential step towards development of a handheld system, an attempt was next made to collect Faraday cup detector spectra at high buffer gas pressures to ensure that sufficient numbers of ions could still be collected to yield a strong signal. This work was initially attempted using the low pressure apparatus from Section 3.1; however, it was found that signal was greatly diminished with increasing pressure. This decreased signal was attributed to scattering of the ions from buffer gas collisions over the several centimeters of distance the ions must travel between the trap and the FC. To alleviate this issue, a newly developed miniature vacuum chamber was used in order to lower the distance to several millimeters while also eliminating the need for a separate shielding box for the FC, both of which improved signal intensity. This apparatus was used in the remainder of the experiments presented in this chapter. A fully miniaturized system is the subject of Chapter 4 and mechanical drawings specific to the Faraday cup interface can be found there in Figure 4.5.

Performance of a Miniaturized Faraday Cup Amplifier

While the A250CF amplifier proved to be a good commercial option for FC ion detection, there are some significant disadvantages to using this amplifier relating to SWaP. Measuring in at 12 $in.^3$ and 300 g, it would represent a greater percentage of the overall size and weight of a handheld instrument than desired. Of greater concern is that because of the

Peltier cooling elements, its power draw is 5.28 W, which is again a large portion of the total instrument power draw goal (< 20 W). For these reasons, our collaborators at 908 Devices Inc. developed a miniaturized version of the A250CF without any cooling elements. By giving careful consideration to electrical component selection and design of the printed circuit board to reduce noise, a detector was developed with improved SWaP while maintaining similar performance levels. An image comparing the 4th generation of miniature detector amplifier (DA - 4) and the A250CF can be found in Figure 3.6. The volume and weight of the DA - 4 are now 1.5 in.^{3} and 60 g, respectively, while the power draw has been reduced by ~99% to 54 mW.

To characterize the DA - 4 at the target pressure of 1 Torr air, a 7 element CIT array (r_o = 500 µm) that was previously tested in a full-scale differential chamber was installed in the new miniature vacuum chamber. Since the buffer gas was ambient air leaked into the chamber, sample introduction was accomplished by simply holding a vial of analyte near this inlet. A comparison of the performance of the DA - 4 versus the A250CF was performed with mesitylene (1,3,5 – trimethylbenzene) as the analyte and can be found as 1000 scan averages in Figure 3.7 (black and blue traces). As designed, both the resolution and the signal to noise levels are comparable between the two. In addition, since the gain of the A250CF is known from the data sheet to be 0.64 µV/charge, the total charge detected from the 105 Th peak can be estimated at 800 charges, meaning with these spectra, each individual CIT element is trapping between 100 and 200 charges. With the atmospheric inlet it becomes simple to rapidly switch between various analytes and results from several other substituted benzene analogs; toluene, *o*-xylene, and *p*-xylene; are also shown in Figure 3.7. This demonstrates how the MS can use fragmentation patterns to differentiate between

analytes with similar structures. The last point to emphasize is that now that the entire instrument is operated at high pressure, a turbomolecular vacuum pump is no longer needed. To the best of our knowledge, this work done by our laboratory and our collaborators represents the first example of an ion trap mass spectrometer operated solely with a roughing pump (and most likely the first modern mass spectrometer of any kind).

Finally, the DA - 4 was used to directly compare a CIT array and SLIT array with equal footprints. The same experimental apparatus described above was used under identical conditions for both the CIT array (7 element, r_o = 500 μm) and SLIT array (3 Element, $2y_o$ = 3 and 4 mm, x_o = 500 μm). To maintain a constant sample concentration, the inlet drew in gas from a Tedlar bag filled with mesitylene diluted to ~10 ppm in N_2. As seen in Figure 3.8, the spectra resulting from 1000 scan averages from the two traps show a much larger signal with the SLIT array with a correspondingly higher signal to noise ratio as expected. This data represents a direct example of the greater ion storage efficiency of the SLIT versus the CIT at the desired operating pressure of 1 Torr. The peak near 74 Th is attributed to a contaminant from the Tedlar bag because it is not seen when mesitylene is introduced without the bag.

Signal Dependence on FC Distance and Bias

In order to maximize the number of ions collected by the FC, an experiment was devised to determine the optimal distance between the ion trap and FC as well as the optimal bias voltage used to attract the ions. The apparatus consisted of a Faraday cup attached to a vacuum feedthrough linear positioner (VF - 108, Huntington) with a positional precision of 10 μm. Again, a Tedlar bag was used for constant sample introduction with 1 ppm toluene in

this case. Spectra were taken under identical ionization conditions with the Faraday cup at different positions relative to the trap. This series of experiments was then repeated at increasing bias voltages. The results of all these experiments is presented in Figure 3.9 with the total integrated signal plotted versus trap - FC distance at several different bias voltages. To summarize the data shown, detected signal decreases from its peak value as the Faraday cup is moved away from the trap. However, the peak signal level can be maintained as long as the bias voltage is raised in proportion to the FCs distance from the trap. This demonstrates that the trap - FC distance is not a critical parameter when designing a miniature ion trap system.

3.3 Faraday Cup Application: Study of Convective Gas Flow Through Ion Traps

The majority of the work on microscale ion traps in our laboratory has been conducted using the full-size differentially pumped vacuum systems presented in Chapter 2 so that mass analysis could be conducted at high pressure while an electron multiplier detector could be used at low pressures. It is obvious that the pressure differential across the ion trap results in some amount of net convective flow of the buffer gas through the trap, but as long as the detector remained an electron multiplier, there was no way to isolate the variable of trap flow to study its effects on the mass spectra. However, successful operation of the Faraday cup detectors at low and high buffer gas pressures described above creates the possibility of studying mass spectrometry at 1 Torr while varying the flow through the trap from zero net flow up to the maximum throughput possible. In addition, to the best of our knowledge no ion traps have ever been operated with the intentional introduction of gas flow through the electrodes.

In this work, a 7 element CIT array (r_o = 500 µm) was used as the sole gas conductance limit between the ion trapping chamber and the detection chamber. Shown in schematic form in Figure 3.10, a rough pump, turbo pump, gas inlet, and two valves were used to control the pressures in the two chambers. The ion trapping chamber was held at a constant 1 Torr of N_2 by means of a needle valve inlet being fed by a bag of 10 ppm mesitylene diluted in nitrogen. The detection chamber pressure (and thus the flow through the trap) was varied between 1 Torr and 0.04 Torr by adjusting the turbo pump valve between fully closed and fully open, respectively.

Spectra of mesitylene taken with varying pressure differentials are shown in Figure 3.11a with the 105 Th ion's peak height versus pressure differential plotted in Figure 3.11b. This data shows that the signal level increases rapidly as small amounts of gas flow are introduced but levels off to a maximum level when the pressure differential is approximately 2:1. The increase in signal level is attributed to several possible causes. The first possible explanation is that the net flow towards the detector causes the majority of trapped ions to be ejected through the detector endcap side rather than 50% in each direction. Since this would only account for a doubling in signal, there must be additional factors in play. Other possible effects of the flow could be that the flow guides ions more efficiently through the exit endcap once they become unstable or that the flow leads to an increase in flux of electrons/ions into the trap during ionization, leading to a greater number of trapped ions. In any case, this data clearly shows that for maximum sensitivity, one should design the vacuum system to induce some amount of flow through the trap.

Bruno Coupier, a staff scientist in the Ramsey lab, has worked to develop a cylindrical ion trap simulator (CITSIM) program specifically designed to meet the

laboratory's needs of microscale ion traps operated at high pressures. CITSIM takes advantage of a GPU to solve the program's highly parallelizable algorithms leading to much faster calculations than can be done using commercial software. This program was used to simulate the previously described trap flow experiment under the same conditions. The resulting spectra in Figure 3.11c show a similar increase in intensity with increasing trap flow. Because the simulated ions were already generated inside the trap and were 'detected' upon their immediate exit, these simulations suggest that at least a portion of the signal increase observed experimentally is a result of a greater proportion of trapped ions being ejected towards the detector rather than from ion trapping differences or ions being better guided towards the detector post-ejection. It should be noted that the simulations program is still in its infancy, thus these results should be considered with a certain amount of caution. The signal increase depicted in Figure 3.11b also follows the calculated gas throughput (Q) for choked flow, the flow regime into which this configuration's dimensions and pressures fall.[10] Shown in Figure 3.11d, the curve for gas throughput is seen to rise sharply with little flow introduced and levels off at a pressure ratio of 2:1, just like the experimental signal intensity. This is good evidence that the signal increase is due to the gas flow through the trap and not any other causes such as ionization fluctuations. The trap flow experiments were also conducted with helium buffer gas and yielded similar sensitivity increases with flow but to a lesser extent due to the low mass of helium relative to nitrogen.

3.4 Conclusions

By using a SLIT with high ion storage capacity, the Faraday cup becomes a viable detector for a handheld ion trap mass spectrometer. Several Faraday cup amplifier systems were used to collect mass spectra with the SLIT. These included a custom fabricated CTIA

amplifier, a commercial A250CF amplifier, and a miniaturized version of that commercial amplifier. The demonstrated ability to detect ions at pressures from a few mTorr up to 1 Torr allowed for the study of ion trap performance with varying amounts of buffer gas flow through the trap, resulting in larger signal intensities with increasing flow up to the maximum flow possible.

3.5 Figures

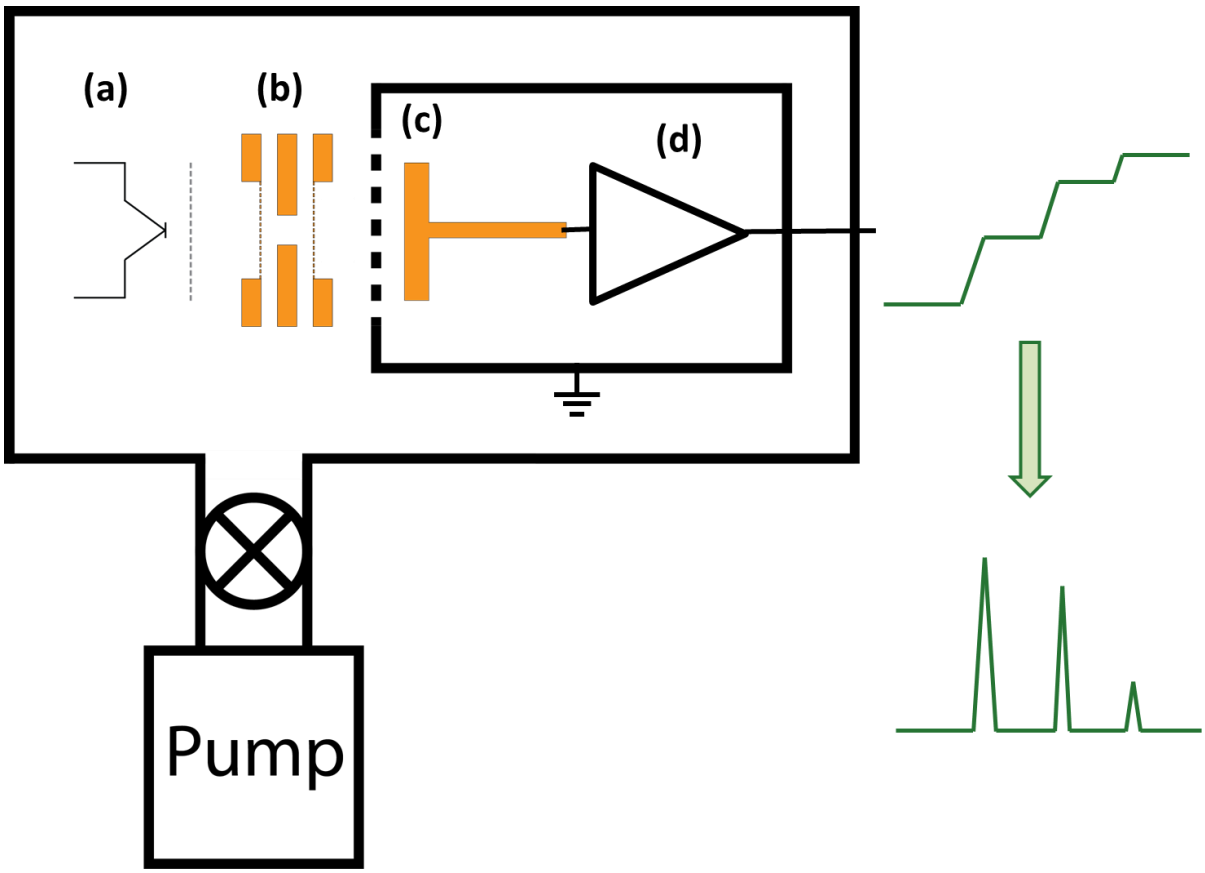

Figure 3.1: Simplified schematic of the isobaric vacuum chamber apparatus used for Faraday cup characterization showing (a) the thermionic electron emitter, (b) the ion trap electrode stack, (c) the Faraday cup, and (d) the charge sensitive amplifier. The Faraday cup and amplifier are housed inside a grounded shielding box to combat noise from the trapping RF voltage, although in some configurations the amplifier is located outside the vacuum chamber completely. Because integrating amplifiers were used in all cases, the resulting signal can be differentiated to produce the desired mass spectrum.

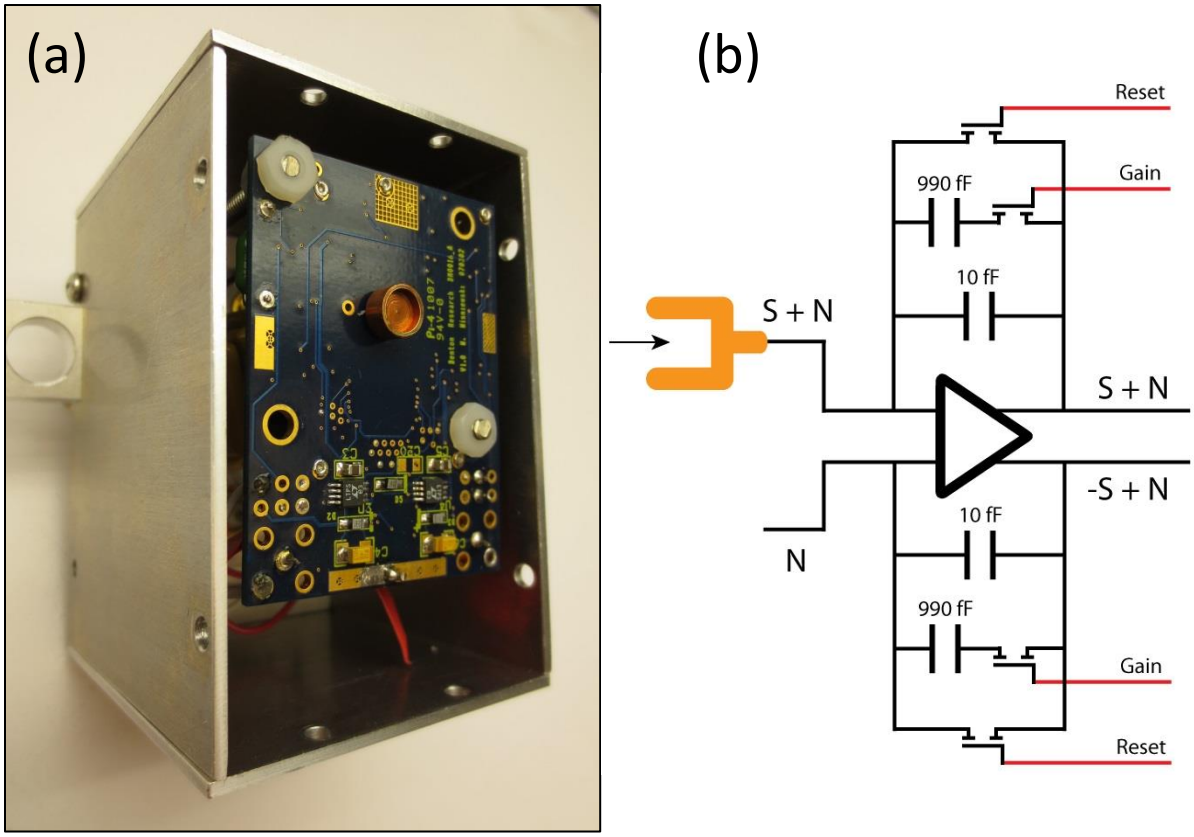

Figure 3.2: A photograph (a) of the custom CTIA detector inside the metal shielding box with the front panel of the box removed to make the full circuit board visible. The copper Faraday cup located in the middle connects through to the back of the PCB where the custom fabricated IC is located. A simplified schematic diagram of the detection circuitry (b) is located to the right. The Faraday cup is attached to one of the two differential inputs and any common mode noise is thus eliminated from the final signal. The two outputs are subtracted from each other prior to data acquisition to subtract any common noise introduced post amplification.

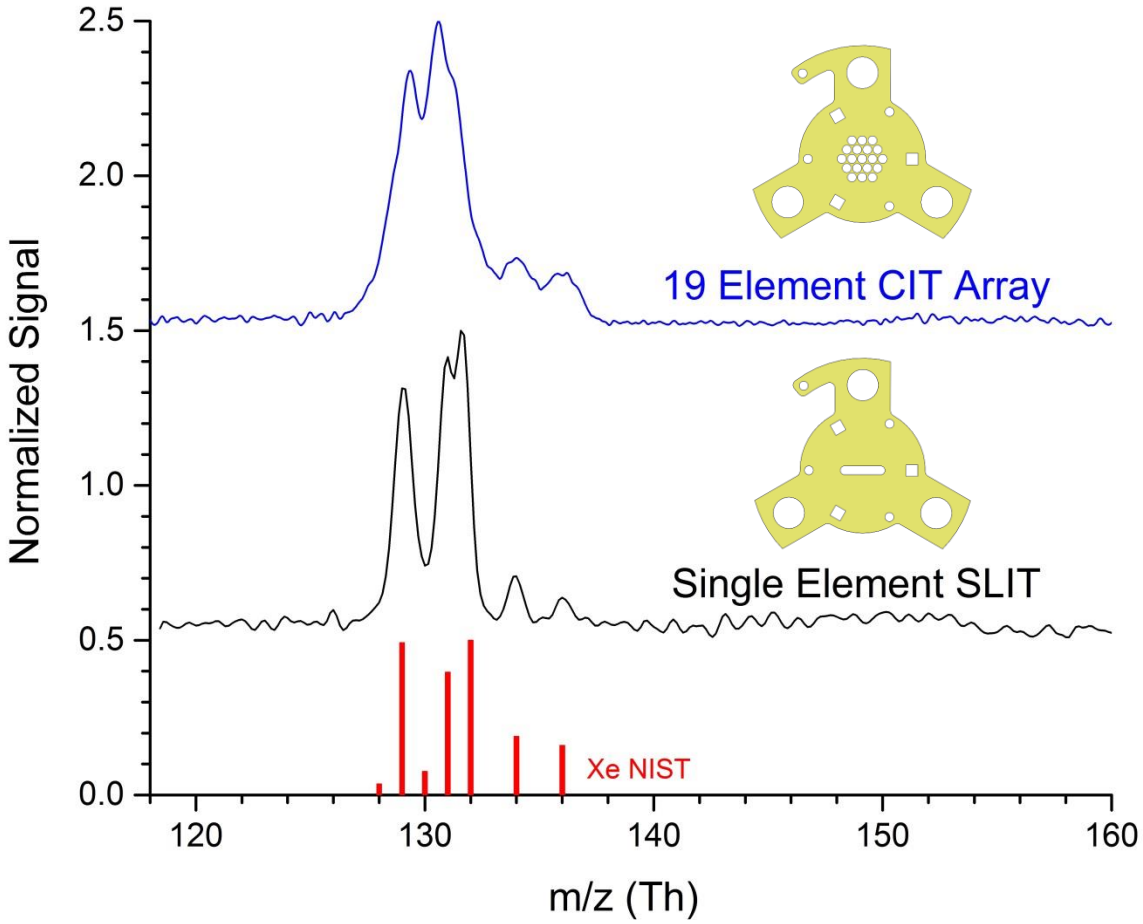

Figure 3.3: Spectra generated from detection of 5.9×10^{-5} Torr xenon detected with a 19 element CIT array (blue) and 2.6×10^{-5} Torr xenon detected with a single element SLIT (black) with drawings of each ring electrode used. The CIT array and SLIT spectra have signal to noise ratios of 55 and 25, respectively, demonstrating that once the difference in sample concentration is accounted for, the SLIT shows similar signal to noise levels as 19 CITs while achieving higher resolution.

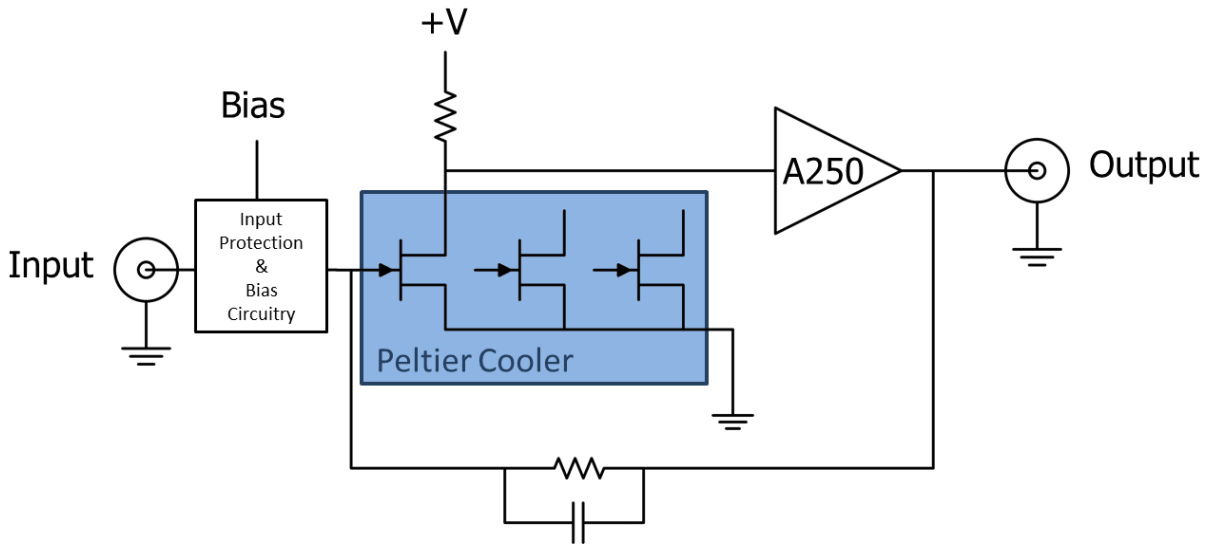

Figure 3.4: A simplified electrical schematic of the A250CF CoolFET charge sensitive preamplifier. This amplifier has three different FETs, two of which act as backups in case of damage. All three are cooled to -50°C in order to lower the amount of electrical noise. This circuit layout results in a pseudo-integrating detector in which an input of charge yields an output pulse with a fast, nanosecond scale rise time and a slow, millisecond scale decay time.

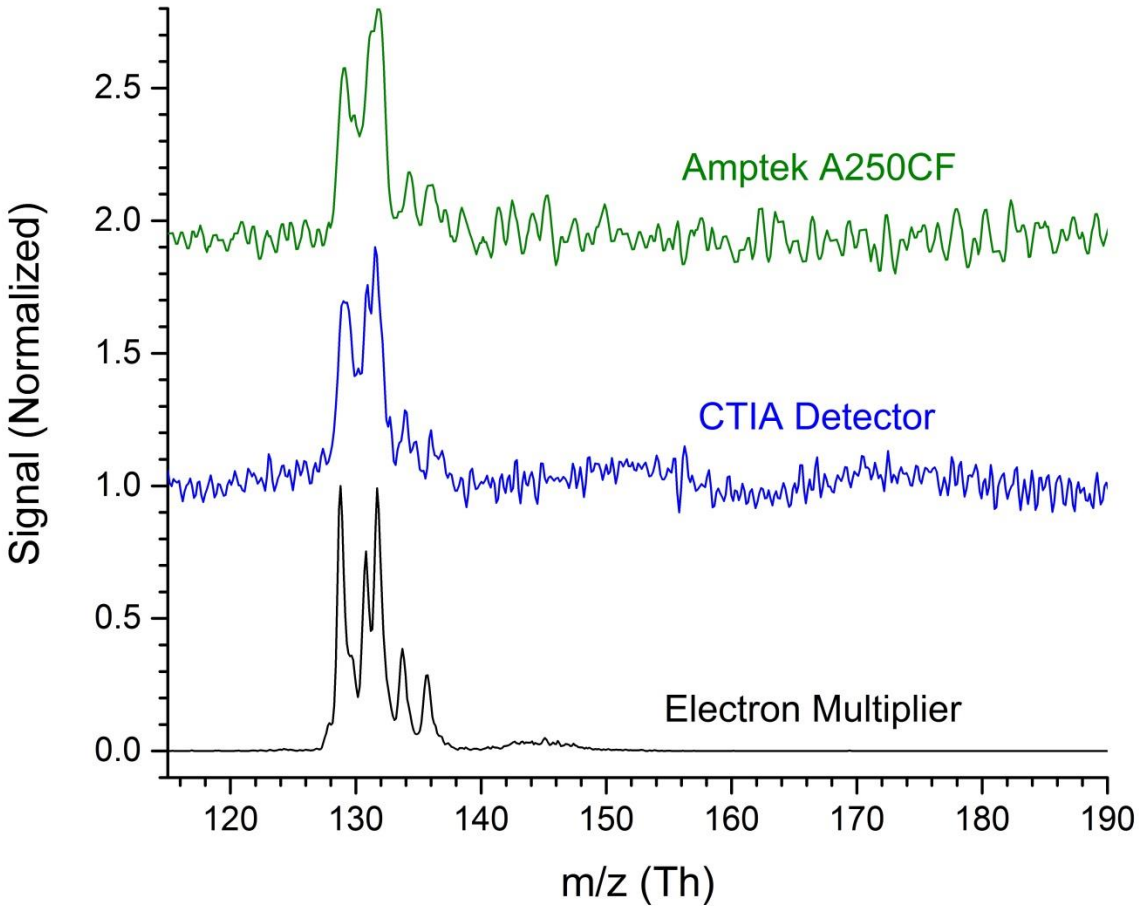

Figure 3.5: Direct comparison of xenon spectra taken in 30 mTorr helium with three different detectors: the commercial A250CF Faraday cup amplifier (green), the custom CTIA Faraday cup amplifier (blue), and a standard electron multiplier (black). From this comparison, one can see that the two Faraday cup amplifiers show poorer resolution than the electron multiplier but still resolve enough of the isotope peaks to yield identifiable xenon spectra. The low frequency noise in the CTIA spectrum is mechanical noise from the turbo pump demonstrating how the sensitive electronics used for Faraday cup amplification are sensitive to even slight mechanical noise.

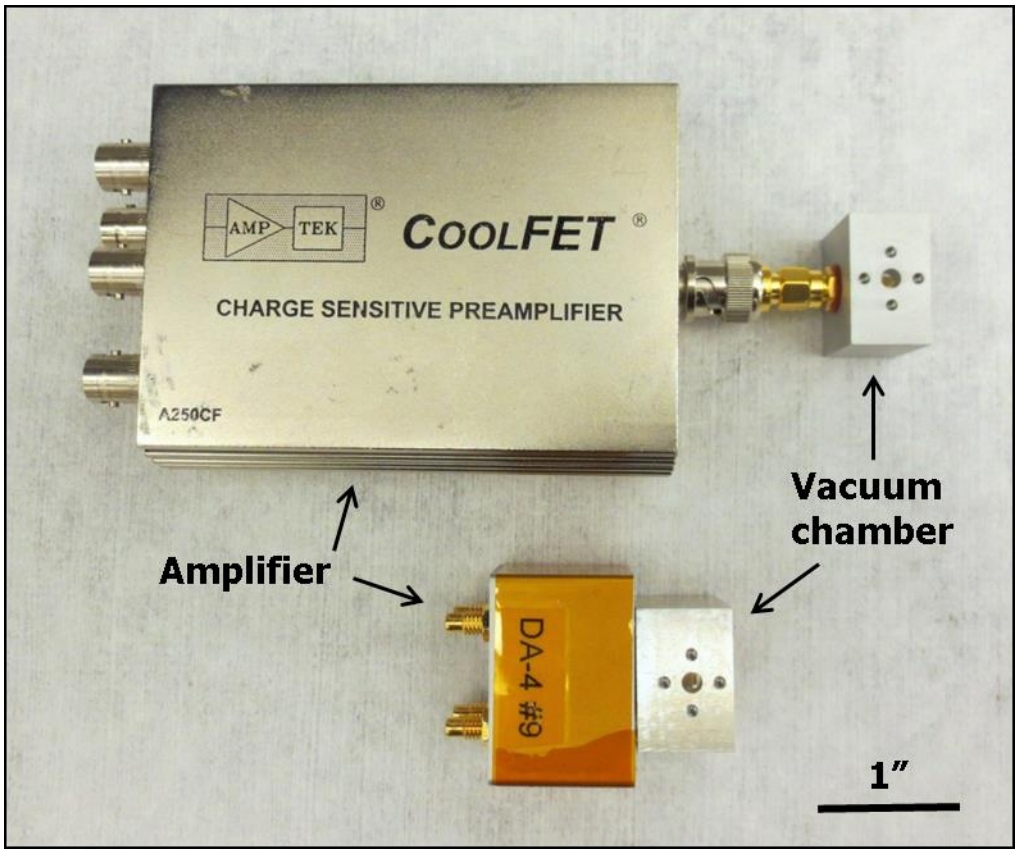

Figure 3.6: Photograph comparing the size of the commercial CoolFET amplifier to the miniaturized version (DA - 4) from 908 Devices Inc. The miniature vacuum chamber interface is also shown for each. The total SWaP for the two detectors is 12 $in.^3$, 300 g, and 5.28 W for the CoolFET, and 1.5 $in.^3$, 60 g, and 0.054 W for the DA-4. The large decrease in power draw for the DA - 4 is due to the elimination of the high-power Peltier cooling element present in the larger amplifier.

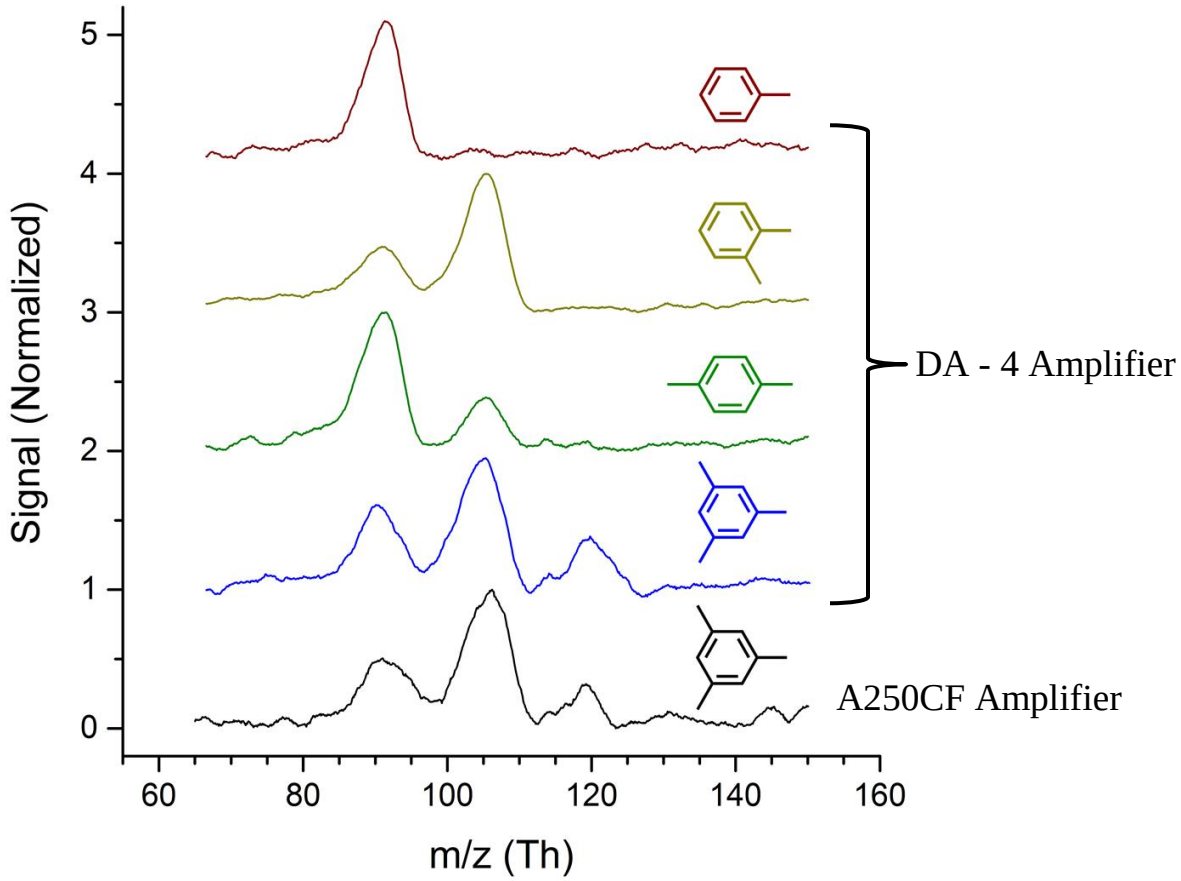

Figure 3.7: Spectra demonstrating Faraday cup detection of various benzene analogs in 1 Torr nitrogen buffer gas. The black and blue traces represent a direct comparison between the commercial A250CF Faraday cup amplifier and the custom miniaturized version (DA - 4), respectively, demonstrating similar performance. The remaining traces were taken using the DA - 4 to demonstrate that the mass of the peaks detected as well as their relative intensities can be used to discriminate between various chemically similar analytes.

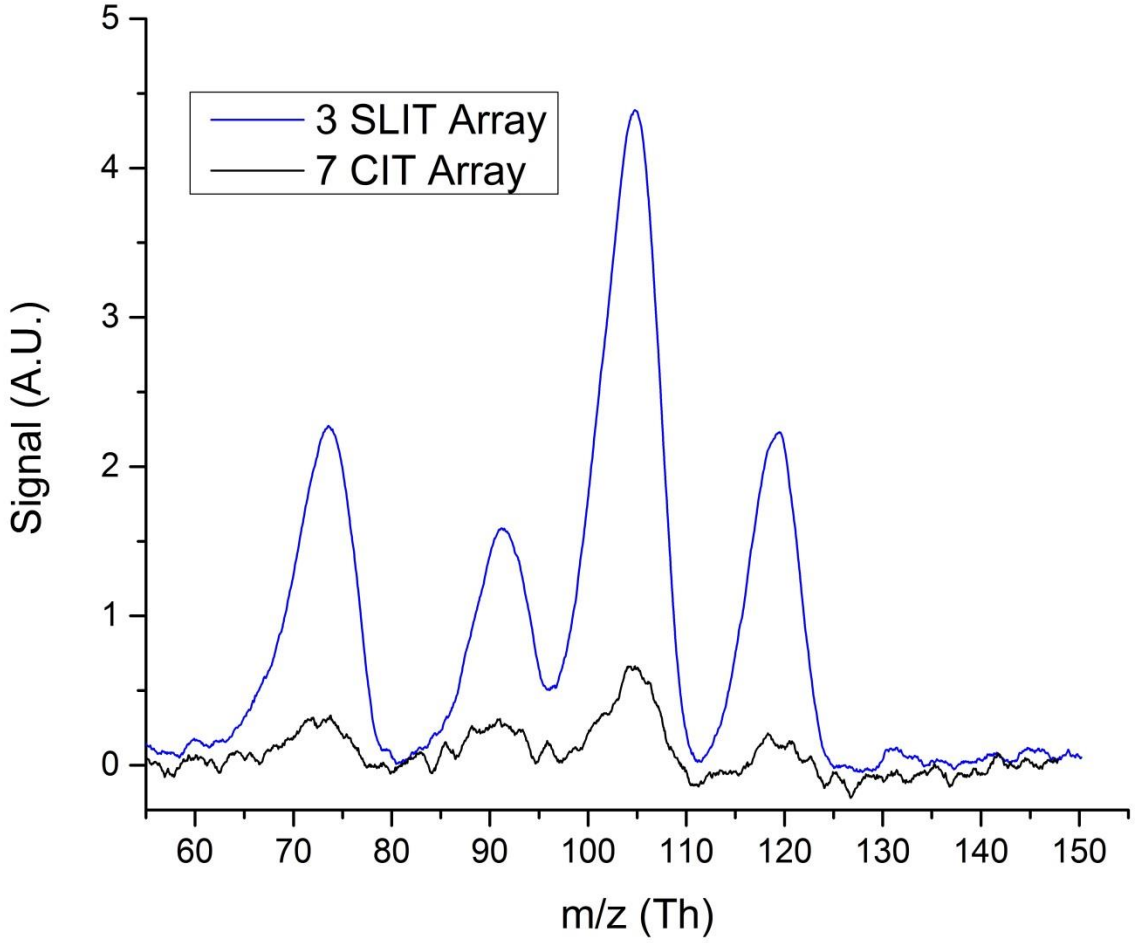

Figure 3.8: Spectra directly comparing CIT and SLIT arrays of equal footprint. For each trap, spectra were taken under identical conditions of 10 ppm mesitylene in nitrogen buffer gas. The large increase in signal intensity and signal to noise ratio is indicative of the SLIT's ability to store a greater amount of ions in the same footprint when compared to the CIT. It should be noted that the peak at 74 Th is a contaminant from the Tedlar sample bag and is otherwise not present.

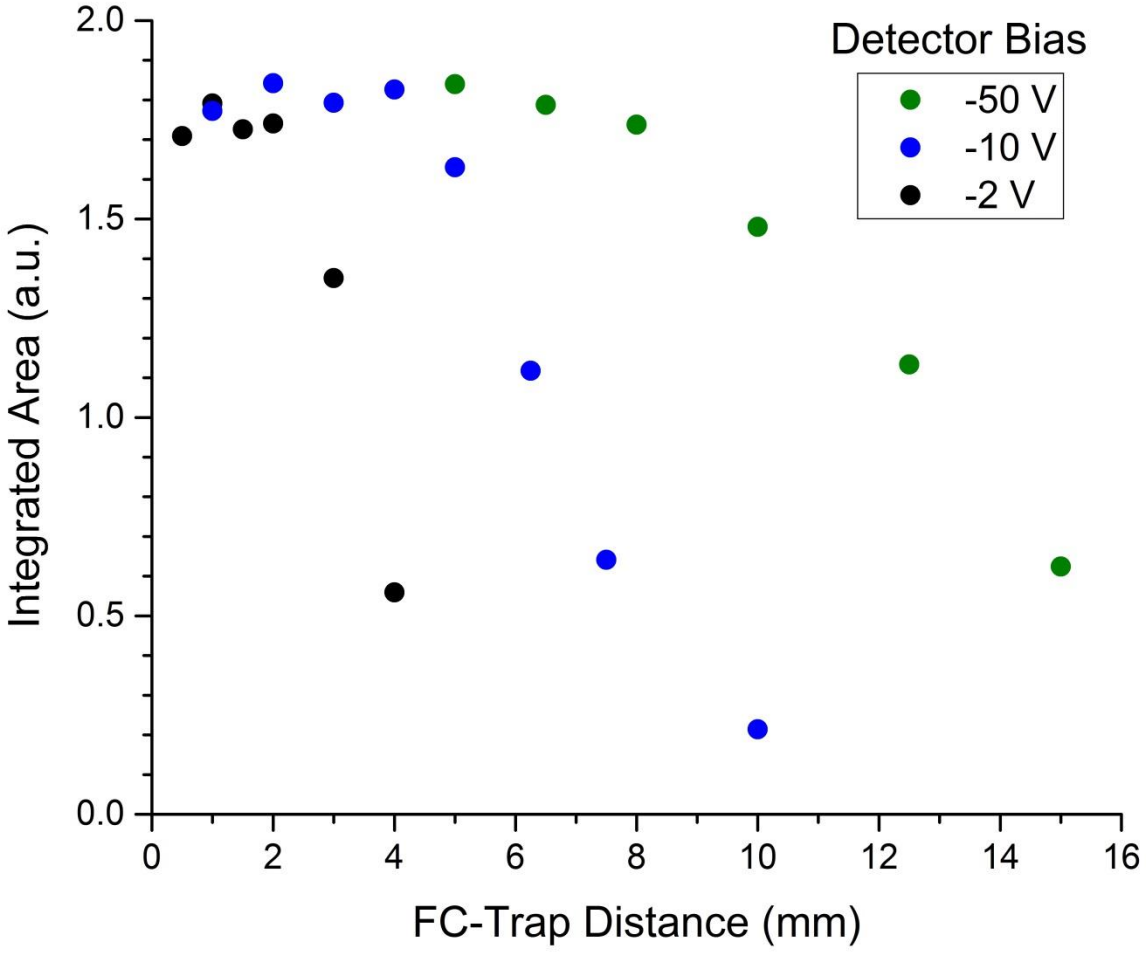

Figure 3.9: Graph plotting integrated signal intensity for detection of 1 ppm toluene in nitrogen versus Faraday cup - ion trap distance for several different Faraday cup bias voltages. As the Faraday cup is backed away from the trap, the detected signal drops. However, this can be compensated for by simply increasing the detector bias to increase the attractive force imparted on the ions.

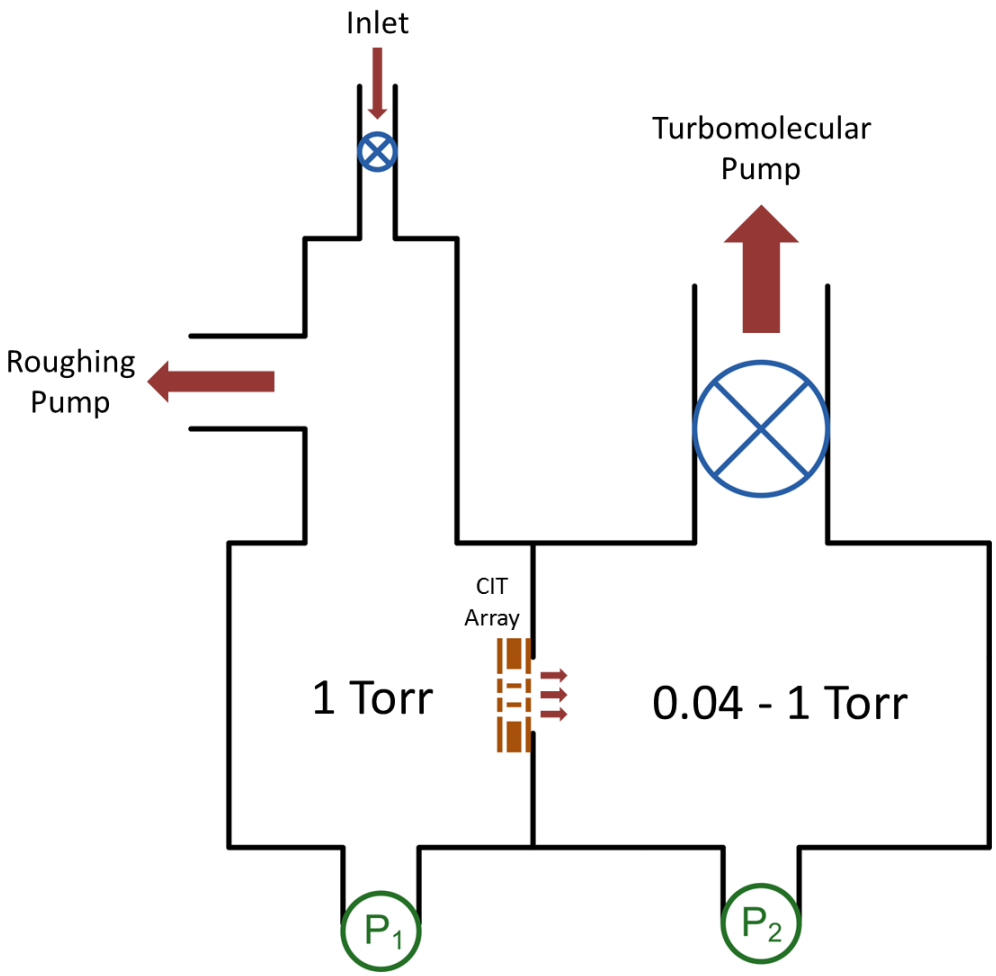

3.10: Simplified schematic diagram of the vacuum chamber used to vary the amount of gas flow through the ion trap during MS scans with gas flows marked by red arrows. To accomplish the desired flow, the two valves shown in blue were adjusted so that the chamber housing the ion trap on the left always remained at 1 Torr while the chamber housing the Faraday cup detector to the right was varied between 1 Torr and 0.04 Torr causing varying amounts of gas flow to proceed through the trap electrodes. Pressure gauges shown in green were calibrated to a capacitance manometer accurate to 0.12%.

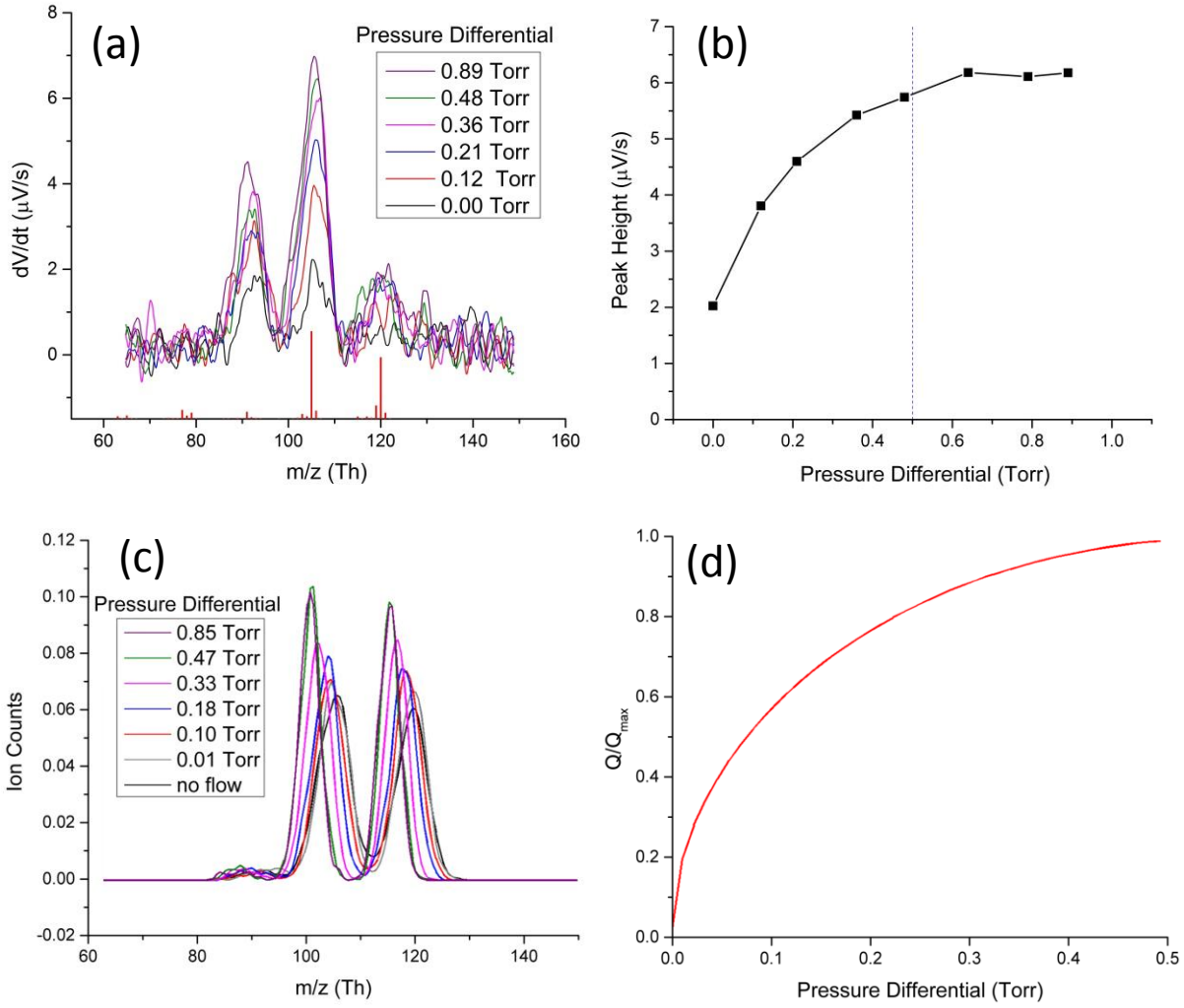

3.11: Experimental and simulations data demonstrating the rise in signal intensity upon introduction of gas flow through a microscale ion trap. Experimental mesitylene spectra (a) show an approximate 3X increase in signal intensity. The plot of peak height versus pressure differential (b) for the experiment shows a large increase upon introduction of low amounts of trap flow up to a maximum level when the pressure differential is ~2:1. Simulations of the same experimental conditions (c) again show a rise in signal intensity with flow but to a lesser extent. The peak shifting in this data was not observed experimentally and is possibly an artifact of a simulations package in its early stages of development. Finally, the magnitude of the signal increase seen experimentally seems to correspond well with the calculated gas throughput (d), showing a sharp rise followed by a leveling off of signal at a pressure differential of 2:1.

3.6 References

1. Koppenaal, D. W.; Barinaga, C. J.; Denton, M. B.; Sperline, R. P.; Hieftje, G. M.; Schilling, G. D.; Andrade, F. J.; Barnes, J. H.; Iv, I. V., MS Detectors. *Analytical Chemistry* **2005,** *77* (21), 418 A-427 A.

2. Brand, W. A., High Precision Isotope Ratio Monitoring Techniques in Mass Spectrometry. *Journal of Mass Spectrometry* **1996,** *31* (3), 225-235.

3. Imrie, D. C.; Pentney, J. M.; Cottrell, J. S., A Faraday cup detector for high-mass ions in matrix-assisted laser desorption/ionization time-of-flight mass spectrometry. *Rapid Communications in Mass Spectrometry* **1995,** *9* (13), 1293-1296.

4. Sinha, M. P.; Wadsworth, M., Miniature focal plane mass spectrometer with 1000-pixel modified-CCD detector array for direct ion measurement. *Review of Scientific Instruments* **2005,** *76* (2), -.

5. Hadjar, O.; Johnson, G.; Laskin, J.; Kibelka, G.; Shill, S.; Kuhn, K.; Cameron, C.; Kassan, S., IonCCD™ for Direct Position-Sensitive Charged-Particle Detection: from Electrons and keV Ions to Hyperthermal Biomolecular Ions. *Journal of The American Society for Mass Spectrometry* **2011,** *22* (4), 612-623.

6. Davila, S. J.; Hadjar, O.; Eiceman, G. A., Ion Profiling in an Ambient Drift Tube-Ion Mobility Spectrometer Using a High Pixel Density Linear Array Detector IonCCD. *Analytical Chemistry* **2013,** *85* (14), 6716-6722.

7. Babis, J. S.; Sperline, R. P.; Knight, A. K.; Jones, D. A.; Gresham, C. A.; Denton, M. B., Performance evaluation of a miniature ion mobility spectrometer drift cell for application in hand-held explosives detection ion mobility spectrometers. *Anal Bioanal Chem* **2009,** *395* (2), 411-419.

8. Wolfe, D. W. High-Pressure Cylindrical Ion Trap Mass Spectrometry. UNC at Chapel Hill, North Carolina, 2012.

9. Knight, A. K.; Sperline, R. P.; Hieftje, G. M.; Young, E.; Barinaga, C. J.; Koppenaal, D. W.; Denton, M. B., The development of a micro-Faraday array for ion detection. *International Journal of Mass Spectrometry* **2002,** *215* (1–3), 131-139.

10. Chambers, A., *Modern Vacuum Physics*. CRC Press: 2000.

CHAPTER 4: DEVELOPMENT OF A MINIATURIZED PROTOTYPE MASS SPECTROMETER

Introduction

Prior development of portable mass spectrometers has largely taken the top-down approach in which the components of benchtop instruments are made smaller in an iterative fashion while retaining most of the full-size system performance.[1-4] Because the mass analyzers used are still relatively large (within an order of magnitude of their conventional counterparts) and ion detection is carried out with electron multipliers, all current miniaturized mass spectrometers rely on turbomolecular vacuum pumps to achieve the low vacuum pressures necessary (10^{-3} Torr and lower).[5-16] The bottom-up approach, which builds an MS system around a microscale mass analyzer, has also received significant attention;[17-21] although to date, there have been no fully miniaturized mass spectrometry systems based around these microscale mass analyzers.

The combination of the stretched length ion trap and Faraday cup ion detectors described in the previous two chapters led to the first operation of an entire ion trapping instrument at a buffer gas pressure of 1 Torr, eliminating the need for high SWaP turbomolecular vacuum pumps. This pump elimination opens the door for development of truly handheld ion trap mass spectrometers since the heavy and power hungry vacuum pumps can be replaced with lightweight, low power roughing pumps. Traditionally, the high voltage RF system also draws a large fraction of the instrument's power, but as described earlier, the

microscale trapping dimensions ease the ion trap's RF voltage requirements, thus lowering its power usage. This chapter describes the development of a prototype handheld mass spectrometer with the focus on the hardware designed around the core MS components, i.e. the ion source, trap, and detector.

To properly frame the context of this chapter, the approximate goal specifications at the outset of this project will be described. The desired full size of the device is in the approximate range of a large digital multimeter (150-200 in^3) with a weight of around 5 lbs. in order to be easily carried for long periods of time by a single person. The power draw should be 20 W or less (approximately the power usage of an ultraportable laptop) in order to maintain a battery life of 8+ hours with a reasonably sized battery. Finally, the target for the gas throughput is in the 1-3 sccm range. This gas flow is a compromise that limits the gas load on the vacuum pumps while leaving enough of a throughput to be able to use a GC as the MS inlet in a future miniaturized GC-MS instrument.

4.1 Description of Miniaturized Vacuum Chamber

The design goal of the miniaturized vacuum chamber was to create a very small chamber for the miniature instrument prototype while still maintaining a high level of flexibility for experimental design. The chamber is made up of three sections in which each of the major ion trap components (source, trap, and detector) are held. For flexibility, this was a modular design in which any one of these sections can be swapped for one of a different design. This modularity was most commonly used to interface several different ion detectors with the instrument with no additional changes to the rest of the mass spectrometer.

An example of a fully assembled miniature vacuum chamber can be found in the lower right portion of Figure 4.1 along with the corresponding exploded view showing all the vacuum connections. Viton O-rings of various sizes were used for all vacuum seals as they are reusable and able to hold the relatively low vacuum conditions this chamber was designed for. Both the vacuum and electrical feedthroughs were made interchangeable for maximum flexibility by the use of 1/4-36 UNS threads. The vacuum feedthroughs end in a simple 1/4" O.D. aluminum tube making them compatible with several types of vacuum fittings and are used for both vacuum pumping and as ports for vacuum gauge measurement. For electrical feedthroughs, it was discovered that with the addition of a properly sized O-ring, an off-the-shelf SMA RF bulkhead connector (901-9841, Amphenol) held vacuum well enough for the moderate ~1 Torr experiments. Either sealing the vacuum side of the connector with Torr Seal brand epoxy or using vacuum grease on the atmospheric side was found sufficient to reach lower pressures if desired. Using these custom and non-traditional feedthroughs proved to be beneficial as nearly all commercial vacuum feedthroughs are too large for this application and can require soldering or welding, making them non-ideal for a flexible design. The successful use of these components led to the overall result, shown as a sectioned view and photographs in Figure 4.2, of a vacuum chamber that took up less than 30 cm^3 with an internal volume of 5 cm^3 in the smallest configurations. In the following sections the ion source, trap, and detector components will be covered in greater detail.

Glow Discharge Ion Source

Hot cathode electron emitter ion sources are not ideal for high pressure mass spectrometry in helium and nitrogen buffer gasses due to the low electron flux generated. Their oxidation upon exposure to oxygen also makes them incompatible with air buffer gas.

Lastly, the power draw of these filaments is quite high at around 5 W due to the high constant currents needed to maintain thermionic emission. For these reasons it was decided to develop a glow discharge (GD) electron source to perform electron ionization (EI) at high buffer gas pressures. In fact, GD-EI has previously been used in miniaturized instruments[22-23] due to its long lifetime and lower power draw (~0.1 W) resulting from it being a pulsed technique, only drawing power during the short ionization period of each scan function.

The design of the glow discharge electron source was based off the well-known discharge characteristics given by Paschen's Law which describes the voltage to achieve discharge between two parallel plates versus distance and pressure.[24] To achieve a glow discharge at the lowest voltage for 1 Torr of air or N_2, the ion source plates shown in Figure 4.2a were set to a1 cm distance apart via a Teflon spacer. The cathode plate (trap side) was set to a constant -250 V potential in order to accelerate the generated electrons towards the ion trap to perform EI. The anode was pulsed to a positive potential during the ionization period to yield a total ΔV typically between 350 and 600 V with the higher potentials yielding a greater flux of ionizing electrons. A photograph of the visible glow due to the source's operation can be seen in Figure 4.2c. The entire GD source doubles as part of the vacuum chamber to prevent any unwanted discharge to the walls of a surrounding chamber. For a vacuum seal, the cathode was sealed to the ion trap chamber with an oversized O-ring in order to ensure electrical isolation.

Sample and Buffer Gas Inlet

Absent from the diagrams in Figures 4.1 and 4.2 are any indicated inlets for analyte and/or buffer gas. This lack of specialized sample inlets is because the most common

practice was to simply use a needle valve (SS-SS4, Swagelok) connected to one of the 1/4" vacuum ports to leak in a mixture of buffer gas and analyte. This mixture was either ambient air with a vial of analyte held near the inlet or a Tedlar bag with a known concentration of analyte in a specified buffer gas. While this method is effective for many experiments, it creates a significant amount of dead volume leading to a slow response time of several seconds, an undesirable quality in a final miniaturized instrument. For this reason, capillary inlets were also implemented using PEEKSil tubing, that is fused silica tubing coated in PEEK polymer. The gas input can be controlled by the length of the capillary with a 50 µm I.D. tube cut to a length of 1.65 cm yielding an inlet flow rate of ~1.5 sccm at 1 Torr. The capillary inlets were potted (353ND, EPO-TEK) inside larger diameter tubing to introduce gas directly into the GD region or through one of the 1/4" vacuum ports as shown in Figure 4.3. No noticeable delay in detection was observed upon sample introduction unlike the several second response times observed with needle valve sample introduction.

Ion Trap Related Hardware

Several minor modifications were made to the ion trap construction described in earlier chapters. The footprint of the electrodes was reduced in order to fit inside a miniaturized chamber, the mounting scheme was changed to a four screw design rather than three so electrical connections matched the electrical feedthrough pattern, and custom made one-piece spacers cut from Kapton or Teflon film were used to facilitate simpler trap construction and provide more consistent spacing across the traps. Figure 4.4 shows an exploded view of this trap assembly along with a front view of a trap inside the aluminum miniature ion trap vacuum chamber. The trap is constructed on top of a removable mount so that traps can be rapidly swapped and tested without the need for disassembly. In addition to

containing the alignment pin holes for alignment of non-mesh endcaps, the mounts provide the proper spacing to align the trapping electrodes with the SMA pins for soldered electrical connection or spring fingerstock pressure connection.

Detector Modules

The greatest variation in design of the miniature vacuum system can be found in the detector module since a separate design was made for each of the Faraday cup detection systems as well as an electron multiplier; the design of all three can be seen in Figure 4.5. Figure 4.5a shows an exploded diagram of the simplest of the detector systems, a simple chamber housing a Faraday cup soldered to an SMA feedthrough. The A250CF amplifier described in Chapter 3 is then connected to the SMA on the outside of the chamber. The interface with the DA-4 detector, again described in Chapter 3, is shown in Figure 4.5b where the joint amplifier and Faraday cup are plugged into the back of the vacuum chamber by means of a radial O-ring seal. Both of these Faraday cup interface designs place the Faraday cup within a few millimeters of the ion trap and contain ports for vacuum pumping and pressure measurement.

While the focus of our lab has been the operation of the entire MS at 1 Torr of buffer gas pressure, there are several reasons to continue the development of electron multiplier based instruments that necessitate lower pressures. It has been found during prior research in our lab that electron multipliers can be operated at previously unreported pressures of 100 mTorr helium or 30-40 mTorr nitrogen/air by lowering the operating voltage to 1200-1400 V in order to prevent discharge. This suggests that moderate improvements in pumping technology could open the possibility of a handheld MS with electron multiplier detection.

In addition, applications where maximum portability is not the highest priority might be able to tolerate the higher SWaP from a small turbomolecular vacuum pump.

For these reasons, an additional detector module shown in Figures 4.5c and 4.5d was designed to accommodate an electron multiplier. The EM was held in place by a polymer front bracket and an aluminum rear bracket which also served to ground the rear connection of the multiplier to the chamber. The high voltage and signal connections were again made with SMA feedthroughs with spring fingerstock soldered to the SMA pins. It was found that pumping through a 1/4" vacuum port, even with a turbo pump, yielded pressures that were too high for EM operation, thus the pumping port size was increased as shown to accommodate a KF-16 vacuum port connection (0.69" I.D.). To limit the gas load to the detector chamber, the ion trap was limited to a single CIT (r_o = 500 μm) with 400 μm diameter endcaps or a 7 element CIT array (r_o = 500 μm) with 200 μm diameter endcaps. This setup was able to maintain detector chamber pressures in the 10-40 mTorr range while the ion trap chamber remained at 1 Torr.

As a final note, it should be mentioned that since initial development of this miniaturized vacuum chamber system, other laboratory members have expanded its capabilities by designing and implementing additional ion source modules. One module is a platform to rapidly test microfabricated cold-cathode ionizers under development, and another is an atmospheric interface to transport externally generated ions into the ion trap. These developments further illustrate the utility and flexibility of this miniature chamber design.

4.2 Demonstration of Miniaturized Vacuum Chamber Operation

One of the benefits of the miniature chamber described in the previous section is the reduction of the capacitive load that the RF system has to drive. This reduction is due to the smaller footprint trapping electrodes and the elimination of cabling inside the vacuum chamber present in the full size differential systems. A smaller capacitance for the RF tank circuit makes it possible to achieve even higher RF frequencies. As described in Chapter 2, operating microscale ion traps at higher frequencies is an effective way to mitigate peak broadening arising from operation at high buffer gas pressures. To demonstrate the ability of performing MS at higher frequencies, mass spectra of *o*-xylene were taken at 1 Torr air using the miniature chamber at RF frequencies ranging from 6 to 10 MHz. The spectra, shown in Figure 4.6, were taken with a 7 element CIT array (r_o = 500 μm) using the DA-4 (biased to -75 V) as the detector. In this case, only a modest decrease in peak width was observed from 6.6 Th FWHM at 6 MHz to 5.9 Th at 10 MHz (possibly due to CIT array variability). However, the ion trap's well depth was seen to improve with frequency as expected (~7 V to 12 V at q_z = 0.4), evidenced by the improved trapping of the low mass 77 Th peak. Further work by others in the laboratory have taken advantage of the miniature system's low capacitance (~25 pF) to obtain spectra at RF frequencies as high as 60 MHz. The similarity of the spectra presented in Figure 4.6 to those previously observed in the full size differential chambers (Figure 2.16 for example) suggests that there are no adverse effects on the data upon the system's miniaturization.

Despite the higher complexity of the electron multiplier module as well as concerns about the high voltages required, the miniature vacuum chamber was successfully operated with EM detection. The comparison of spectra taken with the EM and DA-4 modules shown

in Figure 4.7 illustrates some of the motivation for continuing with EM development. The most important difference is an improved signal to noise ratio (65 versus 22) observed with the electron multiplier. The post-peak baseline shifting observed in the Faraday cup spectrum due to the DA-4's amplification scheme is also absent in the EM spectrum, eliminating data processing needs for baseline correction. Signal to noise values were determined for a known concentration of toluene (10 ppm) in nitrogen to be as high as 420 for a 500 scan average, extrapolating to a limit of detection of 71 ppb at 3X the signal to noise level. LOD data for Faraday cup based systems were determined with a GC inlet and are presented in Chapter 5.

4.3 Miniaturized Prototype Mass Spectrometer

After successful miniaturization of the vacuum chamber and the associated MS components, a project was undertaken to miniaturize the remaining components of the mass spectrometer to create a functional prototype that could be operated with a laptop computer. Because the path to miniaturization of all the DC components (detector power supply, pulsed GD supply, etc.) is relatively straightforward, the focus of the work was largely on the vacuum pumping and RF voltage systems. Because of the high operating pressure of the MS, it was possible to use a small prototype scroll pump from Air Squared as the only vacuum pump. This pump was able to achieve 1 Torr of pressure while drawing only 3.4 W.

The miniature RF system, a diagram of which can be found in Figure 4.8, was designed in collaboration with RF consultant Harry Chase. The class D amplifier used was built around the IRF510 power MOSFET and feeds into a resonant tank circuit as with the full sized instruments. To save space, a compact ferrite-wound inductor was used in place of

the large air-core inductors used in previous miniature ion trap instruments.[1, 4, 23] Operated at 7.63 MHz, this RF system consumes an average of 4.8 W. Combining the miniature vacuum chamber, vacuum pump, and RF system, a handheld prototype was constructed weighing only 2 lbs and drawing 8.2 W from the onboard components. An image of the prototype can be seen in Figure 4.9. The instrument is controlled by a laptop computer connected to a small USB DAQ (NI-6363, National Instruments). The MS components included a capillary atmospheric inlet, 3 element SLIT array, and DA-4 based Faraday cup detection. An example of detection of an ambiently sampled organic compound, mesitylene, can be seen in Figure 4.10.

As mentioned before, the cables running to the prototype seen in Figure 4.10 consist of the signal out cable and DC signals that are straightforward to miniaturize. For the sake of completeness, the different signals are as follows: two glow discharge electrode voltages, square wave RF frequency input, RF modulation input, +12 V RF power supply, +4.5 V vacuum pump supply, -50 V FC bias supply, and +/- 3.3 V FC power supply.

4.4 Conclusions

An engineering effort has been made to package the components of a microscale ion trap into a miniaturized vacuum chamber. The result was a modular design that retained maximum experimental flexibility while still remaining small enough to be used in a miniaturized prototype MS. With the addition of a miniature RF system and vacuum pump, a functional prototype was constructed weighing just 2 lbs with a power draw of only 8.2 W.

4.5 Figures

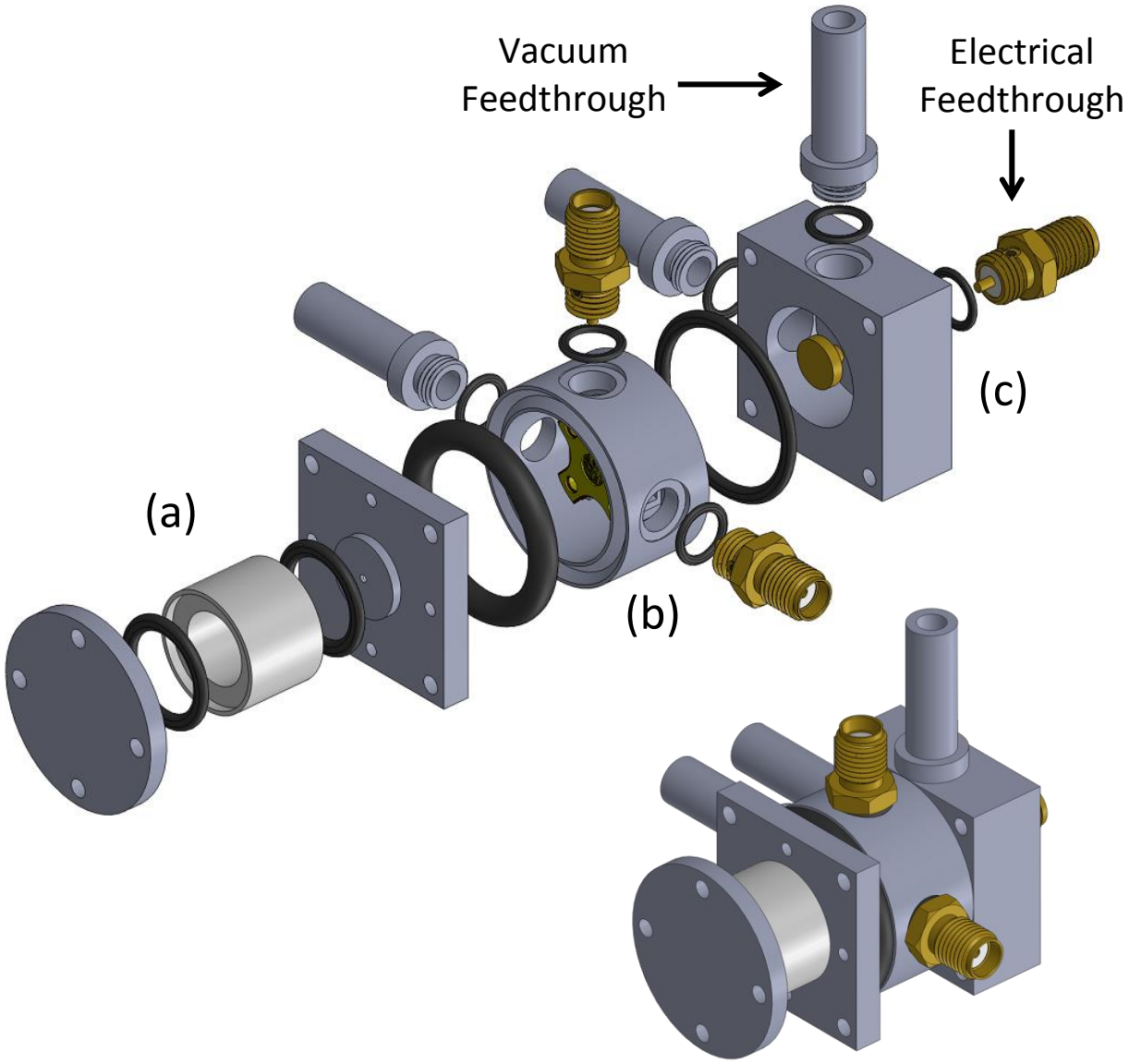

Figure 4.1: Exploded and constructed views of the modular miniature vacuum chamber showing the three major components; the ion source module (a), the ion trap module (b), and the detector module (c). The interchangeable electrical and vacuum feedthroughs can also be seen. This design allows for flexibility in both number and type of feedthroughs in the trap and detector modules.

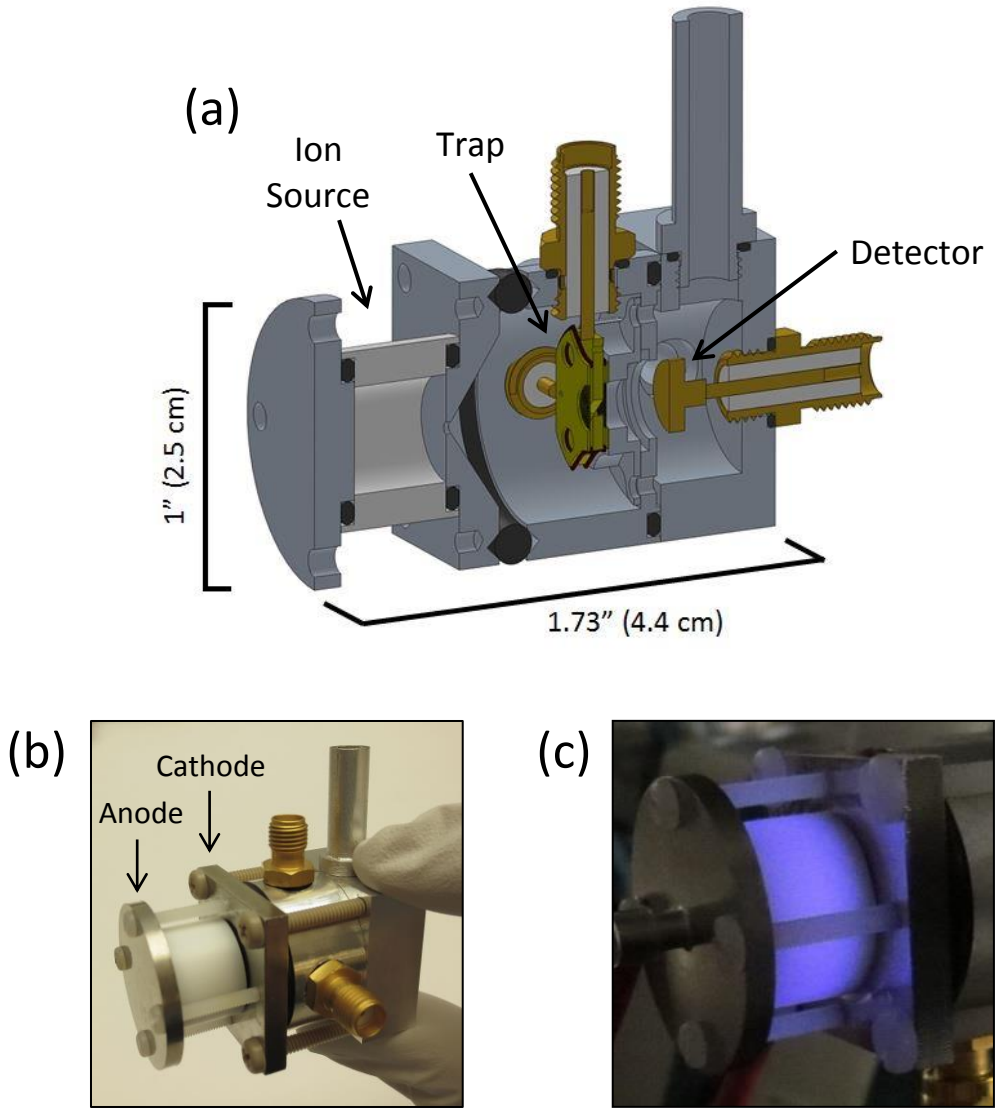

Figure 4.2: Sectioned view (a) of the miniature chamber from Figure 4.1 showing the types of O-ring vacuum seals as well as the relative positions of the source, trap, and detector. A photograph of the constructed chamber (b) is given for scale. Upon operation, the glow discharge (c) can be observed by a faint blue light emitted between the electrodes.

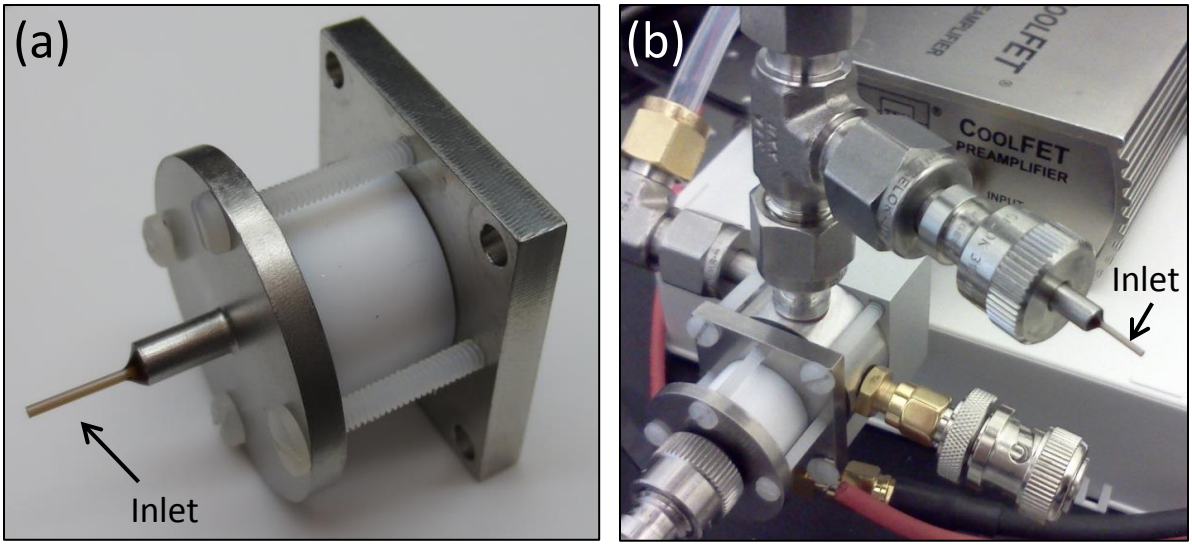

Figure 4.3: Images of the two methods of buffer gas and sample introduction with a capillary inlet. A 1.65 cm long, 50 µm I.D. PEEKSil capillary was potted into 1/8" tubing and placed to introduce sample/buffer gas into the glow discharge region (a) or through one of the 1/4" vacuum ports in the trap or detector modules (b).

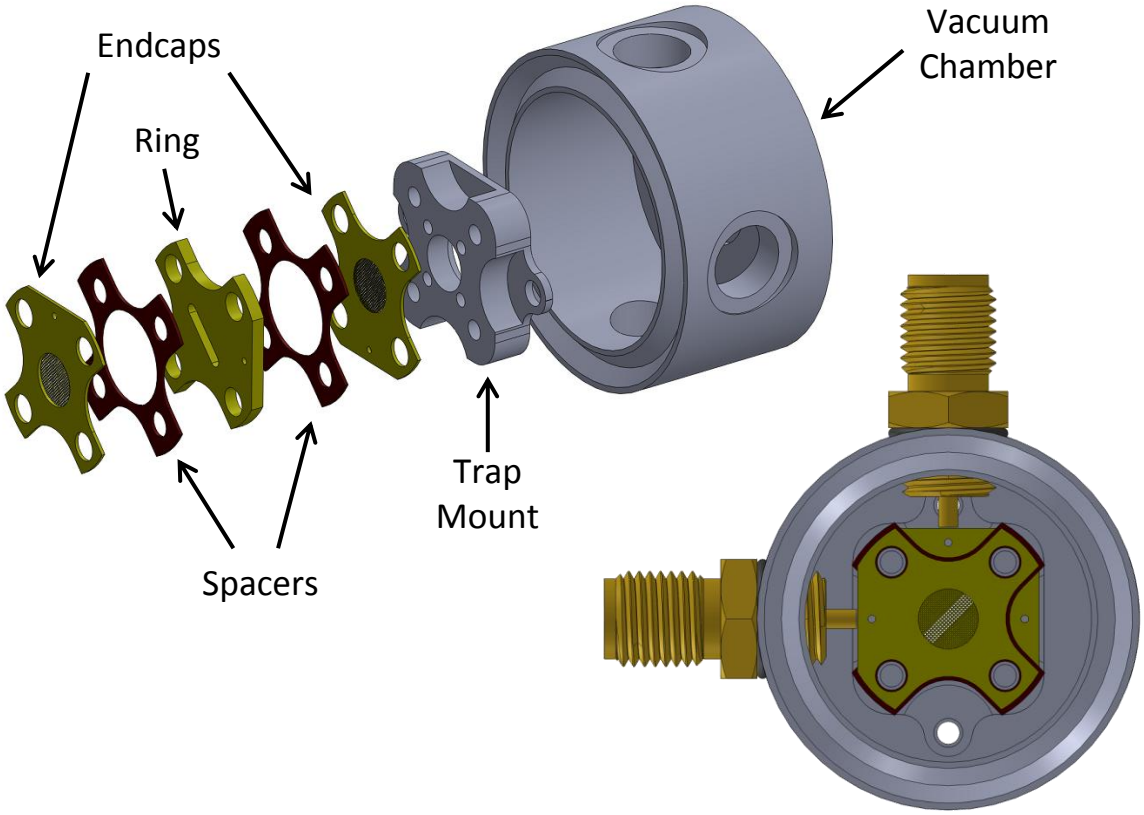

Figure 4.4: Images showing the detail of trap module construction. The exploded view demonstrates how the compact trapping electrodes and custom cut Kapton spacers attach to the removable trapping mount. The constructed view shows the close proximity of the SMA feedthrough pins to the trapping electrodes which facilitate soldering for electrical connection.

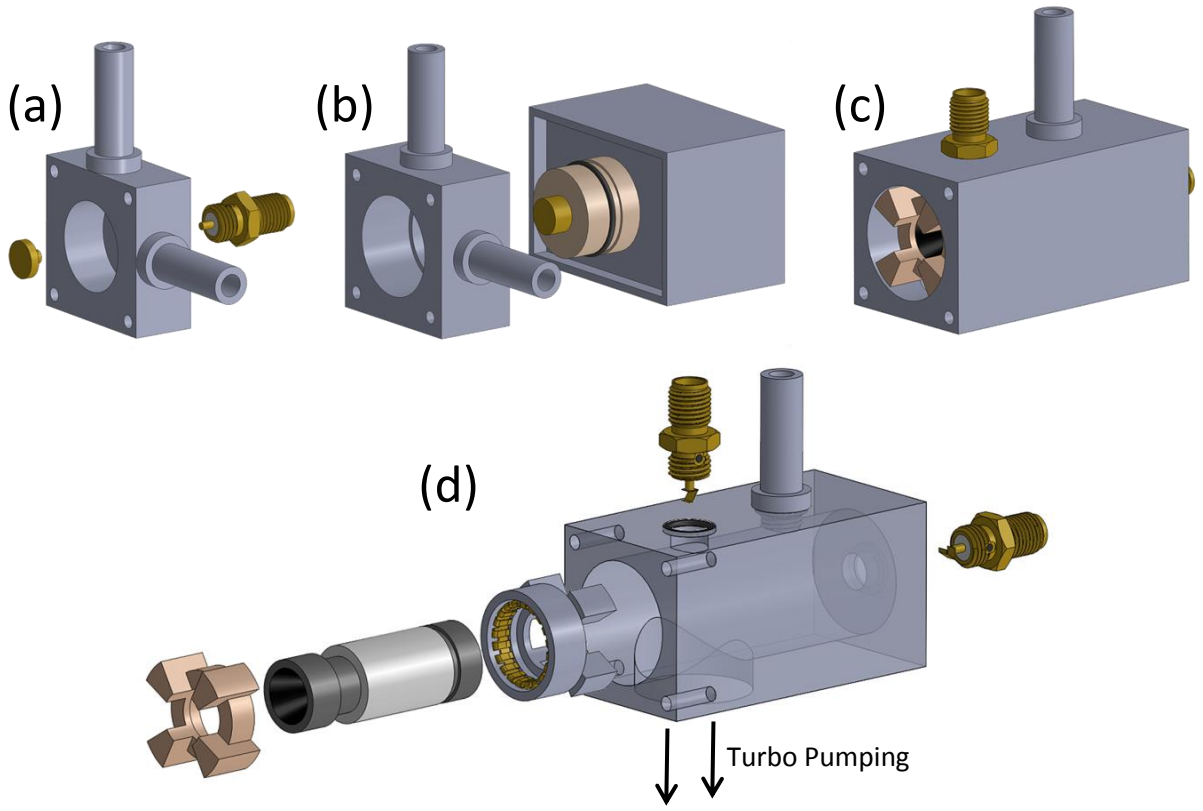

Figure 4.5: Graphic renderings of the various ion detector modules. The A250CF interface module (a) consists of a simple Faraday plate soldered directly to the pin of an SMA which then connects to the A250CF amplifier. In the DA-4 module (b), the DA-4 FC amplifier plugs directly into the back of the vacuum chamber with a radial O-ring seal. The electron multiplier module (c) with the associated exploded view (d) shows how the EM is held in place with a PEEK front spacer and an aluminum rear spacer which grounds the rear of the EM. The signal out and high voltage electrical connections are made by SMA feedthroughs with finger spring connections as shown. Because the EM must remain at lower pressure than the FC modules, a larger pumping port was drilled out of the bottom of the module and pumped with a turbomolecular pump to increase pumping speed.

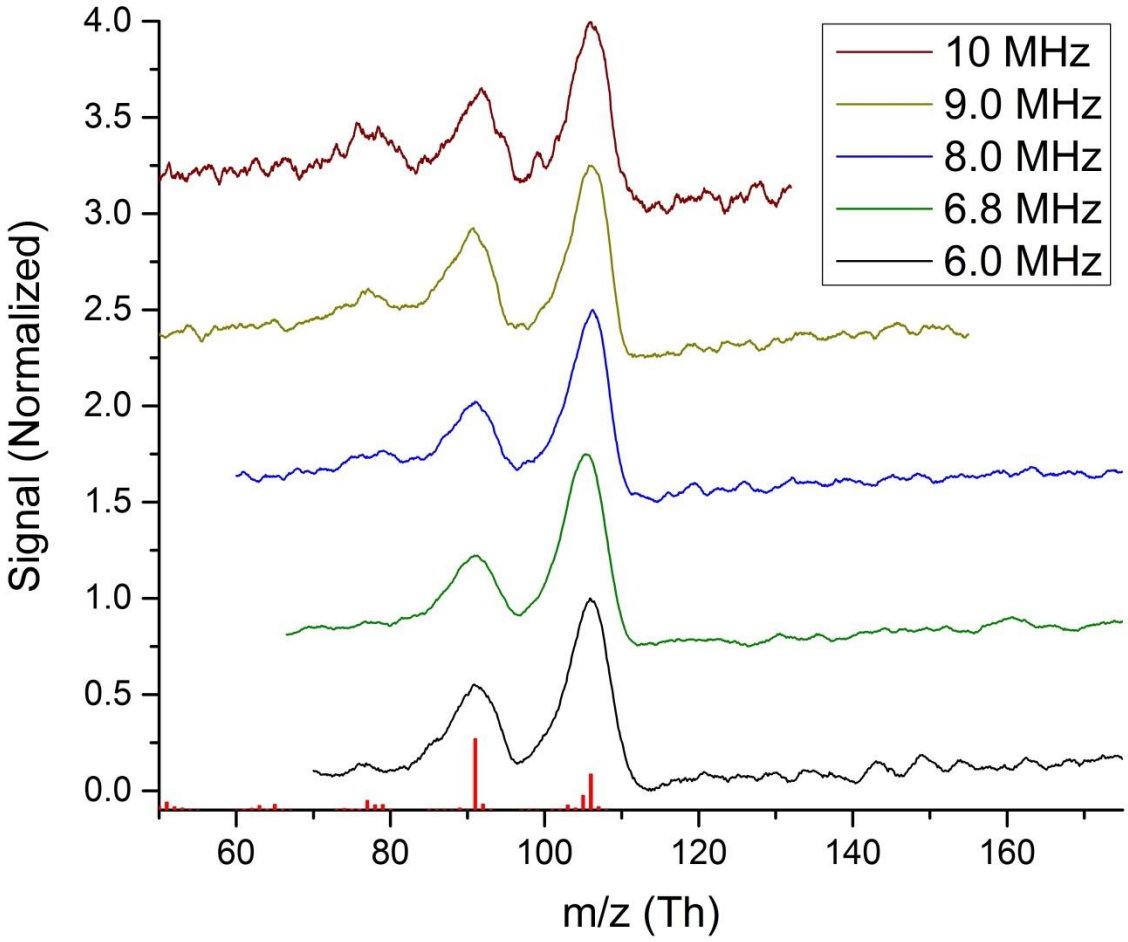

Figure 4.6: Spectra of *o*-xylene taken at increasing RF frequencies using the miniature vacuum chamber with DA-4 based Faraday cup detection. Due to the potential well depth increase, the lower mass 77 Th ion is more effectively trapped at the higher RF frequencies.

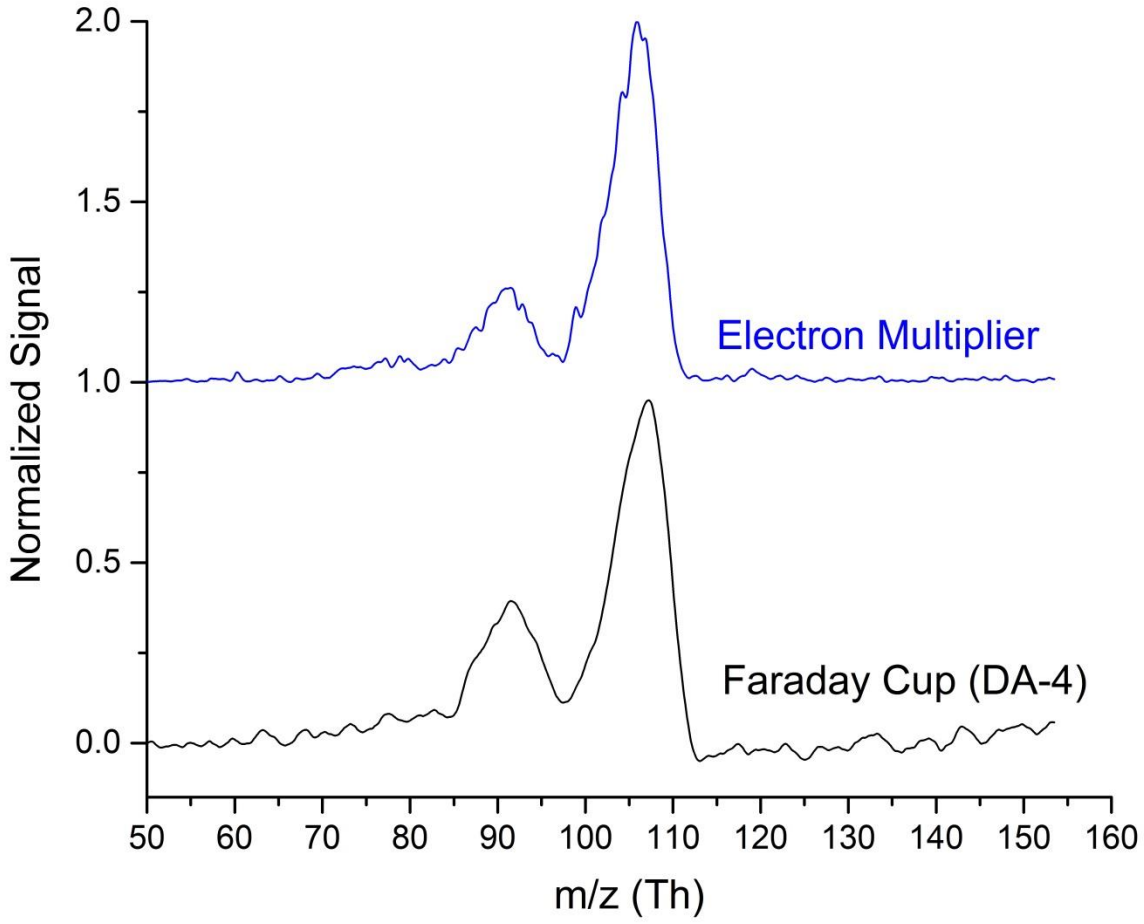

Figure 4.7: Comparison of *o*-xylene spectra taken using the miniaturized vacuum chamber with the electron multiplier and Faraday cup (DA-4) modules. The signal to noise ratios are 65 and 22 for the electron multiplier and Faraday cup spectra, respectively. The electron multiplier spectrum also shows no baseline artifacts that are present in the Faraday cup spectrum.

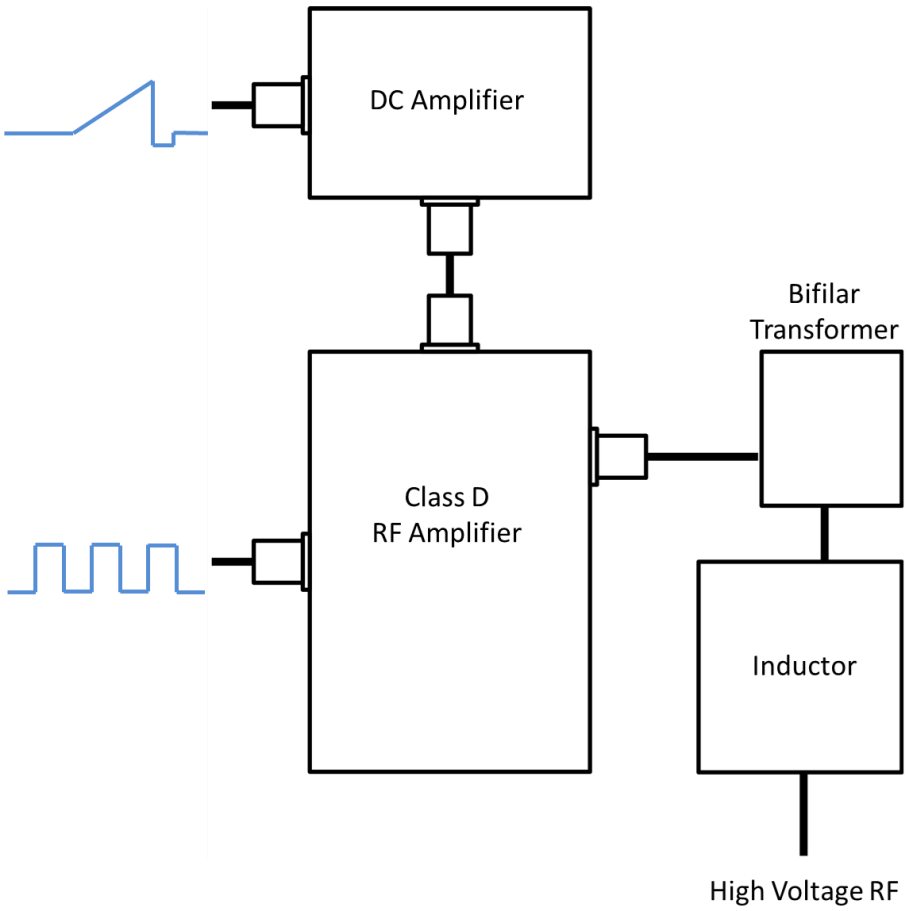

Figure 4.8: The layout of the miniature RF amplification system. Low voltage signals (in blue) are fed into the amplifier circuits. The DC modulation signal and square wave of the proper RF frequency are combined and amplified by the class D amplifier. This is fed through a bifilar 2:1 power transformer and resonant tank circuit to yield modulated trapping RF voltage.

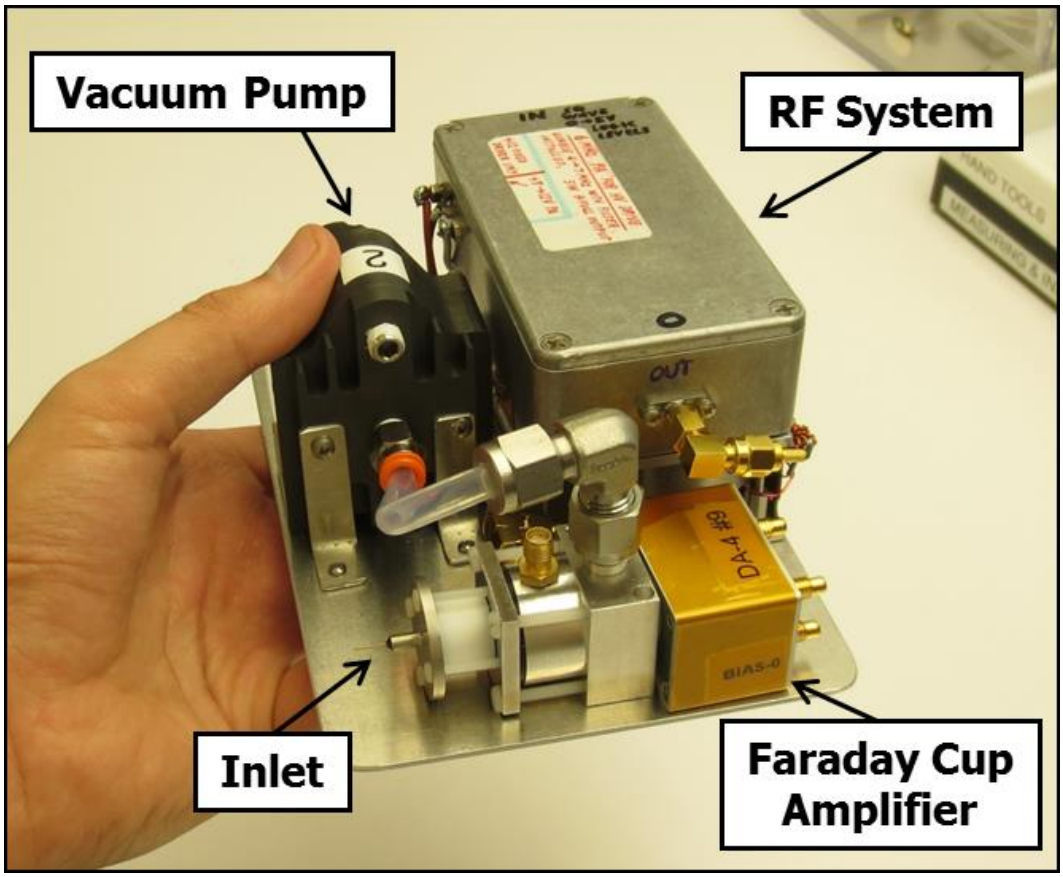

Figure 4.9: Photograph of the miniature prototype with the major components marked.

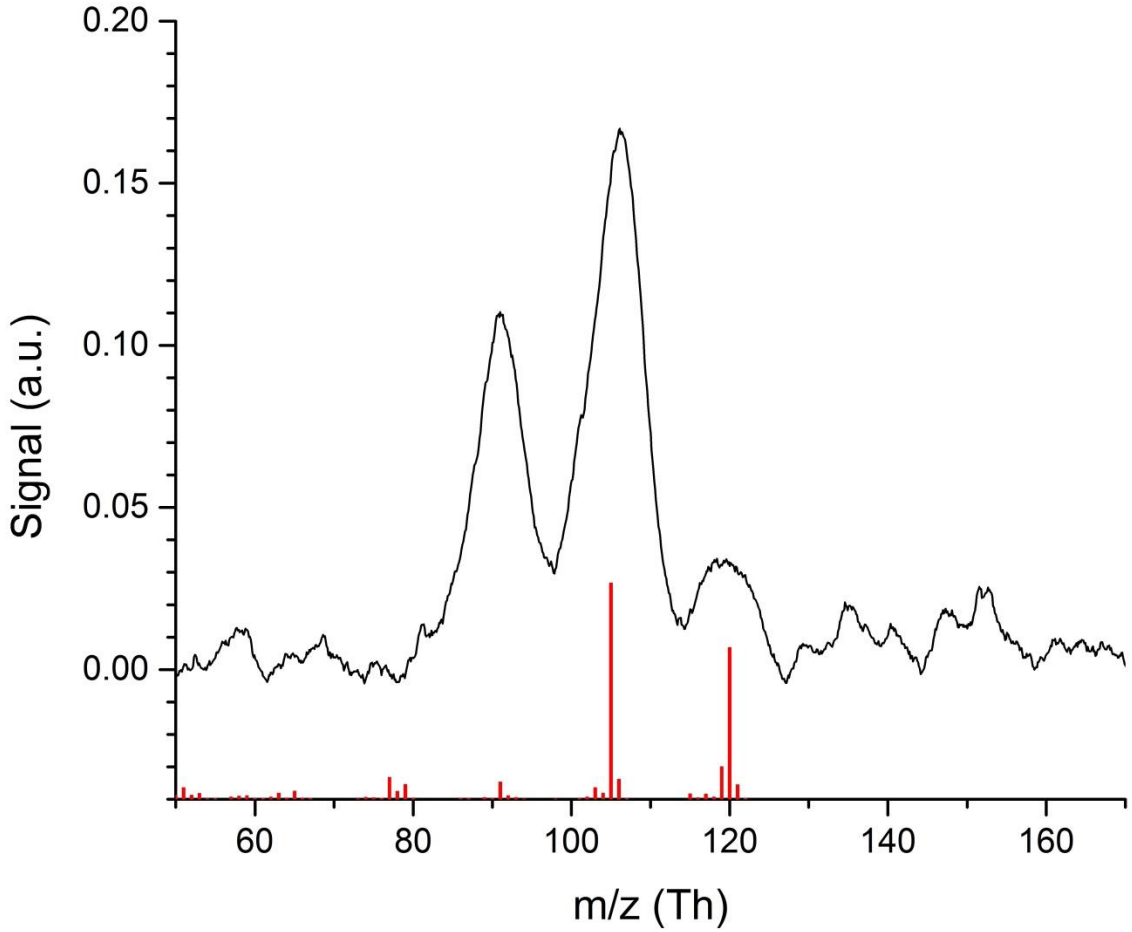

Figure 4.10: Mass spectrum of ambiently sampled mesitylene taken using the miniature prototype mass spectrometer from Figure 4.9. Performance is roughly equivalent to the full size mass spectrometers used previously.

4.6 References

1. Ouyang, Z.; Noll, R. J.; Cooks, R. G., Handheld Miniature Ion Trap Mass Spectrometers. *Analytical Chemistry* **2009,** *81* (7), 2421-2425.

2. Patterson, G. E.; Guymon, A. J.; Riter, L. S.; Everly, M.; Griep-Raming, J.; Laughlin, B. C.; Zheng, O.; Cooks, R. G., Miniature Cylindrical Ion Trap Mass Spectrometer. *Anal. Chem.* **2002,** *74* (24), 6145-6153.

3. Riter, L. S.; Peng, Y.; Noll, R. J.; Patterson, G. E.; Aggerholm, T.; Cooks, R. G., Analytical Performance of a Miniature Cylindrical Ion Trap Mass Spectrometer. *Analytical Chemistry* **2002,** *74* (24), 6154-6162.

4. Gao, L.; Song, Q.; Patterson, G. E.; Cooks, R. G.; Ouyang, Z., Handheld Rectilinear Ion Trap Mass Spectrometer. *Anal. Chem.* **2006,** *78* (17), 5994-6002.

5. Lammert, S. A.; Rockwood, A. A.; Wang, M.; Lee, M. L.; Lee, E. D.; Tolley, S. E.; Oliphant, J. R.; Jones, J. L.; Waite, R. W., Miniature Toroidal Radio Frequency Ion Trap Mass Analyzer. *Journal of the American Society for Mass Spectrometry* **2006,** *17* (7), 916-922.

6. Contreras, J. A.; Murray, J. A.; Tolley, S. E.; Oliphant, J. L.; Tolley, H. D.; Lammert, S. A.; Lee, E. D.; Later, D. W.; Lee, M. L., Hand-portable gas chromatograph-toroidal ion trap mass spectrometer (GC-TMS) for detection of hazardous compounds. *J. Am. Soc. Mass Spectrom.* **2008,** *19* (10), 1425-1434.

7. Gao, L.; Cooks, R. G.; Ouyang, Z., Breaking the Pumping Speed Barrier in Mass Spectrometry: Discontinuous Atmospheric Pressure Interface. *Analytical Chemistry* **2008,** *80* (11), 4026-4032.

8. Hendricks, P.; Duncan, J.; Noll, R. J.; Ouyang, Z.; Cooks, R. G., Performance of a low voltage ion trap. *International Journal of Mass Spectrometry* **2011,** *305* (1), 69-73.

9. Fico, M.; Yu, M.; Ouyang, Z.; Cooks, R. G.; Chappell, W. J., Miniaturization and Geometry Optimization of a Polymer-Based Rectilinear Ion Trap. *Anal. Chem.* **2007,** *79* (21), 8076-8082.

10. Fico, M.; Maas, J. D.; Smith, S. A.; Costa, A. B.; Ouyang, Z.; Chappell, W. J.; Cooks, R. G., Circular arrays of polymer-based miniature rectilinear ion traps. *Analyst* **2009,** *134* (7), 1338-1347.

11. Maas, J. D.; Hendricks, P. I.; Ouyang, Z.; Cooks, R. G.; Chappell, W. J., Miniature Monolithic Rectilinear Ion Trap Arrays by Stereolithography on Printed Circuit Board. *J. Microelectromech. Syst.* **2010,** *19* (4), 951-960.

12. Li, X. X.; Jiang, G. Y.; Luo, C.; Xu, F. X.; Wang, Y. Y.; Ding, L.; Ding, C. F., Ion Trap Array Mass Analyzer: Structure and Performance. *Anal. Chem.* **2009,** *81* (12), 4840-4846.

13. Taylor, N.; Austin, D. E., A simplified toroidal ion trap mass analyzer. *Int. J. Mass Spectrom.* **2012,** *321*, 25-32.

14. Austin, D. E.; Wang, M.; Tolley, S. E.; Maas, J. D.; Hawkins, A. R.; Rockwood, A. L.; Tolley, H. D.; Lee, E. D.; Lee, M. L., Halo ion trap mass spectrometer. *Anal. Chem.* **2007,** *79* (7), 2927-2932.

15. Zhang, Z.; Peng, Y.; Hansen, B. J.; Miller, I. W.; Wang, M.; Lee, M. L.; Hawkins, A. R.; Austin, D. E., Paul Trap Mass Analyzer Consisting of Opposing Microfabricated Electrode Plates. *Anal Chem* **2009,** *81* (13), 5241-5248.

16. Peng, Y.; Hansen, B. J.; Quist, H.; Zhang, Z.; Wang, M.; Hawkins, A. R.; Austin, D. E., Coaxial Ion Trap Mass Spectrometer: Concentric Toroidal and Quadrupolar Trapping Regions. *Anal. Chem.* **2011,** *83* (14), 5578-5584.

17. Kornienko, O.; Reilly, P. T. A.; Whitten, W. B.; Ramsey, J. M., Micro ion trap mass spectrometry. *Rapid Communications in Mass Spectrometry* **1999,** *13* (1), 50-53.

18. Pau, S.; Whitten, W. B.; Ramsey, J. M., Planar Geometry for Trapping and Separating Ions and Charged Particles. *Analytical Chemistry* **2007,** *79* (17), 6857-6861.

19. Pau, S.; Pai, C. S.; Low, Y. L.; Moxom, J.; Reilly, P. T.; Whitten, W. B.; Ramsey, J. M., Microfabricated quadrupole ion trap for mass spectrometer applications. *Phys. Rev. Lett.* **2006,** *96* (12), 120801.

20. Van Amerom, F. H. W.; Chaudhary, A.; Cardenas, M.; Bumgarner, J.; Short, R. T., Microfabrication of Cylindrical Ion Trap Mass Spectrometer Arrays for Handheld Chemical Analyzers. *Chem. Eng. Commun.* **2008,** *195* (2), 98 - 114.

21. Cruz, D.; Chang, J. P.; Fico, M.; Guymon, A. J.; Austin, D. E.; Blain, M. G., Design, microfabrication, and analysis of micrometer-sized cylindrical ion trap arrays. *Rev. Sci. Instrum.* **2007,** *78* (1), 015107/1-015107/9.

22. Gao, L.; Song, Q.; Noll, R. J.; Duncan, J.; Cooks, R. G.; Ouyang, Z., Glow discharge electron impact ionization source for miniature mass spectrometers. *Journal of Mass Spectrometry* **2007,** *42* (5), 675-680.

23. Gao, L.; Sugiarto, A.; Harper, J. D.; Cooks, R. G.; Ouyang, Z., Design and Characterization of a Multisource Hand-Held Tandem Mass Spectrometer. *Anal. Chem.* **2008,** *80* (19), 7198-7205.

24. Paschen, F., On the potential difference required for spark initiation in air, hydrogen, and carbon dioxide at different pressures. *Annalen der Physik* **1889,** *273* (5), 69-96.

CHAPTER 5: HIGH PRESSURE MASS SPECTROMETRY DETECTION FOR GAS CHROMATOGRAPHY

Introduction

Previous chapters have described the development of miniaturized ion trap MS instrumentation made possible by operation at unconventionally high pressures *ca.* 1 Torr. A consequence of high pressure operation is a decrease in ion trap resolution leading to a reduction in instrument selectivity; that is, the ability to which the instrument can identify an analyte in the presence of other compounds in a matrix. There are several strategies to regain selectivity, one of which is to increase the RF drive frequency of the ion trap in order to regain lost resolution. This method is currently being successfully implemented by others in our laboratory on benchtop instruments. However, it is currently unclear if these high frequencies can be generated by hardware with low enough SWaP for a handheld instrument. The subject of this chapter is another strategy to improve the selectivity of HPMS, adding a gas chromatographic separation step prior to mass spectrometry.

Gas chromatography (GC), first demonstrated in 1952,[1] uses a gas mobile phase and a liquid/polymer phase to separate a mixture of analytes prior to detection. While this first demonstration used a large diameter packed column, open tubular columns were eventually found to give higher performance in terms of chromatographic resolution and analysis times.[2-3] A further increase in performance came with the introduction of fused silica capillary columns.[4] Nearly all modern GC instruments utilize one of these narrow bore fused

silica capillary columns, typically between 50 and 500 μm in internal diameter and 5 to 30 or more meters in length, that are held in a temperature controlled oven. This open tubular column is coated with a thin layer (0.1 - 10.0 μm) of a high molecular weight polymer stationary phase. The sample is introduced through a heated inlet causing the analytes to vaporize and be swept down the column by the carrier gas, usually He, H_2, or N_2. While travelling down the column the analyte partitions between the gaseous mobile phase and the liquid stationary phase, with analytes that spend more time in the stationary phase having a slower effective velocity through the column. This partitioning is determined by the physical properties of each analyte and causes the mixture to separate into different bands as it moves down the column, eventually being detected in the order in which the bands elute. In general, analytes with higher boiling points take longer to elute. In order to shorten run times and elute narrow peaks for analytes with a wide range of boiling points, the oven temperature is usually increased with time analogous to mobile phase gradients in liquid chromatography.

The majority of the SWaP associated with benchtop GC instrumentation comes from the oven in which the GC column is housed. A large physical size (typically several cubic feet) is needed to accommodate the up to 60 m long loosely coiled fused silica column while convective heating in the oven draws a very large amount of power (greater than 3000 W for fast temperature ramps) and requires long cooling times in between runs.[5] On the surface, these specifications portray GC as an undesirable candidate for portable instrumentation; however, it has long been realized that the fused silica GC column itself represents a low thermal mass and could be temperature controlled via relatively low power direct resistive heating.[6] In fact, low power methods that do not rely on bulky convection heating have been key in creating field portable and even handheld GC instrumentation.[7]

To avoid large power draws from temperature ramping, early portable GC systems utilized ambient temperatures[8-9] or isothermal heating,[10] limiting analysis to a narrow range of analyte volatilities. Later work incorporated temperature ramps by heating the capillary with resistive wire in contact with the column[11] or direct resistive heating of metal clad columns.[12] These heating methods were efficient enough to be used under battery power. GC columns based on microelectromechanical systems (MEMS), i.e. chip-based columns, are another means to create low thermal mass columns with the added benefit of being able to incorporate column heating and cooling into the MEMS device. The first chip-based column was demonstrated in 1979[13] with further work continuing through today.[14-20] These devices require much lower power (25 W or less average power) and even open the possibility of unconventional GC operation such as introduction of temperature gradients along the column for peak focusing.[21-22] Microfabrication techniques have progressed to the point where several components such as preconcentrators, columns, and detectors can all be integrated into a single MEMS device.[23]

Because the analytes exit the column already in the gas phase, GC pairs well with mass spectrometry (MS) detection. This inherent compatibility was confirmed by the fact that tandem GC-MS operation was first realized in 1957[24] (although not published until 1959), shortly after the invention of GC. Although this first example paired GC with a time-of-flight (TOF) mass analyzer, the majority of early GC-MS work was conducted with sector instruments. Over the years, GC-MS has become the gold standard in analysis for numerous industries and applications.[25] The most common mass analyzer for GC-MS is a single quadrupole, however, more powerful analytical methods are provided by tandem mass spectrometry (GC-MS/MS) performed by triple quadrupole or quadrupole-TOF instruments.

Relevant to this work, ion traps also enjoyed a long period of use in GC-MS instruments partially due to the preferred GC carrier gas, helium, also being the ideal ion trap buffer gas. Recall from Chapter 1 that the first appearance of a commercial ion trap mass analyzer was as the detector in a GC-MS system.[26]

Not surprisingly, several research efforts have attempted to design portable GC-MS systems. Because of the long history of interfacing sector mass spectrometers with early GCs, the first portable GC-MS instrument utilized a miniaturized sector analyzer to achieve a suitcase-sized instrument.[27] Other early applications involved space exploration[28] where SWaP is one of several concerns including automation and reliability. Research and development of fieldable GC-MS systems has led to several commercial instruments, including the linear quadrupole based Hapsite GC-MS from Inficon and several ion trap based instruments (Griffin 400, FLIR; and Tridion, Torion Technologies; Guardion, Smiths Detection).[29] While these instruments retain most of the analytical capability of their laboratory counterparts, their miniaturization has plateaued in the 30 to 40 lb. range. The weight of these systems combined with short battery lives of only a few hours limits the applications of current portable GC-MS instruments. Starting with a mass spectrometer weight in the range of 4-5 lbs., a HPMS based system opens the possibility of a handheld GC-MS that can be comfortably carried and operated for long periods of time in the field.

5.1 GC-MS Instrumentation

In addition to the performance goals previously described for the handheld mass spectrometer (5 lb. weight, 20 W power draw, etc.) there are several specification goals for the proposed GC-MS instrument. First, a GC flow rate of 1-3 mL/min is desirable in order to

be compatible with the current HPMS instrumentation without having to use split flow for detection. In order to keep the analysis time short, 1 minute GC separations are targeted with peak widths in the 1 second range. This analysis time constrains the MS data acquisition speed to the limit of what has previously been done with HPMS instruments. In general, a minimum of 6 MS data points is required to adequately define the GC peak, resulting in an MS acquisition rate of 6 Hz (167 ms per scan). Therefore, to maximize the signal to noise ratio, the MS scan function should be as short as possible in order to average as many MS scans in that time frame as possible.

Rather than developing miniaturized GC instrumentation, the data presented in this chapter was generated with a full size commercial GC in order to demonstrate the feasibility of a miniaturized GC-MS operated at high MS pressure. The instrument chosen was an Agilent 7890 Gas Chromatograph mainly due to the 6890 and 7890 series history of being one of the most common and reliable instruments available. It was also flexible enough to suit the needs of this project with the ability to handle multiple sources and columns using both nitrogen and helium carrier gasses.

A schematic of the general configuration of the GC and GC-MS experiments described in this chapter can be found in Figure 5.1. Two identical columns connected to separate inlets were used in order to compare the HPMS detector with the commercial flame ionization detector (FID). Briefly, an FID works by burning the effluent of the GC with a hydrogen/oxygen flame. A series of reactions occur from combustion of organics present to generate ions that are subsequently detected electronically. Because the FID column outlet was at atmospheric pressure while the HPMS outlet was under vacuum, the same column head pressure would yield different flow rates and analyte retention times for the two

columns. For the most direct comparison, conditions for the two columns were chosen in order to have the same average linear velocity for the two columns so that analyte retention times were very nearly equivalent.

The interface between the GC column and the miniature MS vacuum chamber described in Chapter 4 can also be seen in the schematic in Figure 5.1 and images of the interface can be found in Figure 5.2. The capillary connection is made with a 1/16" capillary fitting with a 0.5 mm adapter ferrule going to a 1/4" tube (ZLTA41, Vici). This tube was tapped to the same pitch as the miniature vacuum chamber's standard 1/4" vacuum ports so it could be attached with Teflon tape to create a vacuum seal. To prevent any cold spots on which analyte could condense, this 1/4" tube was wrapped in heating cord and sheathed in a larger diameter Teflon tube. Lastly, a hole cut through the GC oven wall including insulation so the transfer line could be threaded through to outside the GC oven. The transfer tube heating cord was kept at 70°C using a temperature controller in all experiments. Detailed descriptions of all MS configurations used can be found in Chapter 4, thus only brief descriptions of the MS components used will be given in this chapter for each experiment described here.

5.2 GC-MS Operation with Electron Multiplier Detection

Due to greater sensitivity in comparison to Faraday cup (FC) detectors, it was decided to use an electron multiplier (EM) detector in the first attempts to gather GC-MS data. The pressure limitations set by the EM required both pumping with a turbomolecular vacuum pump and the use of a single element CIT with r_o = 500 µm and 400 µm diameter endcaps.

The trap was operated at 7.1 MHz RF frequency with boundary ejection for all experiments described in this section.

Initial Proof of Concept GC-MS Experiments

A simple mixture of six benzene analogs (benzene, toluene, ethylbenzene, *p*-xylene, *o*-xylene, and mesitylene) in GC grade hexanes was made so that a 0.5 µL split injection yielded 50 ng of each analyte on-column. A 30 m column [Agilent HP-5, (5% phenyl)-methylpolysiloxane, 320 µm I.D., 0.25 µm film thickness] was cut in half to yield two identical 15 m columns. The minimum obtainable flow rate for the MS column was 3 mL/min of N_2 carrier gas due to the outlet of the relatively wide bore column being under vacuum. This configuration resulted in a slightly higher than desired pressure of 1.5 Torr for the MS. The resulting linear velocity in both columns of 93 cm/s and an oven ramp of 25°C/min after a 0.3 min hold at 40°C resulted in all six analyte peaks eluting in 1.65 min.

Chromatograms comparing the µMS detector to the commercial FID detector for these conditions can be found in Figure 5.3. This initial GC-MS data was encouraging, having an ample signal to noise ratio with 15 MS scan averaging and no noticeable GC peak broadening compared to the FID data. However, the slow MS data acquisition rate is apparent as only ~2 MS data points are present for each GC peak. This slow acquisition was partially due to the rudimentary software written to gather this initial data. Further data with these experimental conditions can be found in Figure 5.4, showing selected mass spectra taken from selected GC peaks. It is clear that sampling this mixture with the MS only would yield many overlapping peaks making it impossible to identify or quantify the different components. This shows the necessity for the GC separation prior to MS analysis. With the

GC separation it is possible to differentiate between compounds, such as *p*-xylene and ethylbenzene, which exhibit identical mass spectra.

GC-MS Improvements

After the promising initial GC-MS data, further steps were taken to improve performance and further test the capabilities of the GC-MS with EM detection. The first change was a hardware modification, switching the 320 μm diameter column for a new column of 250 μm diameter [Restek, Rxi-5ms, (5% diphenyl)-dimethyl polysiloxane, 0.25 μm thick film). Moving to this narrower bore column while maintaining the 15 m length reduces the minimum possible flow rate. Now the GC column was operated at a 2 mL/min flow rate (76 cm/s) which yielded the target MS pressure of 1 Torr. Additionally, in collaboration with William Gilliland, the data acquisition and analysis software was overhauled for greater flexibility and faster data acquisition. Instead of averaging a set number of spectra and saving the averaged spectrum to disk, each individual MS scan was saved in RAM as a linked list and only saved to disk at the end of the GC separation, eliminating dead time due to writing to disk during data acquisition. This method also improved the flexibility of data analysis, allowing one to choose how many spectra to average after the data is collected. Unfortunately, the individual MS scan acquisition rate was somewhat limited by the USB DAQ (NI-6363, National Instruments), having a 10 ms dead time in between spectral acquisition. Because the MS scan functions were 10 ms themselves, the maximum rate to acquire individual MS scans was 20 ms, meaning that a 15 scan average took a total of 300 ms whereas it would only take a total of 150 ms with improved hardware.

An example GC-MS chromatogram with these improvements, once again compared to FID detection, can be found in Figure 5.5. In this case a more complicated mixture of 15 organic analytes, including several chemical warfare simulants, was analyzed. Sample was injected such that 100 ng of each analyte were injected on-column. A slightly faster temperature ramp of 35°C/min was used in order to elute all 15 analytes in 2.5 minutes. As with the previous data, the GC-MS chromatogram compares well with the FID generated chromatogram and the number of MS data points per GC-MS peak shows improvement over Figure 5.3. All the peaks detected in the FID chromatogram are present in the μMS chromatogram, although peak tailing is observed in some of the later eluting peaks. Plate counts for the benzene peak in the FID and μMS chromatograms were calculated to be 35,300 and 31,000, respectively. Much like Figure 5.4 is an example of the utility of the GC separation, Figure 5.6 demonstrates the benefit of MS detection. The GC peak at 4.5 minutes is the result of two analytes coeluting, dimethyl methylphosphate (DMMP) and 2,6-lutidine. By comparing the mass spectra detected during the first and second halves of this peak, one can observe a distinct spectrum from each compound.

5.3 GC-MS Operation with Faraday Cup Detection

Due to the desire to operate the entire MS at 1 Torr of buffer gas pressure for handheld instruments, GC-MS operation was explored using a Faraday cup ion detector. It was initially unclear whether adequate sensitivity could be achieved with a Faraday cup due to the limited signal averaging imposed by the GC time scales. However, the sensitivity gains (~7X over CIT arrays) observed when using SLIT arrays, demonstrated in Figure 3.8, suggested that a Faraday cup based GC-MS system was feasible.

Faraday Cup versus Electron Multiplier for GC-MS Detection

The μMS with Faraday cup was used as a GC detector under the same conditions as described for Figure 5.5. The mass spectrometer operated at 1 Torr N_2 used a 3 element SLIT array (x_o = 500 μm, $2y_o$ = 3 and 4 mm) for ion trapping and the A250CF Faraday cup detector apparatus described in Chapter 3; with all vacuum pumping occurring on the detector chamber, inducing flow through the trap for maximum sensitivity. Again, 100 ng of each analyte was injected on-column. Because of the higher levels of background noise with Faraday cup detection, 30 scan averages were used for this chromatogram rather than 15. The comparison of GC-MS data taken with the Faraday cup versus electron multiplier and FID chromatograms is shown in Figure 5.7. When directly comparing the GC-MS chromatograms using FC and EM detection, they seem quite similar except for the slightly wider GC peaks (peak #2 for example) in the case of the FC, which are most likely due to higher signal averaging. The signal to noise ratio for FC detection is slightly worse, but the fact that it is on the same order as the EM data is evidence of the many more ions trapped and analyzed by the SLIT arrays.

GC-MS with Helium Buffer Gas

Helium is preferred as a GC carrier gas to nitrogen because separations using helium can be run in shorter times while retaining the same resolution. In addition, as shown in Chapter 2, the resolution in in HPMS is drastically improved with the use of helium buffer gas rather than nitrogen. The major drawback of using helium in a portable GC-MS instrument is the need to bring a helium source out into the field. However, it is likely that for some applications the performance gains afforded by the use of helium are worth the

addition of a portable helium tank. Therefore, the performance of the GC-MS instrumentation with Faraday cup detection was explored utilizing helium.

Because helium has different discharge characteristic than nitrogen, several changes had to be made to the glow discharge source. A pressure of 1 Torr and an electrode spacing of 1 cm results in trying to operate the glow discharge to the left of the minimum in Paschen's curve[30] leading to prohibitively high voltage requirements. To lower the voltage required for discharge, either the operating pressure or the electrode spacing must be increased. Both methods were attempted and stable glow discharge was achieved either at a pressure of 2 Torr with 1 cm spacing or at a pressure of 1 Torr with 3 cm spacing. Other than these modifications, the GC-MS was run under identical conditions as the prior Faraday cup experiments with nitrogen.

Figure 5.8 compares chromatograms taken with helium carrier/buffer gas (under both 1 and 2 Torr conditions) to a chromatogram using nitrogen. It should also be noted that a new organic analyte mixture was made for these experiments with the addition of methyl salicylate, another chemical warfare simulant. Upon inspection, the first observation is that the 1 Torr helium chromatogram has a lower signal to noise ratio with the peaks for DMMP; 2,6-lutidine; and dichlorobenzene being almost or completely absent. On the other hand, the 2 Torr data actually achieved a better signal to noise ratio than the nitrogen chromatogram, albeit with the m-toluidine peak being absent. This inconsistent performance with helium is most likely due to difficulty in obtaining stable glow discharge in helium, an issue that has been encountered by others in our laboratory as well. Unfortunately, progress in creating a glow discharge source that is tailored specifically to helium has been slow. When comparing the mass spectra generated, the peak widths seen in helium are narrower than nitrogen as

expected, measured at 3.8 Th and 5.9 Th FWHM, respectively. However, from the data presented in Chapter 2, peak widths between 1 and 2 Th would be expected for operation in helium. Recent data from our collaborators shows that even small amounts of air contamination in helium buffer gas causes significant peak broadening and it was suggested that air contamination from small vacuum leaks might be behind the wider than expected peaks in this helium GC-MS data.

5.4 Sensitivity and LOD Determination for GC-MS

After GC-MS operation was successfully demonstrated in several configurations, the next step was a thorough study of the system's sensitivity to determine parameters influencing sensitivity, and to find an overall system limit of detection (LOD). These tasks were completed for the optimal case of nitrogen as the carrier gas and Faraday cup based MS detection.

Signal to Noise Ratio and MS Averaging

Ideally, signal averaging reduces the amount of random noise in a measurement by the square root of the number of spectra averaged. This is certainly the case for the stand alone HPMS systems, but for measuring transient signals such as those from a GC, one must take into account the time necessary to obtain the averaged signal. The signal to noise ratio (S/N) for detection of a GC peak increases with a small number of spectra averaged, plateaus, and then begins to decrease as a greater portion of the spectra that are being averaged are no longer near the highest intensity portion of the GC peak. The S/N curve for the FC based GC-MS data from Figure 5.7 is shown in Figure 5.9 and was generated using the standard deviation of the noise. It shows a relatively constant S/N level between 10 and

20 averaged scans. With this data in hand, one would most likely choose to utilize scan averaging between 10 and 15 in order to collect more MS data points per GC peak with only a slight reduction in S/N. Additionally, recall that the acquisition time of a single mass spectrum is currently hardware limited to twice as high as it should be. The use of a higher quality DAQ would shift the S/N plateau up and to the right, improving performance.

Sensitivity versus Ionization

The number of ions generated and trapped is a function of both how long the ionization portion of the scan function lasts and of the magnitude of the voltage difference between the glow discharge plates. It should also be apparent that sensitivity is also a function of the ionization conditions. Therefore, calibration curves were generated with increasing concentrations of aniline at several different ionization conditions. The results, seen in Figure 5.10 show a linear dependence with the amount of analyte injected on the column. The slope of this line, i.e. the sensitivity, is also greater with increased ionization as expected.

From the highest intensity set of data points (displayed in green) the LOD (3X standard deviation of the noise) of the GC-MS system was estimated to be 0.056 ng injected, or 248 ppb gas concentration. This represents a good initial system LOD, but several straightforward improvements can be made to get this number well under 100 ppb. First, making the upgrade to a higher quality DAQ will double the acquisition rate, leading to twice the spectral averaging; second, work is currently underway on a Faraday cup amplifier with half the noise of the current amplifier; and finally, a minor redesign of the trap electrodes and

chamber could allow for several more SLIT elements to be added to the array to improve sensitivity.

Linear Dynamic Range of GC-MS System

The data plotted in Figure 5.10 was intentionally taken within the instrument's linear dynamic range (LDR). Unfortunately, when concentrations much higher were studied (e.g. the black set of data points in Figure 5.11) the signal level quickly plateaus. The log-log plotted data of Figure 5.11 illustrates the narrow LDR of the current GC-MS system of approximately one order of magnitude. This LDR limits quantification to a very narrow range of analyte concentrations, although useful qualitative information can still be obtained over a much wider concentration range. To alleviate the issues ion traps have with LDR, all commercial instruments implement some form of automatic gain control (AGC) in which the amount of ionization is varied depending on the number of ions detected in the previous scan. Changing the ionization conditions covers different ranges of concentrations as shown in Figure 5.11, thus AGC implementation on this system could increase the LDR to two or three orders of magnitude. In addition, the strategies to improve LOD discussed in the previous section would also widen the LDR, leading to an instrument that can provide both qualitative and quantitative information effectively.

It was found that working at concentrations much above the LDR of the mass spectrometer led to poor chromatographic resolution and increased peak tailing. By collecting data within the LDR and by applying additional heating to the MS chamber, improved chromatographic data was obtained. Figure 5.12 is another separation of 15 organic compounds (10 ng of each on column) taken with FC detection and N_2 carrier gas.

This data represents the highest quality GC-MS chromatogram to date, showing chromatographic resolution equal to that of the FID detector while still exhibiting large S/N. The equivalent resolution can be easily observed by comparing the partially resolved GC peaks (#4 and #5) between the two chromatograms.

5.5 Conclusions

The use of a miniaturized ion trap mass spectrometer as a GC detector for fast separations (< 2.5 min) was demonstrated using both an electron multiplier based and Faraday cup based MS systems. Nitrogen rather than helium carrier gas was used for the majority of the experiments due to its applicability to portable instrumentation. However, proof of concept data was also collected using helium. Chromatographic resolution achieved with the μMS detector was equal to that obtained with a commercial FID detector. The largest current performance limitation is with the low linear dynamic range, but implementation of automatic gain control would help to increase the LDR without any further hardware modifications.

5.6 Figures

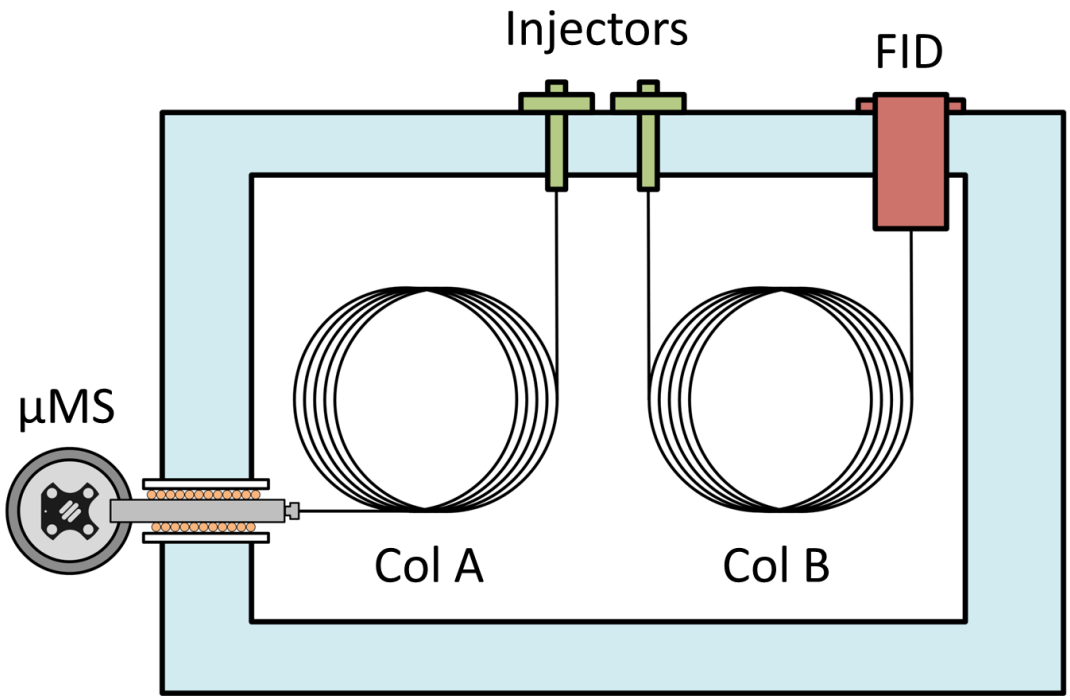

Figure 5.1: Schematic diagram of the GC and GC-MS used to compare the experimental µMS detectors and the commercial FID detector. In all cases, identical injectors and columns were used under conditions to yield identical average velocities in both columns. Also shown is the heated µMS transfer line traversing the insulating oven wall.

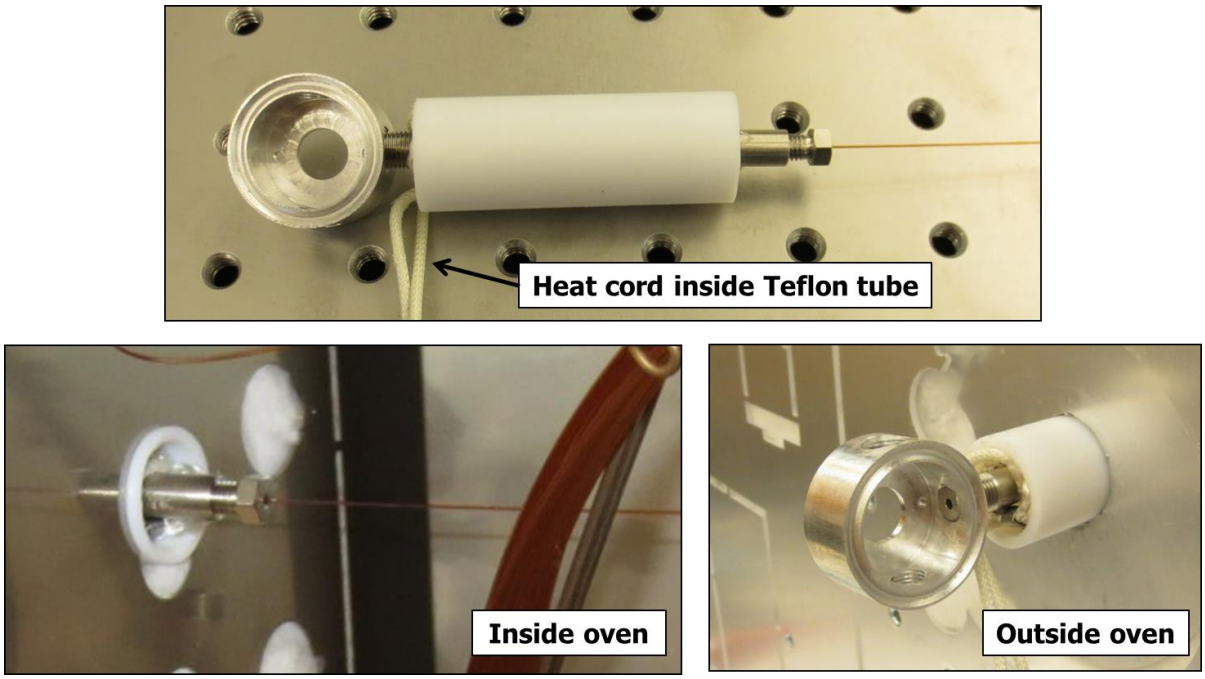

Figure 5.2: Images of the heated μMS transfer line. A 1/4" tube adapter fitting screws directly into the miniature vacuum chamber. This tube is wrapped with heating cord and kept in place by a 3/4" Teflon tube.

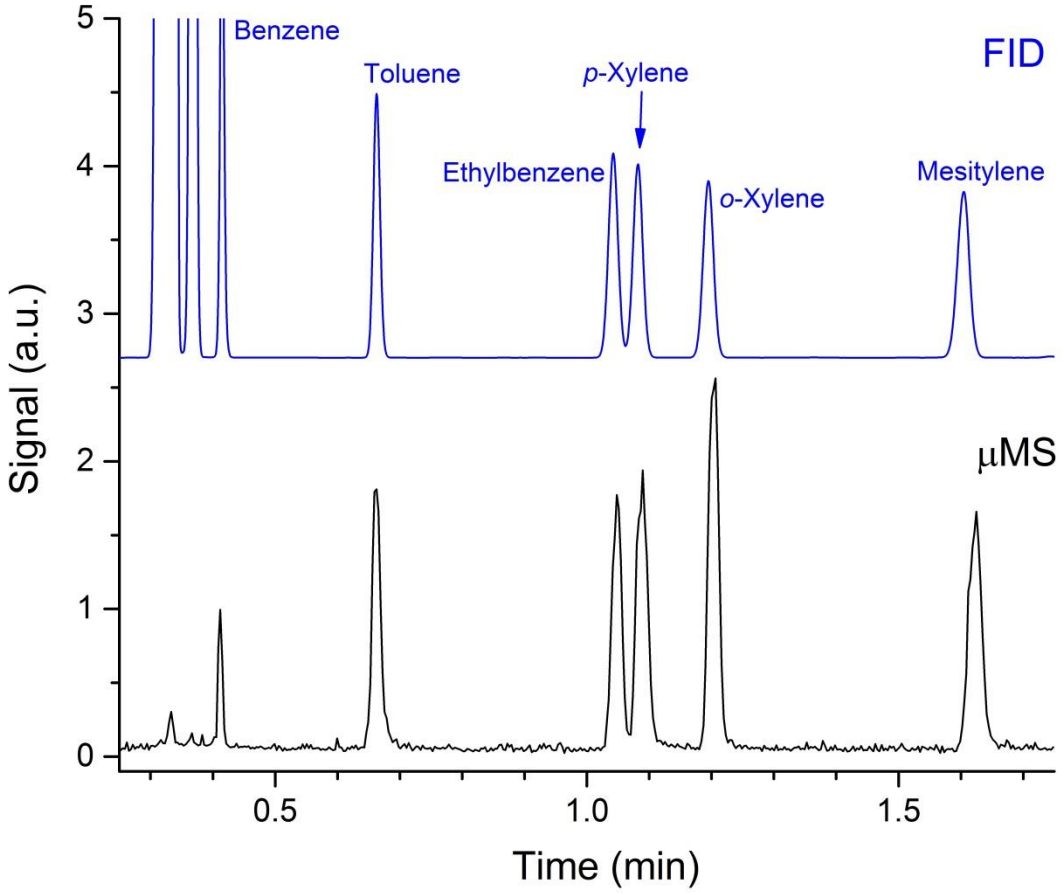

Figure 5.3: Chromatographic separations of six benzene analogs comparing the performance of the commercial FID detector to that of a μMS detector using an electron multiplier. A flow rate of 3 mL/min nitrogen through a 320 μm, 15 m long column was used to separate the compounds in approximately 1.6 min. Each chromatographic data point was the result of an average of 15 MS scans taken at 1.5 Torr background pressure. The large, unlabeled peaks prior to 0.5 min are due to solvent (hexanes mixture).

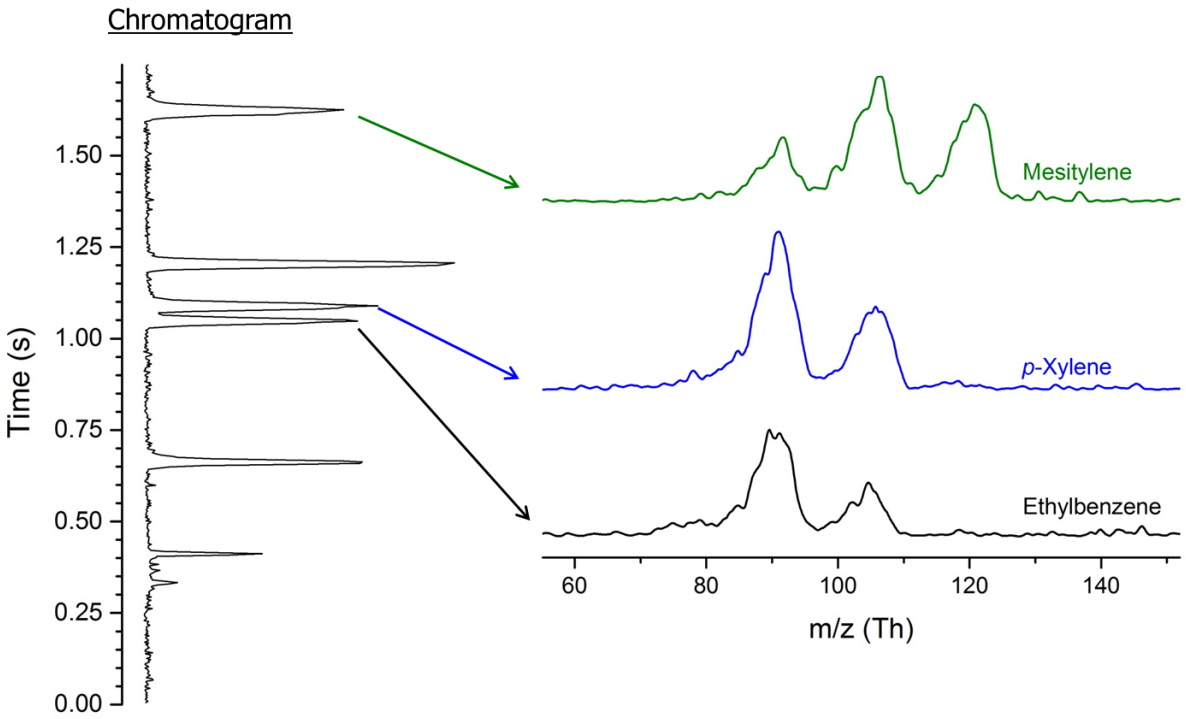

Figure 5.4: Selected mass spectra from the same GC-MS chromatogram (left) presented in Figure 5.3. The mass spectra demonstrate the utility of the GC as these spectra would be indistinguishable from one another using only mass spectrometry.

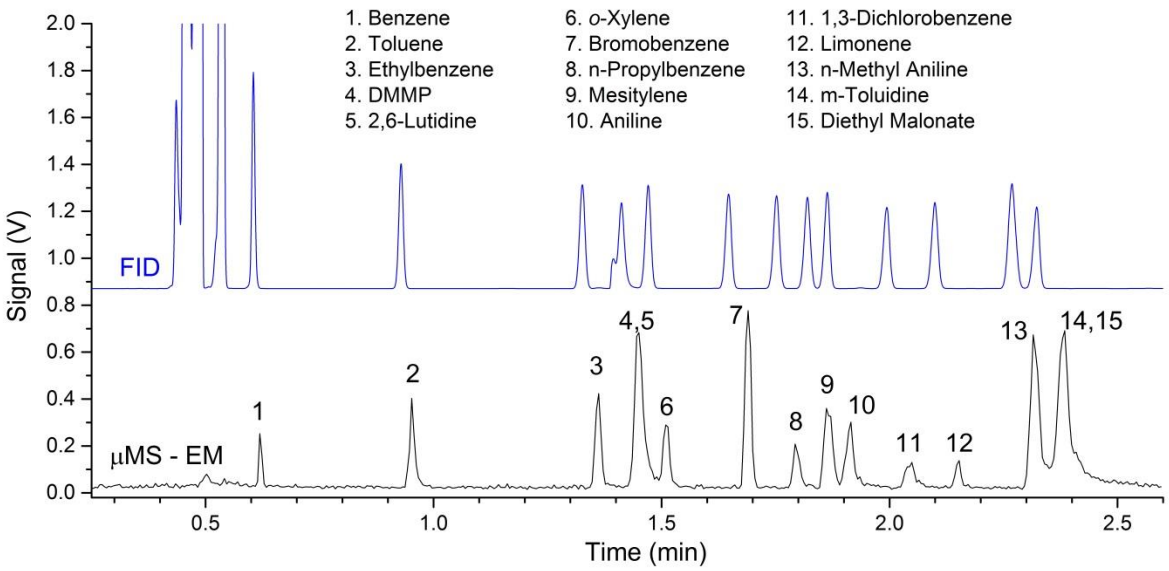

Figure 5.5: GC detector comparison with an improved separation of 15 organic compounds. A narrower bore, 250 μm diameter column resulted in a lower flow rate of 2 mL/min N_2 and a 1 Torr MS pressure while improved data acquisition software resulted in a higher MS sampling rate. The separation successfully detected all 15 compounds with only 2 overlapping peaks. Slight retention time differences are attributed to differences in column lengths between the FID and μMS columns.

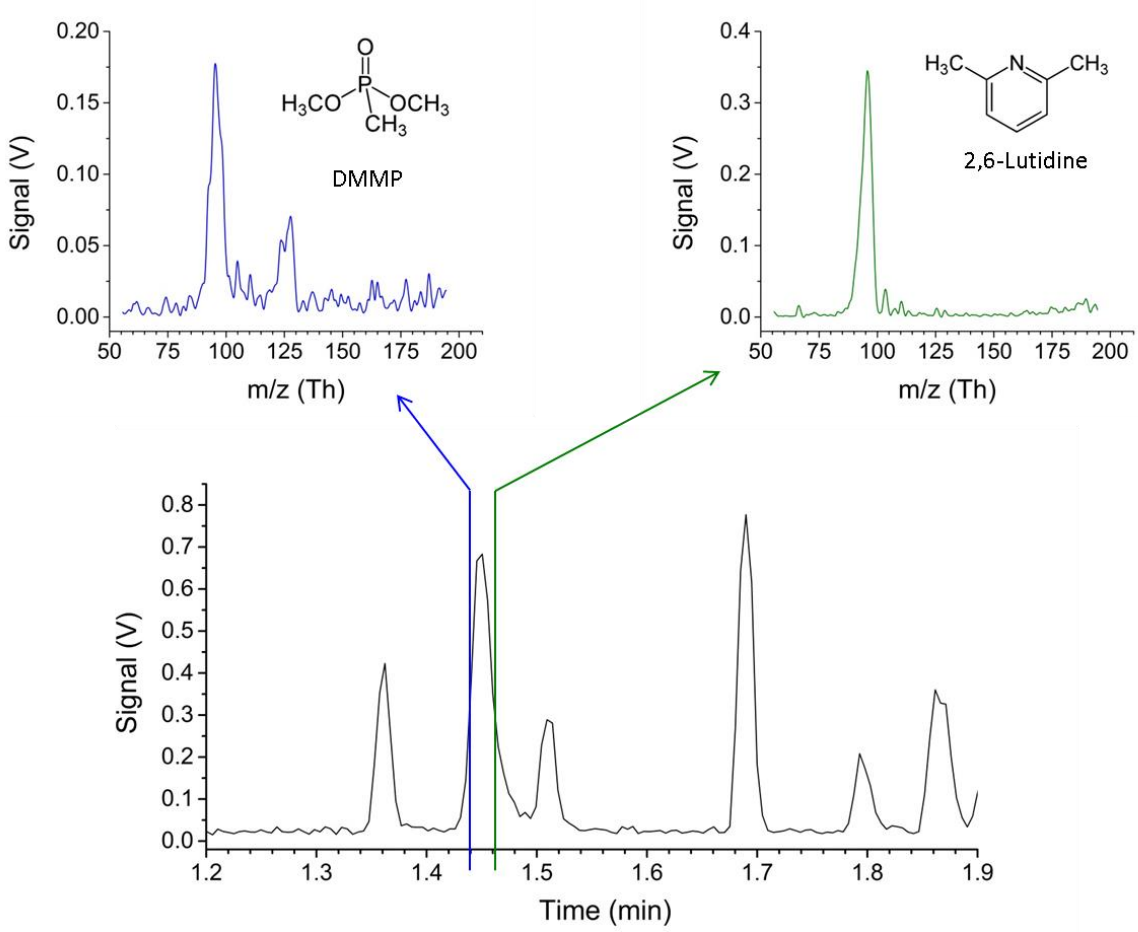

Figure 5.6: Two distinct mass spectra from different sections of the same GC peak demonstrating the ability of the µMS detector to differentiate more than one compound from a coeluting GC peak.

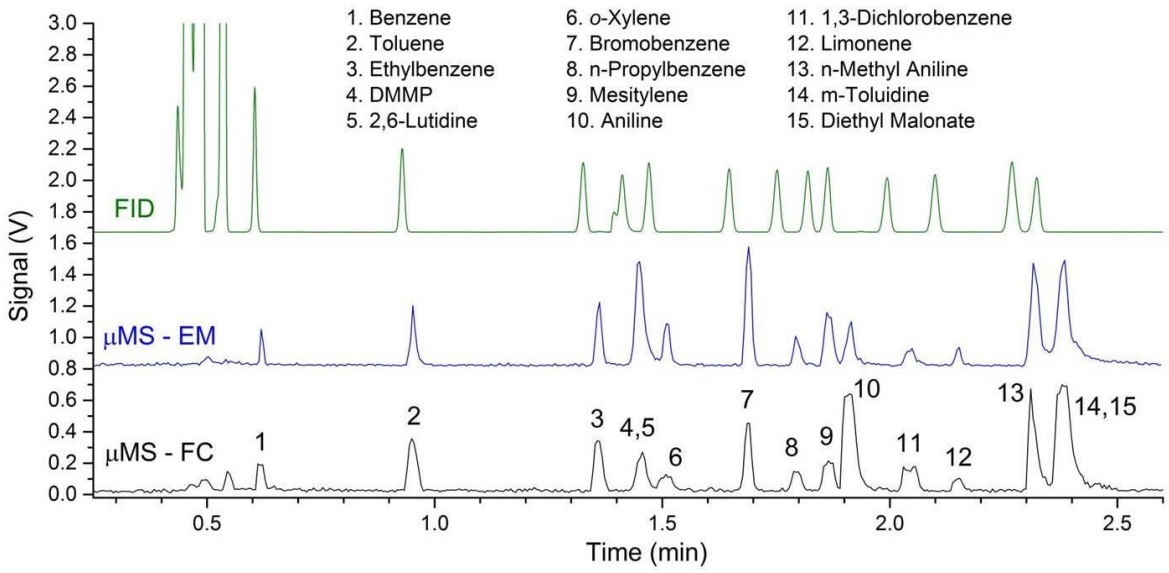

Figure 5.7: Comparison of a Faraday cup based GC-MS detector to that of an EM based GC-MS detector and a FID GC detector for the detection of a 15 component mixture. Upon transitioning to a FC based MS, detection of the all the same compounds was achieved with only slightly lower S/N.

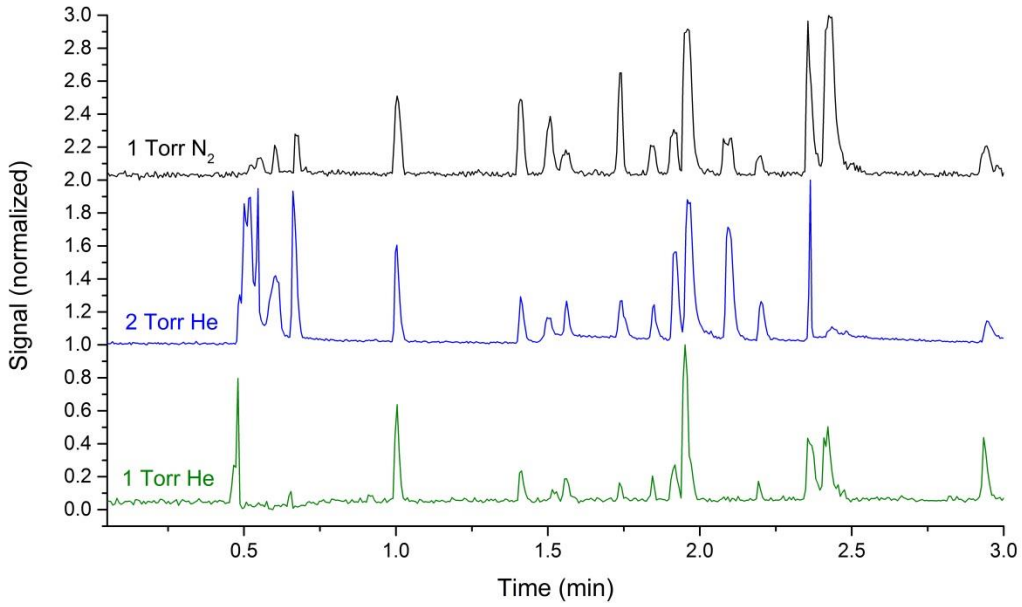

Figure 5.8: Comparison of GC-MS chromatograms taken under 1 Torr N_2 buffer gas conditions with those taken under 1 and 2 Torr He buffer gas conditions. Several peaks in the 1 Torr helium data have a lower S/N ratio with several peaks being almost or completely absent. The 2 Torr data on the other hand has the highest S/N of all three. This inconsistency is attributed to the difficulty of obtaining a stable glow discharge in helium.

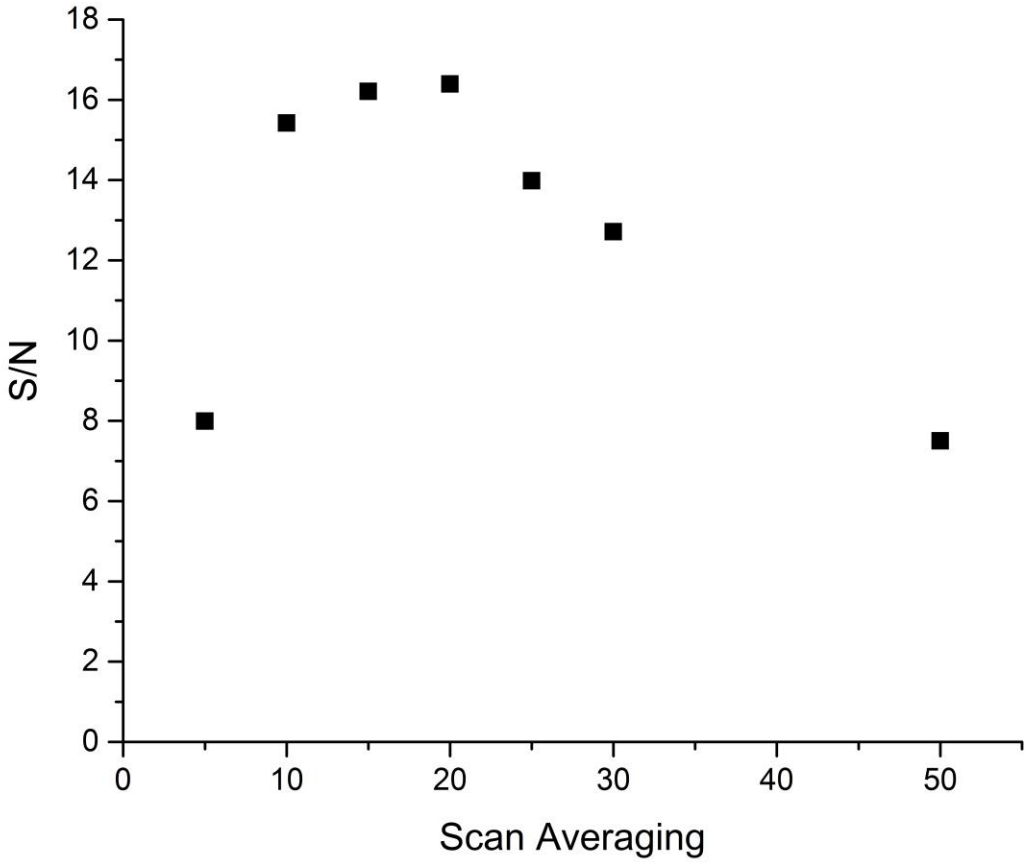

Figure 5.9: Plot of S/N ratio versus number of MS scans averaged for a single GC-MS data set. A rise in S/N is initially observed followed by a plateau and a decrease as a greater portion of the spectra that are being averaged are no longer near the highest intensity portion of the GC peak.

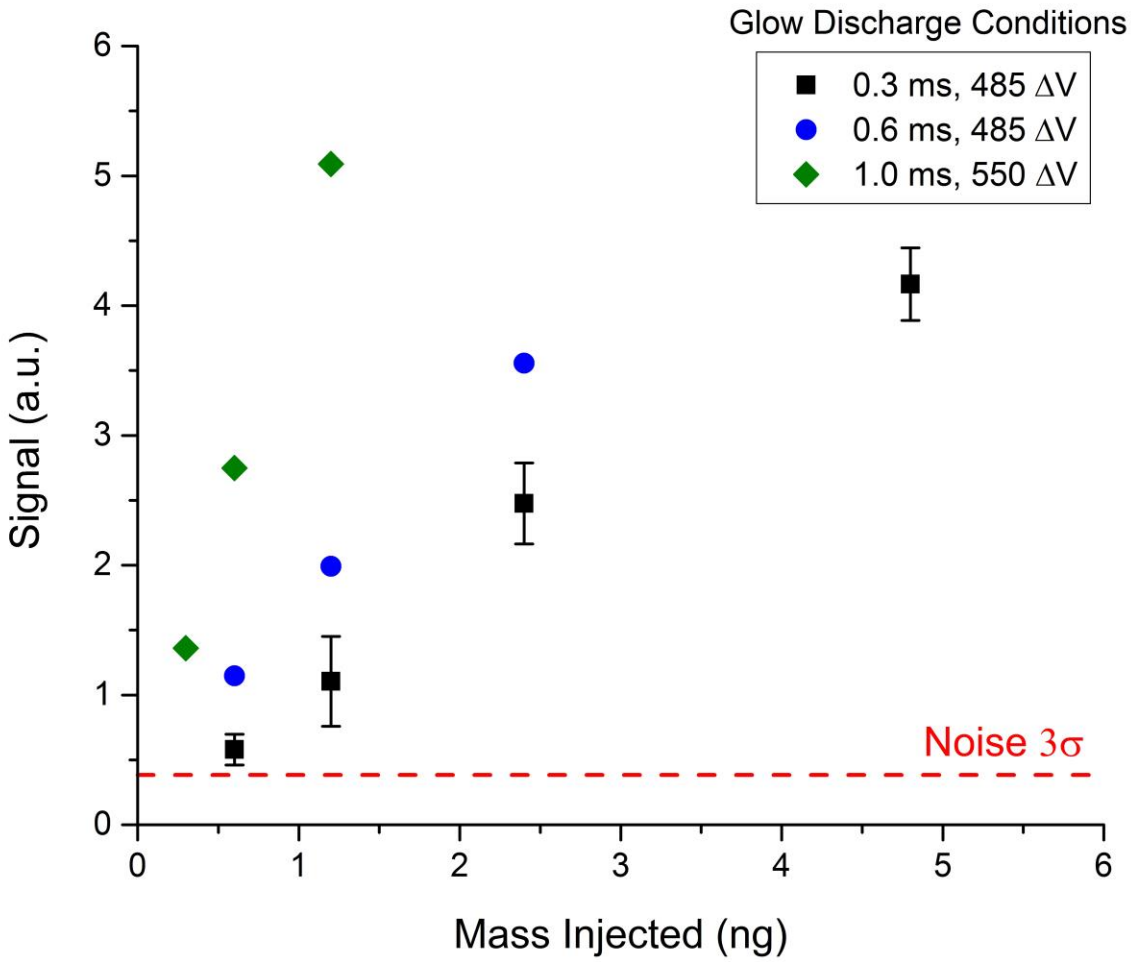

Figure 5.10: Calibration curve of GC-MS detection of aniline using several glow discharge ionization conditions with the noise level indicated in red. This data demonstrates that the sensitivity of the µMS detector varies with the ionization conditions with an increase in ionizing electrons leading to an increase in sensitivity. Error bars for the black data set represent the standard deviation of three separate GC runs.

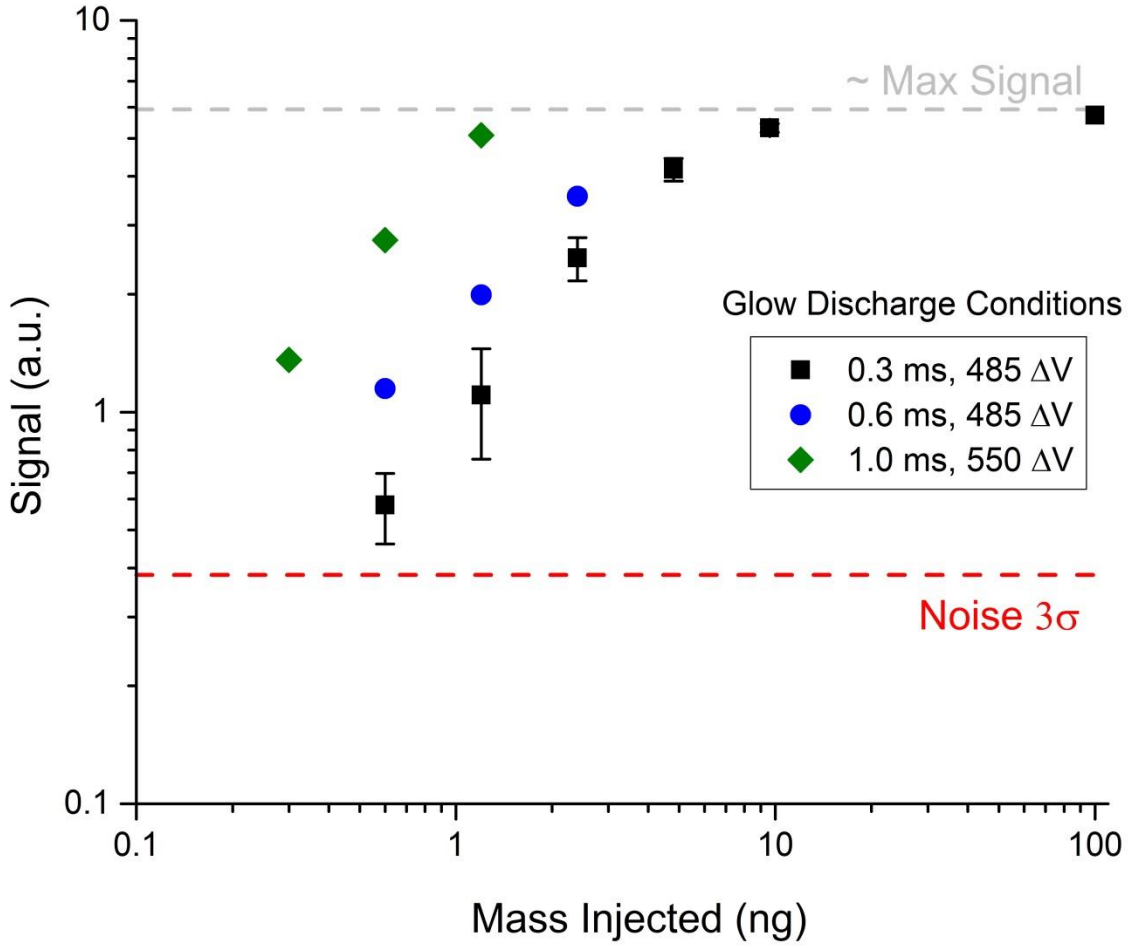

Figure 5.11: Log-log plots of the calibration curve data from Figure 5.10 with an added data point at 100 ng injected on-column. With the 100 ng data point representing the maximum signal that the µMS can obtain, this data demonstrates the limited linear dynamic range of this detector. However, the blue and green data sets demonstrate that this range can shift based on ionization conditions leading to an overall wider LDR if automatic gain control is implemented.

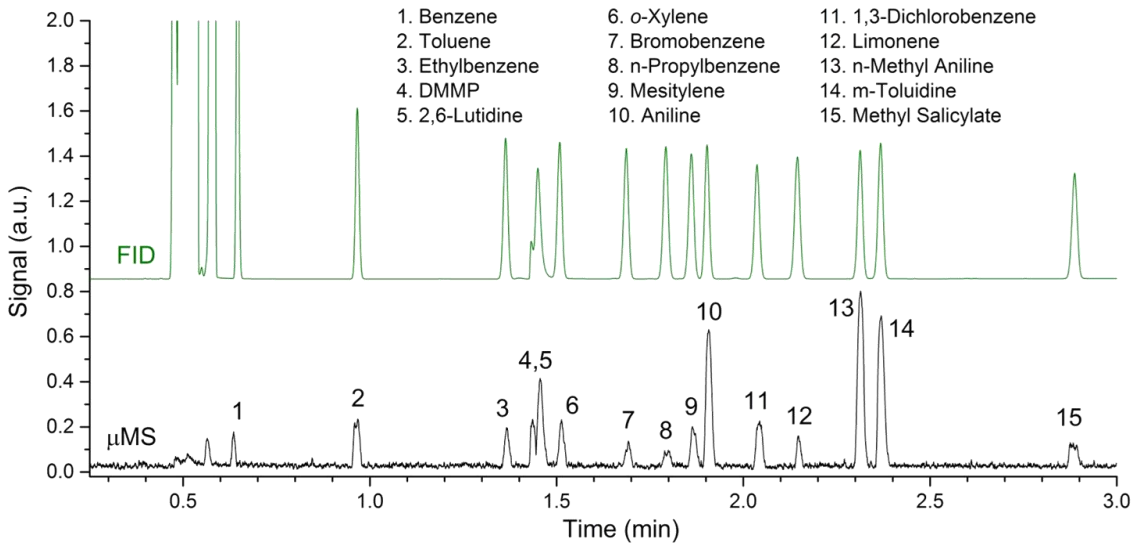

Figure 5.12: High resolution GC-MS chromatogram taken with a FC based μMS detector in nitrogen buffer gas (black) compared to the commercial FID detector (green). A mixture of 10 ng each of 15 organic species was injected on-column. This represents the best chromatographic data taken with any of the μMS detectors, demonstrating chromatographic resolution equal to that of the commercial FID detector while still exhibiting enough S/N to identify each peak.

5.7 References

1. James, A. T.; Martin, A. J., Gas-liquid partition chromatography; the separation and micro-estimation of volatile fatty acids from formic acid to dodecanoic acid. *The Biochemical journal* **1952,** *50* (5), 679-690.

2. Golay, M. J. E., A Performance Index for Gas Chromatographic Columns. *Nature* **1957,** *180* (4583), 435-436.

3. Ettre, L. S., Open-tubular columns: Past, present and future. *Chromatographia* **1992,** *34* (9-10), 513-528.

4. Dandeneau, R. D.; Zerenner, E. H., An investigation of glasses for capillary chromatography. *Journal of High Resolution Chromatography* **1979,** *2* (6), 351-356.

5. Matisová, E.; Dömötörová, M., Fast gas chromatography and its use in trace analysis. *Journal of Chromatography A* **2003,** *1000* (1–2), 199-221.

6. Lee, M. L.; Yang, F. J.; Bartle, K. D., *Open Tubular Gas Chromatography: Theory and Practice*. Wiley: New York, NY, 1984.

7. Smith, P. A., Person-portable gas chromatography: Rapid temperature program operation through resistive heating of columns with inherently low thermal mass properties. *Journal of Chromatography A* **2012,** *1261* (0), 37-45.

8. Bond, E. J.; Dumas, T., A portable gas chromatograph for macro- and microdetermination of fumigants in the field. *Journal of Agricultural and Food Chemistry* **1982,** *30* (5), 986-988.

9. Das, T. N., Terpenes in a conifer forest: Detection at sub-parts per billion level without sample preconcentration. *Atmospheric Environment. Part A. General Topics* **1992,** *26* (15), 2853-2857.

10. Lee, I. N.; Hee, S. S. Q.; Clark, C. S., Additivity of Detector Responses of a Portable Direct-Reading 10.2 eV Photoionization Detector and a Flame Ionization Gas Chromatograph for Atmospheres of Multicomponent Organics: Use of PID/FID Ratios. *American Industrial Hygiene Association Journal* **1987,** *48* (5), 437-441.

11. Ehrmann, E. U.; Dharmasena, H. P.; Carney, K.; Overton, E. B., Novel Column Heater for Fast Capillary Gas Chromatography. *Journal of Chromatographic Science* **1996,** *34* (12), 533-539.

12. Hail, M. E.; Yost, R. A., Compact gas chromatograph probe for gas chromatography/mass spectrometry utilizing resistively heated aluminum-clad capillary columns. *Analytical Chemistry* **1989,** *61* (21), 2410-2416.

13. Terry, S. C.; Jerman, J. H.; Angell, J. B., A gas chromatographic air analyzer fabricated on a silicon wafer. *Electron Devices, IEEE Transactions on* **1979,** *26* (12), 1880-1886.

14. Radadia, A. D.; Masel, R. I.; Shannon, M. A.; Jerrell, J. P.; Cadwallader, K. R., Micromachined GC Columns for Fast Separation of Organophosphonate and Organosulfur Compounds. *Analytical Chemistry* **2008,** *80* (11), 4087-4094.

15. Sun, J.; Cui, D.; Li, Y.; Zhang, L.; Chen, J.; Li, H.; Chen, X., A high resolution MEMS based gas chromatography column for the analysis of benzene and toluene gaseous mixtures. *Sensors and Actuators B: Chemical* **2009,** *141* (2), 431-435.

16. Vial, J.; Thiébaut, D.; Marty, F.; Guibal, P.; Haudebourg, R.; Nachef, K.; Danaie, K.; Bourlon, B., Silica sputtering as a novel collective stationary phase deposition for microelectromechanical system gas chromatography column: Feasibility and first separations. *Journal of Chromatography A* **2011,** *1218* (21), 3262-3266.

17. Ali, S.; Ashraf-Khorassani, M.; Taylor, L. T.; Agah, M., MEMS-based semi-packed gas chromatography columns. *Sensors and Actuators B: Chemical* **2009,** *141* (1), 309-315.

18. Reidy, S.; George, D.; Agah, M.; Sacks, R., Temperature-Programmed GC Using Silicon Microfabricated Columns with Integrated Heaters and Temperature Sensors. *Analytical Chemistry* **2007,** *79* (7), 2911-2917.

19. Potkay, J. A.; Lambertus, G. R.; Sacks, R. D.; Wise, K. D., A Low-Power Pressure- and Temperature-Programmable Micro Gas Chromatography Column. *Microelectromechanical Systems, Journal of* **2007,** *16* (5), 1071-1079.

20. Lewis, A. C.; Hamilton, J. F.; Rhodes, C. N.; Halliday, J.; Bartle, K. D.; Homewood, P.; Grenfell, R. J. P.; Goody, B.; Harling, A. M.; Brewer, P.; Vargha, G.; Milton, M. J. T., Microfabricated planar glass gas chromatography with photoionization detection. *Journal of Chromatography A* **2010,** *1217* (5), 768-774.

21. Contreras, J. A.; Rockwood, A. L.; Tolley, H. D.; Lee, M. L., Peak sweeping and gating using thermal gradient gas chromatography. *Journal of Chromatography A* **2013,** *1278* (0), 160-165.

22. Tolley, H. D.; Tolley, S. E.; Wang, A.; Asplund, M. C.; Lee, M. L. In *Properties of Thermal Gradient GC Separations*, Pittcon, Chicago, Il, Chicago, Il, 2014.

23. Manginell, R.; Bauer, J.; Moorman, M.; Sanchez, L.; Anderson, J.; Whiting, J.; Porter, D.; Copic, D.; Achyuthan, K., A Monolithically-Integrated μGC Chemical Sensor System. *Sensors* **2011,** *11* (7), 6517-6532.

24. Gohlke, R. S., Time-of-Flight Mass Spectrometry and Gas-Liquid Partition Chromatography. *Analytical Chemistry* **1959,** *31* (4), 535-541.

25. Abian, J., The coupling of gas and liquid chromatography with mass spectrometry *Journal of Mass Spectrometry* **1999,** *34* (3), 157-168.

26. Syka, J. E. P., Chapter 4 - Commercialization of the Quadrupole Ion Trap. In *Practical Aspects of Ion Trap Mass Spectrometry,* March, R. E.; Todd, J. F. J., Eds. CRC Press: 1995; Vol. 1, pp 169-205.

27. Sinha, M. P.; Gutnikov, G., Development of a miniaturized gas chromatograph-mass spectrometer with a microbore capillary column and an array detector. *Analytical Chemistry* **1991,** *63* (18), 2012-2016.

28. Akapo, S. O.; Dimandja, J. M. D.; Kojiro, D. R.; Valentin, J. R.; Carle, G. C., Gas chromatography in space. *Journal of Chromatography A* **1999,** *843* (1–2), 147-162.

29. Contreras, J. A.; Murray, J. A.; Tolley, S. E.; Oliphant, J. L.; Tolley, H. D.; Lammert, S. A.; Lee, E. D.; Later, D. W.; Lee, M. L., Hand-Portable Gas Chromatograph-Toroidal Ion Trap Mass Spectrometer (GC-TMS) for Detection of Hazardous Compounds. *Journal of the American Society for Mass Spectrometry* **2008,** *19* (10), 1425-1434.

30. Paschen, F., On the potential difference required for spark initiation in air, hydrogen, and carbon dioxide at different pressures. *Annalen der Physik* **1889,** *273* (5), 69-96.